# A COMPUTATIONAL STUDY OF FUEL IMPINGEMENT IN THE INTAKE OF A SPARK IGNITION ENGINE

Thesis by:

Jason Ronald Guldan

A thesis submitted in partial fulfillment of the

requirements for the degree of:

**Master of Science**

**(Mechanical Engineering)**

**at the**

**UNIVERSITY OF WISCONSIN – MADISON**

**2007**

# APPROVED

---

Jaal B. Ghandhi

Associate Professor

22 May 2007

# Abstract

A computational study of fuel impingement in a port fuel injection gasoline engine was performed to gain an understanding of the fuel impingement process, and provide insight into high load fuel delivery, where oil dilution by fuel can be a significant problem. The relatively low intake manifold temperatures and large amount of fuel injected make fuel impingement and oil dilution of particular interest in marine outboard engines. This project included the development of a rezoning subroutine, a single-component fuel study and multi-component fuel study using KIVA.

Single-component studies of $C_6H_{14}$, $C_8H_{18}$, $C_{14}H_{30}$ and $C_8H_{17}$ (gasoline) gave an initial indication of the amount and location of fuel impingement. These results indicated a fuel-composition dependence of the fuel impingement process.

ASTM D-86 fuel distillation curves were used to create gasoline multi-component fuel distributions. The results of the multi-component study showed that the mass-averaged mean molecular weight fuel increased during time, suggesting that the heavy components in the fuel would have significant impact on the fuel film.

Additional single-component simulations were conducted with a fuel mass representative of the multi-component distribution to examine what effect heavier ($C_9H_{20}$ and $C_{10}H_{22}$) test fuels would have on the impingement process. The $C_9H_{20}$ and $C_{10}H_{22}$ simulations showed a higher fraction of the fuel forming a fuel film, 86.9% and 94.4% of total injected fuel, respectively, compared to 38.6% for $C_8H_{18}$ and 33.2% for $C_8H_{17}$. For the tested conditions, there is a clear transition in the

impingement process between $C_8H_{18}$ and lighter hydrocarbons and hydrocarbons that are heavier than $C_8H_{18}$.

# Acknowledgements

I would like to thank the many people who supported and guided me over the past two years at the Engine Research Center. First and foremost I would like to thank my advisor, Professor Jaal B. Ghandhi, for his guidance and support throughout my project. He kept me interested and motivated through the times when nothing seemed to work. I wish to thank the other members of my committee, Professors Rolf D. Reitz and Scott T. Sanders for reviewing this work. I would also like to thank Mercury Marine for their support of my project and for funding the Brunswick Fellowship.

I cannot give enough thanks to Randy Hessel for working with me to develop the rezoning subroutine and debug problems throughout the last two years. Without him, my project would have never possible. Another colleague that helped me significantly is Youngchul Ra. Like Randy, he took the time to explain KIVA and troubleshoot issues that I encountered during my research. Fellow students Mike Bergin, Achuth Munnannur and Jessica Brakora helped me through many code issues and took the time to help me learn KIVA.

Finally, I would like to thank my family: Daniel, Jacquelyn, Nicholas and Adam Guldan, and my girlfriend, Alicia Roeker, for supporting me throughout my time in Madison. They were there for me through my frustration and stress, even when I could not devote enough time for them.

# Table of Contents

# Lists of Figures

# Lists of Tables

# 1 INTRODUCTION

Computer simulation of engine systems has advanced tremendously due to advances in software and computational power in the recent decades. The range of applications has increased as the software and computational power have allowed more realistic simulation geometries and durations.

Internal combustion engines are a very demanding application of computational fluid dynamics (CFD) due to the transient, three-dimensional, two-phase flow in complex geometries. Fuel injection and atomization, wall impingement and vaporization of the spray, ignition and combustion chemistry are all major processes in engine simulations superimposed on the turbulent flow. These are complicated physical and chemical phenomena that are inherently computationally intensive.

Fuel impingement in the intake manifold of a spark-ignition engine can lead to liquid fuel entering the cylinder and impinging on the cylinder wall. This can be a serious problem because adhered liquid fuel does not react during the combustion event, and eventually may also migrate past the piston rings into the lubricating oil. Fuel tends to lower the lubricity of engine oil which results in higher engine wear.

Commercial fuels such as gasoline typically contain hundred of chemical components. These components vary in molecular weight and properties, and should be treated as a multi-component mixture to capture the true vaporization characteristics of the fuel. Continuous thermodynamic models have been developed

to deal with the multi-component nature of fuels. Since the vapor pressure of a chemical is related to its molecular weight, the vaporization of a multi-component fuel film depends on how the different components vaporize. The lighter fuel components would be expected to vaporize quickly leaving the heavier components in the film.

Simulation of fuel impingement is of interest because the problem is inherently difficult to investigate experimentally. A simulation that includes the multi-component nature of the fuel would be very useful because it would be able to give information on not only where fuel impingement is occurring in an engine, but also the time-varying composition of the film that eventually enters the engine.

## *1.1 Motivation*

The purpose of this research is to model fuel impingement in a Mercury Verado outboard engine. The Mercury Verado is a 4-stroke port injection engine that is super-charged and liquid cooled. The Mercury Verado engine comes in 200, 225, 250 and 275hp models and is currently the world's most powerful 4-stroke outboard boat engine.

The cooling system on an outboard engine uses lake or sea water as the cooling fluid. The pump is directly connected to the motor shaft which results in the cooling system flow rate proportional to engine speed. This relationship results in excessive engine cooling at high engine speeds.

At full power and engine speed (269hp output, 6100 rpm) for the Verado engine, the injection duration is 459.6 crank angles with 71.17mg of gasoline per

injection. The gasoline is injected out of 1 injector with 2 nozzles, each of which is aimed at the top of the intake valves. At low engine speeds, the gasoline absorbs heat from intake valves and vaporizes so only vapor-phase gasoline remains when the intake valves open and the fuel-air mixture is inducted. At high engine speeds the excessive cooling causes the intake valves and intake port to be relatively cool such that the liquid gasoline does not completely vaporize. This results in liquid gasoline building up in a film on the intake valves and intake port. The liquid gasoline eventually migrates into the cylinder. Excessive cylinder wall wetting can dilute the engine oil, reducing its lubricity, causing engine wear.

Another consideration that adds more complexity to experimental testing of fuel impingement is the amalgam of different hydrocarbons which makeup gasoline. Gasoline is a mixture of hydrocarbons that have a range of different molecular weights. The vapor pressure is inversely proportional to the molecular weight of the molecule, so the lighter molecules vaporize faster than the heavier molecules. The differing evaporation rates of the gasoline constituents result in the fuel film losing the lighter hydrocarbons over time while the heavier molecules tend to remain in the liquid phase in the film. These remaining heavy hydrocarbons would most likely be the components diluting the oil so the makeup of this film is important. In an experimental setup, a test fuel would need to match the fuels being used by engine owners. Gasoline can vary from state to state, and season to season, so determining what test fuel to use would be very difficult and the testing would need to be repeated for each test fuel.

## *1.2 Research Objectives*

The objective of this work is to model the fuel impingement in a Mercury Verado outboard engine. The simulation will be formed with a computational grid provided by Mercury Marine. The model will be exercised using both single-component fuels and multi-component fuel compositions to determine how fuel composition affects fuel impingement. The first objective of this study is to simulate single-component fuel impingement using multiple fuels to determine where the wall film is occurring. The second objective of this study is to simulate multi-component fuels of different fuel distributions and determine where the wall film is occurring and what the makeup of the wall film is.

## *1.3 Approach*

The KIVA family of codes was used to conduct this simulation. There has been significant research at the Engine Research Center using KIVA aimed at the development of more detailed models of the atomization, vaporization, ignition and combustion events. The investigation can be broken into two major portions:

- Single component modeling using $C_6H_{14}$, $C_8H_{18}$, $C_{14}H_{30}$, and single-component gasoline
- Multi-component modeling using different fuel mixture distributions

The single-component investigation involved development of a grid rezoning subroutine that allowed grid movement. The three single-component fuels chosen for study provided information on where a light fuel ($C_6H_{14}$), gasoline-like fuel

($C_8H_{18}$), and heavy fuel ($C_{14}H_{30}$) create wall films. The single component investigation was conducted using KIVA-3.

The multi-component investigation used the developed grid and rezoning subroutine to test previously determined fuel distributions along with fuel distributions that will be developed based on different test fuels information provided by Mercury Marine. The multi-component investigation was conducted using KIVA-3v Release 2 because it has multi-component continuous thermodynamic fuel vaporization. $C_9H_{20}$ and $C_{10}H_{22}$ were also simulated to study the heavy end components in gasoline and their effects on the fuel impingement process.

Chapter 2 contains an overview of the literature on the topics that are most closely related to this study. Chapter 3 details the model construction and simulation conditions. Chapter 4 reviews the results of the single-component simulation results, and Chapter 5 reviews the multi-component and heavy single-component simulation results. Chapter 6 concludes with a summary and recommendations for further work.

# 2 LITERATURE REVIEW

The development of engine models and the various subtopics such as sprays and combustion have been the subject of significant effort. This section will provide a brief overview of the topics that are most applicable to this study. The first section is a general overview of vaporization also covering the subtopic of multi-component fuel effects. The second section is an overview of fuel impingement and wall film literature. The third section a review of KIVA. The fourth and fifth sections summarize the wall film and multi-component models in KIVA.

## *2.1 Vaporization and Fuel Overview*

Droplet vaporization is a complex phenomena that is extremely relevant to internal combustion engines, and has a resulting effect on both the formation of liquid films created during fuel impingement and their subsequent evaporation. Droplet vaporization is a transient process as the size and, thus, the surface area is constantly changing. Heat is transferred into the droplet from the ambient air which produces vapor-phase fuel near the surface that transports due to a difference in the partial pressure of the fuel near the droplet and the ambient conditions. After an initial interaction with the ambient air where the droplet temperature increases to a steady-state temperature, the gas-phase heat transfer is balanced by the mass flux out of the droplet due to vaporization. In very hot ambient condition where the droplet lifetime is shorter than the initial heat up time, a steady-state temperature and, thus, equilibrium is never achieved.

### 2.1.1 Simple droplet vaporization theory

Fuel droplet vaporization theory (e.g. Turns, 2000) is developed and discussed in most standard combustion textbooks. Many assumptions are made to develop a simple but useful droplet vaporization model such as [34]:

1. The process is a quasi-steady problem such that the problem can be describe as if it were in steady state at any given time.
2. The droplet temperature is uniform throughout the droplet and in time, which removes the transient heating of the droplet from the problem.
3. The vapor surrounding the droplet is assumed to be determined by the vapor-liquid equilibrium at the droplet surface.
4. All of the thermo-physical properties are constant in space and time.

With these assumptions, the mass vaporization rate, $\dot{m}$ , is given by:

$$\dot{m} = 4\pi r_s \rho D_{AB} \ln(1 + B_Y) \qquad \text{Equation 1}$$

where the dimensionless transfer number $B_y$ is defined as [34]:

$$B_Y = \frac{Y_{A,S} - Y_{A,\infty}}{1 - Y_{A,S}}$$

$\dot{m}$ refers to the mass flow rate of liquid fuel out of the droplet, $r_s$ refers to the radius of the droplet at the surface, $\rho D_{AB}$ refers to the diffusivity of the fuel, $Y_{A,S}$ and $Y_{A,\infty}$ refer to the vapor mass fraction at the surface of the droplet and at a distance infinitely far away.

The droplet lifetime can be determined by integrating Equation 1 with respect to time which results in the $D^2$ law for droplet evaporation:

$$D^2(t) = D_0^2 - Kt \qquad \text{Equation 2}$$

where K is defined as an evaporation constant:

$$K = \frac{8\rho D_{AB}}{\rho_l} \ln(1 + B_Y)$$

The $D^2$ law provides a linear prediction of fuel droplet vaporization after an initial transient heat up time. For a more detailed derivation of the above refer to [34].

### 2.1.2 Makeup of modern fuels

Modern fuels used in internal combustion engines are an amalgam of different hydrocarbons that vary in volatility and ignition characteristics. The octane number is used to group gasoline fuels on the basis of auto-ignition quality where a fuel with a higher octane number is less likely to auto ignite. An octane number of 100 is equivalent to the auto-ignition properties of 100% iso-octane and an octane number of 0 is equivalent to the auto-ignition properties of a 100% n-heptane. A fuel is rated using the Research Octane Number (RON) or Motor Octane Number (MON). The RON is determine by running the fuel through a specific test engine with a variable compression ratio while the MON testing uses a similar test engine but the fuel mixture is preheated and operated under a higher engine speed and variable ignition timing. The octane number is the most recognized fuel property because it is widely used at refueling stations but it does not give an indication of the actual chemical makeup of the fuel. The chemical makeup of fuels can change immensely season-to-season or state-to-state even though they are grouped as the same fuels based on octane number.

The ASTM D86 test is used to obtain a distillation curve for fuels, which is then used as a measure of the volatility of the fuel. The ASTM D86 test is conducted by recording the increasing temperature of the vapor in the neck of a flask versus percent evaporated as 100ml of fuel is gradually heated and distilled. Generally, the temperature at fixed fractions of the resulting distillation curves is used to reference the volatility and compare different fuel blends.

The multi-component nature of commercial gasoline is very important to the vaporization of the fuel droplets. The majority of droplet vaporization and combustion studies have used single component test fuels as the subject of study, which provides the basic understanding of the underlying principles. Commercial gasoline consists of at least 200 components and a starting boiling point of 300K while the final boiling point can be as high as 500K [19]. The multi-component composition of gasoline results in complex vaporization processes that can only be approximated by single component models. As the vapor pressure of hydrocarbons is related to the molecular weight of the hydrocarbons, lighter hydrocarbon molecules will have a higher vaporization rate than heavier hydrocarbons at the same droplet temperature. This difference in vaporization rates results in transient processes of both the size of the fuel droplets and the droplet composition.

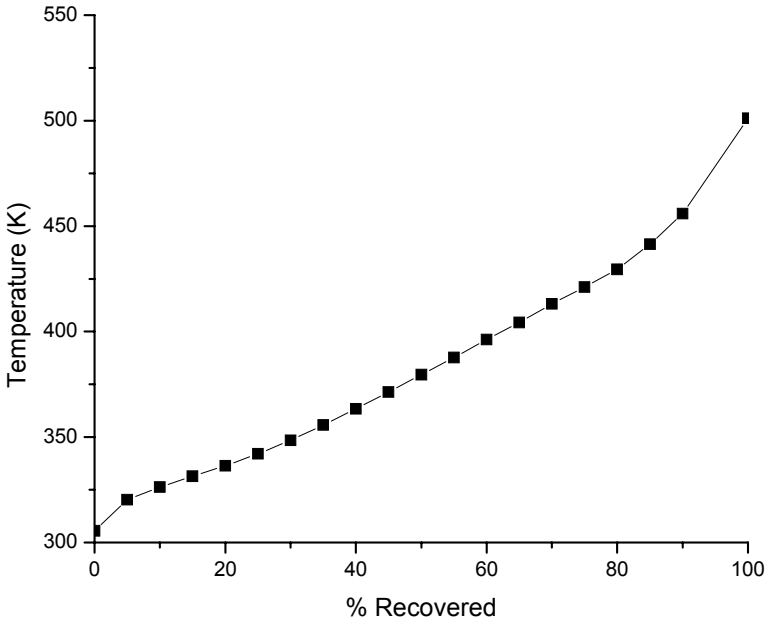


*Figure 1: Distillation Curve of Regular Unleaded Gasoline [24]*

A typical ASTM D86 curve is shown in Figure 1 shows that the range of temperatures can span hundreds of degrees over a continuous curve, suggesting hundreds of fuel components. The large number of fuel components has been confirmed by speciation analysis for gasoline [19]

## *2.2 Fuel Impingement Overview*

Wall impingement occurs in port-injected SI engines when liquid fuel is sprayed into the intake manifold and it does not completely vaporize before it collides with the top of the intake valve or intake manifold wall. This wall impingement may produce a wall film that normally results in reduced vaporization of the liquid fuel. The wall film models used in this study will be discussed in 2.4.

There have been many studies of the transport of liquid film fuel into the cylinder in port injected SI engines [23][29]. One factor Meyer and Heywood (1999) investigated was the fuel volatility and the resulting size and number of droplets entering the cylinder. Pure iso-octane and indolene, which is a multi-component fuel similar to gasoline, were tested. The iso-octane produced fewer occurrences of droplets in the cylinder while the indolene resulted in a greater proportion of larger droplets entering the cylinder for a closed valve injection. This would indicate that the multi-component nature of indolene produced a greater film thickness in the valve area [23]. Skippon and Norton [29] investigated the effect of gasoline volatility on the mass and composition of the inlet port wall film in a port-injected SI engine. They investigated cold start conditions, as well as conditions were the engine was warmed up. Their results show that as the inlet port wall temperature increased the composition of the film had an increased amount of heavy species relative to cold start conditions (approx. 80% versus 20% when the engine was cold) [29]. There have been modeling studies that look at the effect that the multi-component fuels have on droplet makeup, and they will be discussed in 2.5.

## *2.3 KIVA-3 Simulation*

The KIVA computer program was developed by Los Alamos National Laboratory and was publicly released in 1985. KIVA-3 is a program intended to provide numerical calculation of transient, two and three-dimensional, chemically reactive fluid flows and sprays [6]. The intended subject of study is applications involving the internal combustion engines, but it does have the ability to study other

systems with some modifications in the code. This section merely is intended to act as an introduction to KIVA-3 and will not cover the models used in depth except for the models which are most applicable to the subject of study. For a detailed description see [5]. This section will give a description of how the code is used, where the actual calculations most relevant to this study will be discussed in 2.5.

## *2.4 KIVA Wall Films and Vaporization Models*

The models that are most applicable to this study are the droplet vaporization and wall film models. Solving for the dynamics of spray droplets in a computational model involves complex interactions between the spray and surroundings. KIVA-3 takes into account detailed information of the droplets such as a distribution of droplet size, velocity and temperature, droplet collisions and coalescences, as well as droplet oscillations, distortions and breakup when the Weber numbers are larger than unity [26]. For a detailed description of the distribution functions as well as breakup and collision distribution functions refer to [5]. KIVA-3 uses the radius distribution function to create droplets that radii have been randomly sampled about the Sauter Mean Radius. This distribution pattern was based on experimentally observed data [5].

### 2.4.1 Overview of droplet calculations

The complete droplet calculations can be reviewed in depth in [5] but the main evaporation terms are included here for review.

The Frossling correlation [5] describes the rate of droplet radius change R:

$$R = -\frac{(\rho D_{air})(\hat{T})}{2\rho_d r}\frac{Y_1^{*-} - Y_1}{1 - Y_1^*} Sh_d \qquad \text{Equation 3}$$

where $Sh_d$ refers to the Sherwood number for mass transfer defined as:

$$Sh_d = (2.0 + 0.6\,\mathrm{Re}_d^{\frac{1}{2}} Sc_d^{\frac{1}{3}})\frac{\ln(1+B_d)}{B_d}$$

*Re* refer to the Reynolds number and $Sc_d$ and $B_d$ are given as:

$$\mathrm{Re} = \frac{\rho u d}{\mu}\ , \quad Sc_d = \frac{\mu_{air}(\hat{T})}{\rho D_{air}(\hat{T})}\ \text{, and}\ B_d = \frac{Y_1^* - Y_1}{1 - Y_1^*}$$

$Y_1^*$ is the fuel vapor mass fraction at the droplet's surface and $Y_1 = \frac{\rho_1}{\rho}$ and $(\rho D)_{air}(\hat{T})$ refers to the fuel vapor mass fraction and diffusivity in air[5].

The energy balance on the droplet is used to determine the droplet's rate of temperature change [5]:

$$\rho d\,\frac{4}{3}\pi r^3 c_l \dot{T} d - \rho_d\, 4\pi r^2 RL(T_d) = 4\pi r^2 Q_d \qquad \text{Equation 4}$$

where $c_l$ refers to the liquid specific heat, the *L(Td)* term is the latent heat of vaporization and the heat conduction per unit area to the droplet surface is $Q_d$.

### 2.4.2 Wall film calculations

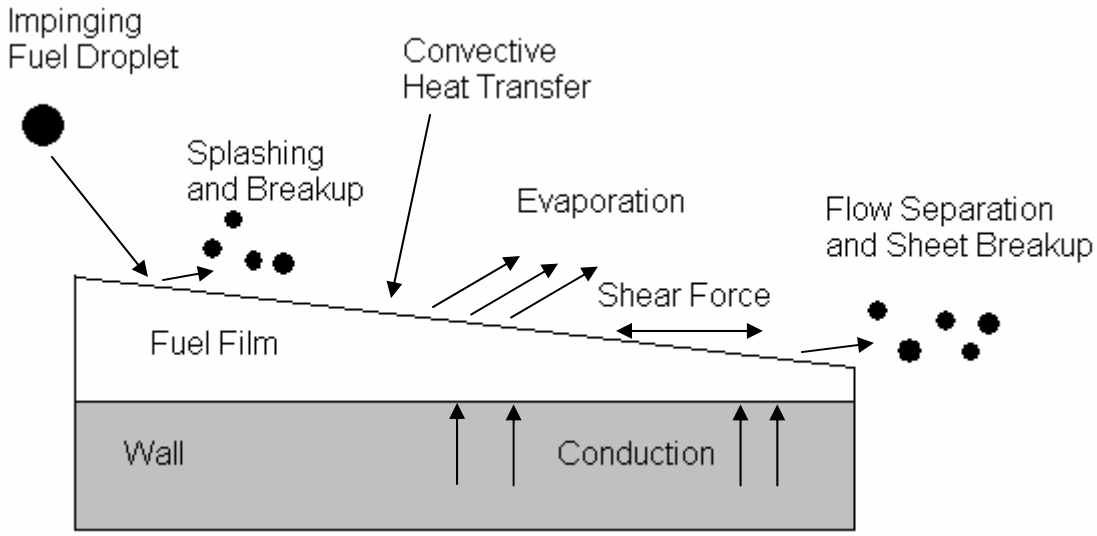


*Figure 2: Physical Phenomena in Fuel Film [22]*

Figure 2 shows the major physical processes affecting the liquid film. The interaction between the spray and wall are significant for PFI gasoline engines. The wall film is assumed to be well mixed such that the temperature and composition are constant throughout the liquid film. This assumption is valid due to the interactions between the gas flow above the film, the impinging spray and the wall film. These interactions provide a reasonable assumption that the liquid film is well mixed.

Spray-wall impingement is handled in a separate subroutine that first determines if a particle has hit a wall based on its velocity and position. There are 4 droplet-wall regimes that KIVA considers stick, rebound, spread and splash. The most applicable to this study are the spread and splash regimes due to the injection velocities. The spread regime is used if the Weber number of the droplet meets the following criteria [5]:

$$10 < We < 18.0^2 d_d \left(\frac{\rho}{\sigma}\right)^{\frac{1}{2}} v^{\frac{1}{4}} f^{\frac{3}{4}}$$

$$\text{where } We = \frac{\rho u^2 r}{a}$$

based on the liquid $\rho$ the density, $\sigma$ the surface tension, $v$ the kinematic viscosity, $f$ the frequency of drops colliding with the film, $a$ is surface tension coefficient, and $d_d$ the droplet diameter. During a spread event, the entire droplet is absorbed into the liquid film. If the Weber number is greater than $18.0^2 d_d \left(\frac{\rho}{\sigma}\right)^{\frac{1}{2}} v^{\frac{1}{4}} f^{\frac{3}{4}}$, the splash regime is used and multiple other droplets are created and leave the surface [5].

## *2.5 Multi-component Fuel Modeling*

### 2.5.1 Multi-component model

Continuous thermodynamics, or thermodynamics of continuous mixtures, is one method of analyzing the vaporization of a fuel droplet that is composed of a wide range of hydrocarbons. The mixture is defined by a distribution function representing the mixture of a homologous family of compounds. The distribution function in the model used in KIVA-3 release 2 is the Γ-distribution function [22]. The required transport equations were derived in detail by Tamim and Hallet (1995) [33] and implemented in KIVA by Andreas Lippert (1999) [22]. The derivations will not be covered in depth but the resulting equations will be discussed.

The Continuous Thermodynamics Method uses a mass basis, where $y_i$ is the mass fraction of the fuel species, $\Delta I_i$ is the interval in molecular weight and *I* is centered about the value of I corresponding to species I [22]:

$$y_i = f(I)_i \Delta I_i \qquad \text{Equation 5}$$

such that the integral of the distribution satisfies the constraint

$$\int_0^\infty f(I)dI = 1 \qquad \text{Equation 6}$$

.

The Γ-distribution was chosen because it had been shown to have the ability to adequately represent fuel properties [12][33][37]. The Γ-distribution is given as [12]:

$$f(I) = \frac{(I-\gamma)^{\alpha-1}}{\beta^\alpha \Gamma(\alpha)} \exp\left(-\frac{(I-\gamma)}{\beta}\right) \qquad \text{Equation 7}$$

such that the mean $\theta$ and the variance $\sigma$ on a molar basis are defined as:

$$\theta = \alpha\beta + \gamma \text{ and } \sigma^2 = \alpha\beta^2$$

The distribution parameters $\alpha$, $\beta$ and $\underline{\gamma}$ control the shape of the distribution and Γ refers to the gamma function. The liquid droplet composition and the vapor-liquid equilibrium are based on a molar distribution [22]. The mass and molar distribution can be related through the following relation [22]:

$$f_{mass}(I)dI = f_{molar} \frac{I}{\theta_{molar}} dI \qquad \text{Equation 8}$$

For the case where γ=0, the molar and mass means can be simplified to [22]:

Mean Mass: $\bar{\theta} = (\alpha+1)\beta$ and the Mean Molar: $\hat{\theta} = \alpha\beta$

The fuel distribution parameters for gasoline have been derived in [33] and shown in Table 1.

*Table 1: Multi-component Gasoline Distribution Parameters [33]*

| Gasoline | |
|---|---|
| α | 5.7 |
| β | 15 |
| γ | 0 |
| θ | 85.5 |
| σ | 35.8 |

The multi-component model was compared to the single-component KIVA-II standard model and experimental data for a cold start from the results of Hiroyasu et al (1974) to compare the temporal variation in drop size during simulation time. The results showed that the multi-component model predicted the temporal variation in droplet size much better than the standard single component version of KIVA-II.

A comparison of the vaporization of iso-octane and multi-component gasoline was conducted by Zhu and Reitz [38]. They showed that the mean molecular weight of the droplets increased during the droplet lifetime such that the mean molecular weight was nearly twice that of iso-octane after 8ms in a 30atm 500k environment where the initial droplets were 20 microns in diameter. Zhu and Reitz showed that the droplet lifetime of the multi-component gasoline was longer than that of the iso-octane droplets. It was shown that the multi-component gasoline droplet never

followed the $D^2$ law but the iso-octane droplet, while spending most of the simulation in the heat up time, did follow the $D^2$ law during the late vaporization period [38].

The multi-component model was also used in a study by Ra and Reitz (2003). Sprays of iso-octane and gasoline were compared in a gasoline direct injection computational grid. They showed that the vaporization of the gasoline was greater than the single component iso-octane sprays during the same simulation conditions. The mean molecular mass of the liquid gasoline in the cylinder was seen to be increasing during the injection, and began increasing more rapidly after the injection was finished because no more new fuel was entering the cylinder. This is applicable to this study because as the mean molecular mass of the droplets increases due to the lighter elements in the gasoline vaporizing faster than the heavier elements, we would expect the remaining heavier hydrocarbons to be the main components of the impinged fuel film.

### 2.5.2 Multi-component governing equations

Zhu and Reitz [38] give a general governing equation for the various moments of the liquid fuel distribution. This governing equation uses a non-convective two-zone drop model for which gas absorbed in the outer layer of the liquid drop is assumed exist only in the outer layer of the liquid drop. The study presented does not consider gas absorption so a simplified form of the general governing equation can be obtained from as [38]:

$$\frac{c_1 R}{3}\frac{d\left(\theta^n\right)^1}{dt} - \dot{m}\left(\theta^n\right)^1 = \left[\nabla \cdot \int_0^\infty \tau^n J_\tau - y_f\left(\theta^n\right)^v \dot{m}\right]_{R^+} \quad (n = 0,1,2,\ldots) \quad \text{Equation 9}$$

where $R$ is the drop radius, $\tau$ is molecular weight and $J_\tau$ is the diffusion flux. $\left(\theta^n\right)^1$ and $\left(\theta^n\right)^n$ are the $n$th moments of the distribution of the liquid fuel and vapor and defined by:

$$\left(\theta^n\right)^p = \int_0^\infty \tau^n f^p(\tau) d\tau \quad (n=0,1,2,\ldots) \quad \text{Equation 10}$$

Any number of equations can be obtained with Equation 10 for different values of n. For a two-parameter distribution, $n=2$ suffices to describe the variation in liquid composition with time through vaporization [38]. With the assumption of gas-phase steadiness, unity Lewis number, and correction for convective effects the vaporization rate can be written as [38]:

$$\dot{m} = \frac{c_g \overline{D}}{2R}\ln(1+B)\left(2.0 + 0.6\,\mathrm{Re}^{\frac{1}{2}} Sc^{\frac{1}{3}}\right) \qquad \text{Equation 11}$$

for n=0. where B is the Spalding number:

$$B = \frac{\left(y_{f,s} - y_{f,\infty}\right)}{\left(1 - y_{f,s}\right)}$$

and $c_g$ is the specific heat of the fuel vapor. $Sc$ is the Schmidt number and $Re$ is the Reynolds number.

A differential form of the governing equation for wall film mass can be written as [38]

$$\frac{\partial\left[\left(\theta^n\right)^1 h\right]}{\partial t}+\frac{1}{A_{wall}}\sum_{j=1}^{N_{side}}\left(\theta^n\right)^1\left[\left(\vec{V}_f-\vec{V}_w\right)\cdot\vec{n}\right]_j h_j L_j=\dot{M}_{imp}+\dot{S}_{imp} \qquad \text{Equation 12}$$

where $h$ is the wall thickness, $V_f$-$V_w$ is the relative velocity between the wall film and the wall, $A_{wall}$ is the wall film area, and $L_j$ is the length of the $j$th side of the wall film. $M_{imp}$ and $S_{imp}$ are the corresponding source terms related to the effects of the wall film vaporization and spray impingement, respectively. $\dot{Q}_{imp}$ is the source term related the impinging spay drops.

The energy equation for the wall film with the assumption of being well mixed is [38]:

$$\rho_1 h C_{vl}\left\{\frac{\partial T_1}{\partial t}+\sum_{j=1}^{N_{side}}\left[\left(\vec{V}_f-\vec{V}_w\right)\cdot\vec{n}\right]_j L_j T_l\right\}=h_1\left(T_{wall}-T_1\right)+h_2\left(T_{cell}-T_1\right)+\dot{Q}_{imp} \qquad \text{Equation 13}$$

where $\rho_1$, $C_{vl}$, $T_1$, $T_{wall}$ and $T_{cell}$ are the film density, film specific heat, wall temperature, and the gas temperature of the cell involving the film, respectively. $h_1$ and $h_2$ are the convective heat transfer coefficient between the film and the wall and that between the film and the gas, respectively.

# 3 METHODOLOGY

## *3.1 Computational Grid*

The computational grid was provided by Mercury Marine and was used for previous fuel injection simulations. The grid included the outer surface of the heat exchanger shell (not the internal geometry of the heat exchanger), intake manifold, combustion cylinder, and exhaust manifold. The grid contained 10 regions with 163,858 computational cells. The injector is placed in the intake manifold; the combustion chamber has a pent-roof design with slanted valves.

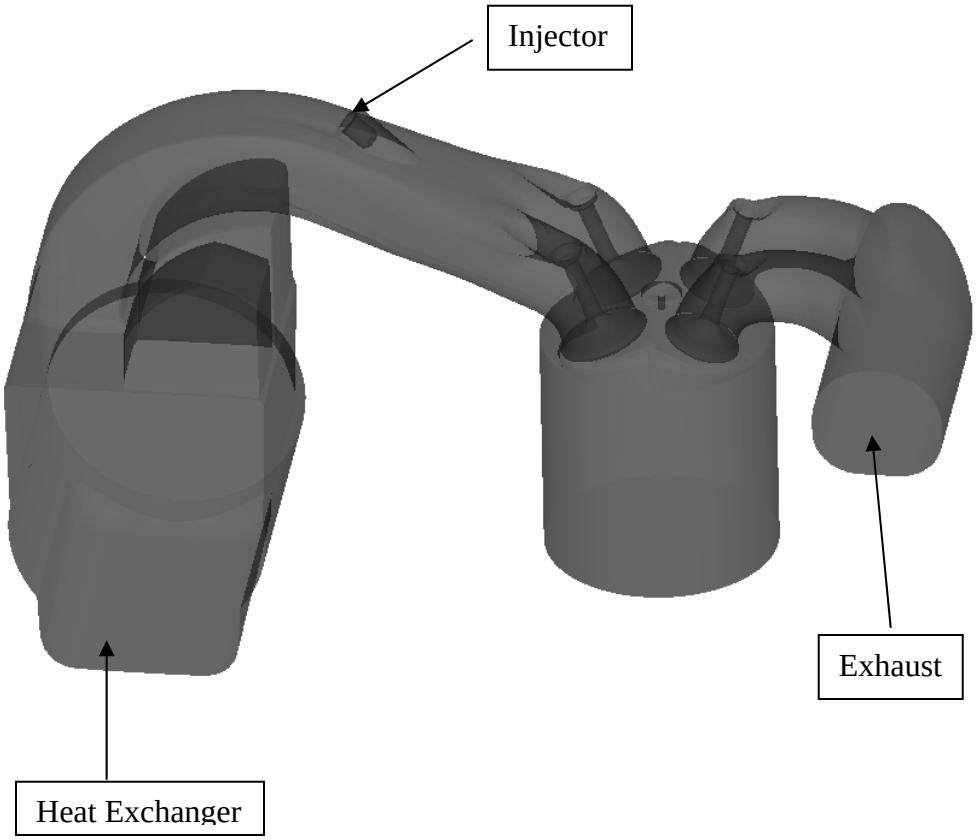


*Figure 3: Overview of Verado Grid*

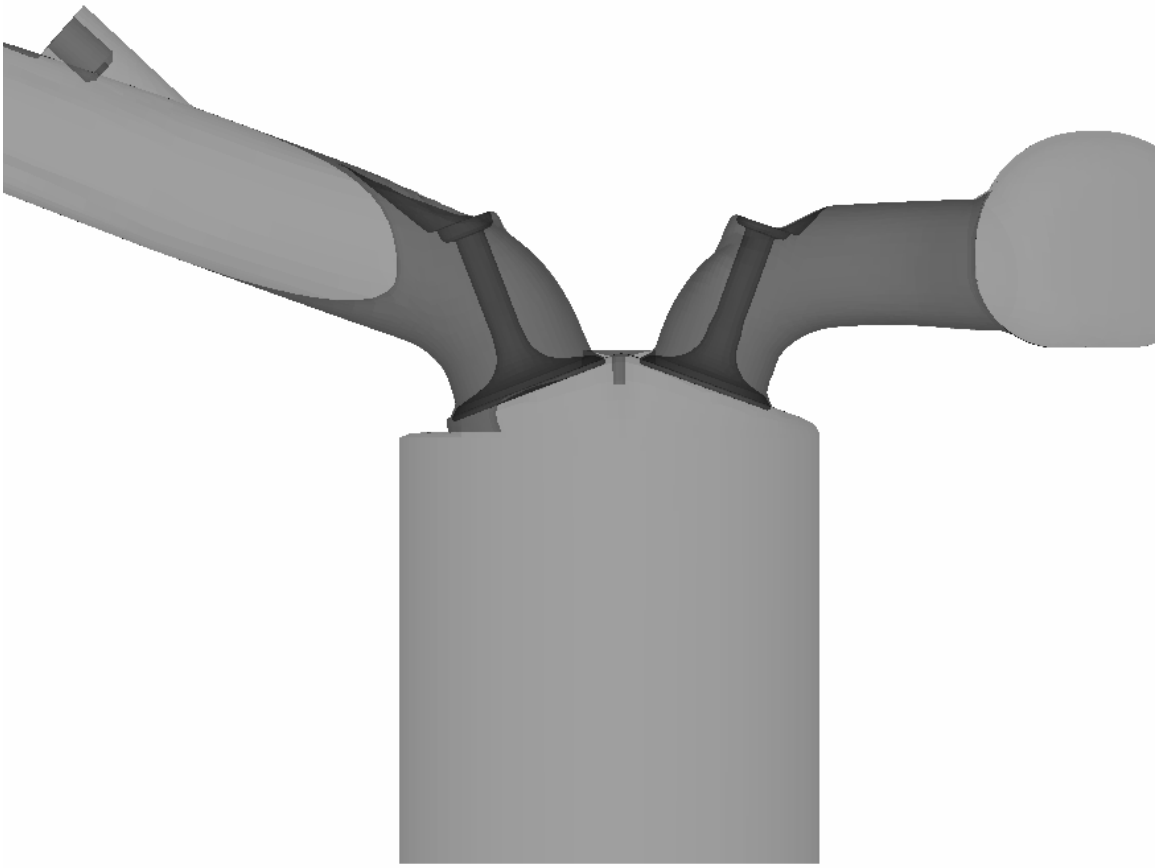

*Figure 4: Side Profile of Intake, Cylinder and Exhaust*

Two simulation conditions were examined in this study. Both conditions are high load, high speed conditions which it is believed that heavy fuel impingement is occurring due to the large amount of fuel being injected along with high engine speed and relatively cool wall conditions.

*Table 2: Simulation ERC1 Parameters [24]*

| | |
|---|---|
| Engine Speed | 6100rpm |
| Intake Manifold Pressure | 179.9kPa |
| Intake Manifold Air Temperature | 50.0°C |
| Injection Velocity | 3150cm/s |
| Injection Mass | 71.79mg/cycle |
| Injection Duration | 12.57ms (19.6 ms cycle duration) |

*Table 3: Simulation ERC2 Parameters [24]*

| | |
|---|---|
| Engine Speed | 4897rpm |
| Intake Manifold Pressure | 125.0kPa |
| Intake Manifold Air Temperature | 37.0°C |
| Injection Velocity | 2250cm/s |
| Injection Mass | 49.42mg/cycle |
| Injection Duration | 8.83ms (24.6 ms cycle duration) |

*Table 4: Engine Parameters [24]*

| | |
|---|---|
| Bore | 82mm |
| Stroke | 81mm |
| Displacement | 0.855 Liters |
| Connecting rod | 133mm |
| Valve Timings (deg)<br>(After TDC of intake stoke):<br>IVO<br>IVC<br>EVO<br>EVC | <br><br><br>-44<br>256<br>442<br>778 |

The simulation characteristics are shown in Table 2 and Table 3. The simulations were compiled based on information provided by Mercury Marine at different engine conditions. Hexane ($C_6H_{14}$), Iso-octane ($C_8H_{18}$), and tetradecane ($C_{14}H_{30}$) were chosen as the single-component fuels for simulation in order to provide insight into the effects of different fuel volatility. The full set of input parameters are shown in Appendix B.

## *3.2 Rezoning subroutine*

The rezoning subroutine developed for this study was created with the help of Randy Hessel of the Engine Research Center. The specific rezoning subroutine developed for this grid is a modification of a general rezoning subroutine that Randy Hessel had developed for other KIVA projects. The rezoning subroutine uses multiple interpolations and grid relaxations in the engine cylinder to move grid points into positions that allow for seamless grid movement while avoiding misshapen computational cells. A detailed description of the rezoning subroutine is shown in Appendix A.

## *3.3 Sub-models Used*

*Table 5: Sub-models Used*

| **Process** | **Model** |
|---|---|
| Turbulence | Conventional K-ε Model<br>Modified RNG K-ε Model<br>Han and Reitz(1996) |
| Wall Heat Transfer | Compressible, Unsteady Wall Functions<br>Han and Reitz (1996) |
| Injection Profile | Square wave |
| Collision model | O'Rourke model |
| Wall Impingement Model | Rebound/Slide Model<br>Naber (1988) |
| Spray Breakup | TAB breakup Model<br>O'Rourke (1987)<br>Reitz (1987) |
| Multi-Component Fuel | Continuous Thermodynamics Method<br>Lippert (1999) |

A combustion model was not used because of the increased computational time required for the simulation. The combustion would add additional thermal energy into the simulation which would reduce any in cylinder fuel impingement but this model will serve as a predictor of where fuel impingement is occurring. The conventional k-epsilon model was used in KIVA3v simulations and the modified RNG K-ε model [14] was used in KIVA3v Release 2 simulations. The temperature wall function model [15] was used to predict the gas-wall convective heat transfer. This model allows for the use of a coarse grid near the wall but maintains accurate

heat transfer predictions. The wall impingement model assumes the velocity of a particle is parallel to the wall when it impinges and was proposed by Naber (1988). This model provides movement of the particles and thus the fuel film, due to airflow over the surface. The injection spray was a pulse injection of which the particles were distributed using the χ-squared distribution around a Sauter Mean Radius of 2.5e-3 cm. The distribution of fuel droplets is [6]:

$$f(r) = \frac{1}{\bar{r}} \exp^{\left(\frac{-r}{\bar{r}}\right)} \qquad \text{Equation 14}$$

where $\bar{r}$ is the number-averaged drop radius and is related to the input Sauter Mean Radius by:

$$\bar{r} = \frac{1}{3} r_{SMR} .$$

The breakup model used was the TAB breakup model [26]. The KIVA3v Release 2 multi-component simulations used the Continuous Thermodynamics Method [22].

## *3.4 Single-component Model*

### 3.4.1 Simulation Background

The single-component simulation used KIVA3v as the computational software and ran on a Linux cluster. The single component model used $C_6H_{14}$, $C_8H_{18}$ and $C_{14}H_{30}$ as test fuels to study how the varying molecular mass affected the fuel impingement. This model was used as an initial debugging simulation because the rezoning subroutine and simulation parameters had to first be developed. KIVA3v does not have multi-component fuel capabilities but development of the rezoning

subroutine was done using this version of KIVA because the code was available with the modifications necessary for a custom rezoning subroutine already in place. Once the rezoning subroutine was developed and simulation parameters established, the rezoning subroutine and simulation parameters were transferred to KIVA3v Release 2 with modifications only needed to allow for the custom rezoning subroutine. This allowed for faster development of the rezoning subroutine, and also a set of results could be compared with KIVA3v Release 2 results.

### 3.4.2 Simulation Parameters

The models used wall temperatures of 418K for the cylinder wall, 448K for the head, and 498K for the piston surface based on values obtained from Mercury Marine. The intake temperature was 435K while the ambient pressure was 179kPa. The inflow and outflow were 435K and 179kPa.

### 3.4.3 Fuel Injection Characteristics

The $C_{14}H_{30}$ simulations used injection velocities that were reduced to nearly half of the calculated injection velocities because the higher injection velocities caused errors in the $C_{14}H_{30}$ simulation. $C_{14}H_{30}$ simulations were conducted using an injection velocity of 1400cm/s where the other fuels were injected at 3150cm/s and 2275cm/s for simulations ERC1 and ERC2. The sprays conditions were developed based on information received from Mercury Marine. The injector had 2 nozzles which sprayed in 2-full-cone sprays that were directed at the base of the intake valves. The numbers of parcels in each injection were modified to allow for longer

simulation durations. The numbers of parcels were 1000 for $C_6H_{14}$ and $C_8H_{18}$ while the $C_{14}H_{30}$ simulations used 3000 parcels per injection. Parcels are groups of droplets that are grouped together. In three dimensional simulations, it is generally accepted that the number of parcels can vary from 1000-4000.

### 3.4.4 Selection of Single-component Fuels

The single-component simulations were conducted with three test fuels intended to cover the range of the expected multi-component distribution. This gave a good indication of how large of an effect the multi-component fuel would have on the wall impingement.

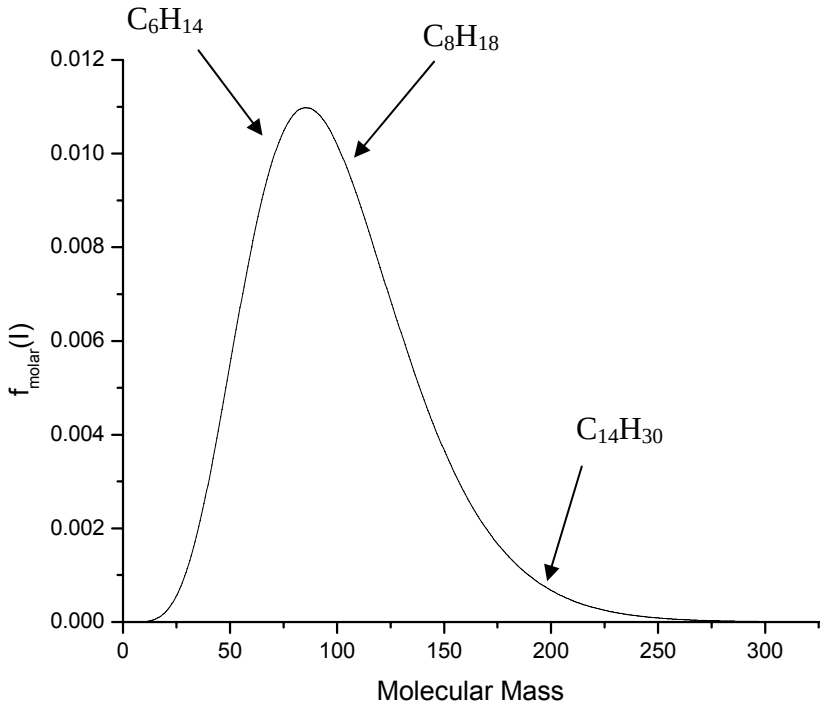

shows the multi-component distribution of gasoline based on [33]. $C_6H_{14}$, $C_8H_{18}$ and $C_{14}H_{30}$ were chosen to examine how the light, middle and heavy fuel portions of the distribution would differ.

## *3.5 Multi-component Model*

The KIVA3v Release 2 simulations used the same fuel injection characteristics as the KIVA3v simulations but used slightly different temperatures and pressures due to additional information supplied by Mercury Marine. The KIVA3v simulations still provide insight into how significant the multi-component effects of the fuel will be. The models used wall temperatures of 373K for the cylinder wall, 373K for the head, and 373K for the piston surface based on values obtained from Mercury Marine. The intake temperature was 323K while the ambient pressure was 179kPa. The inflow and outflow were 323K and 179kPa.

# 4 SINGLE COMPONENT RESULTS

## *4.1 Overview of Single-component Model*

The single-component study was conducted with KIVA3v. This version of KIVA does not have multi-component subroutines and uses single component fuels. KIVA3v was chosen to run the single component simulations because it runs faster than KIVA3v Release 2 and was a useful tool for the rezoning subroutine development and code debug.

## *4.2 Fluid Flows*

Figure 5 show the valve lift profiles used in the simulation along with the injection period for both test case ERC1 and ERC2. The simulation started at -180° ATDC so the first injection begins shortly after the start of the simulation and was allowed to run for approximately 1200°ATDC, which was limited due to the film thicknesses becoming a significant portion of the cell height. The current wall film model assumes that the wall film thickness is small compared to the cell height and encounters temperature convergence issues when this assumption is not valid. The hope was to run for a long enough period that a steady state film was established in the intake system.

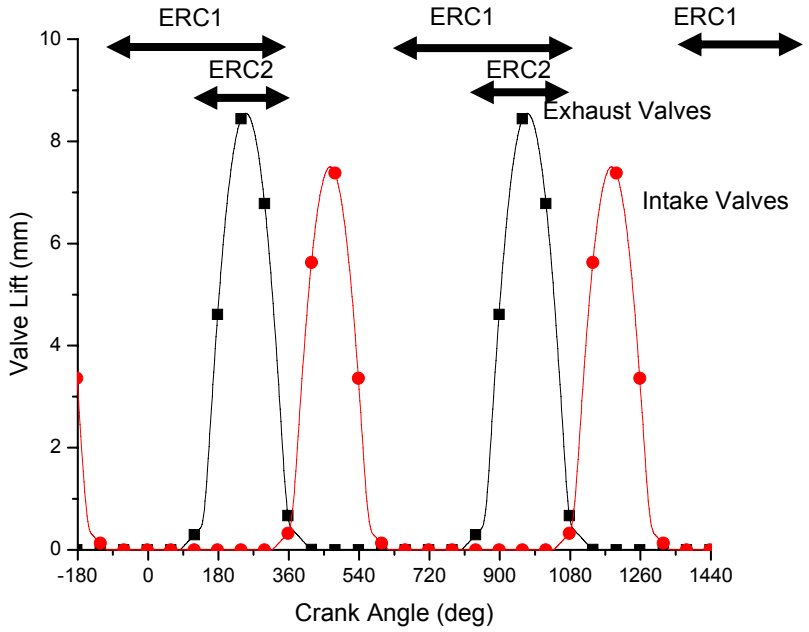


*Figure 5: Valve Lift and Injection Durations*

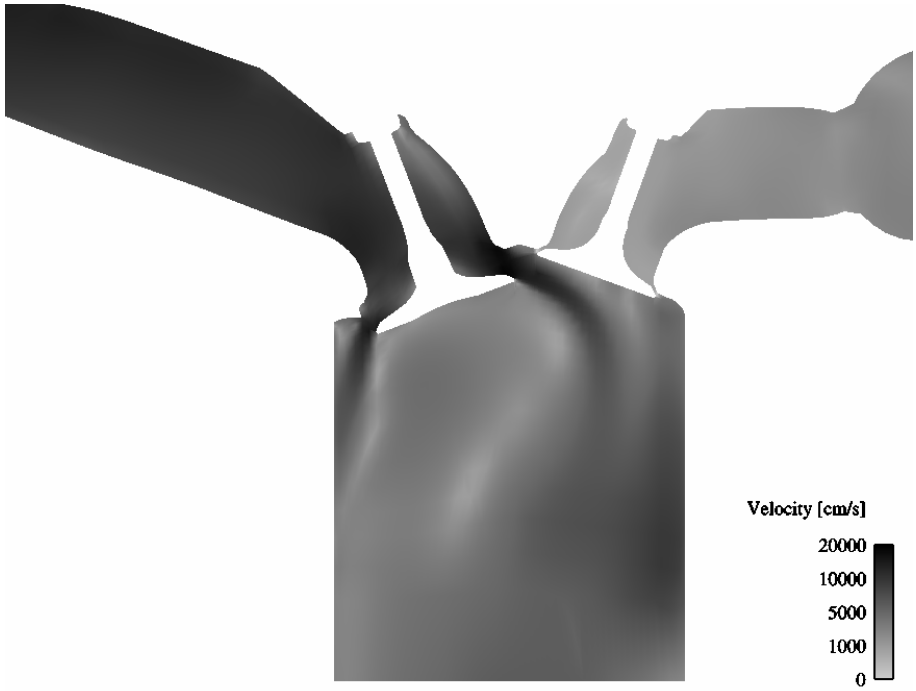


*Figure 6: Velocity Profile During Injection*

The fluid velocities, Figure 6, show very fast airflows around the valve during the intake stroke. These high-velocity flows would be expected to carry liquid fuel that impinged in the intake manifold or on the intake valves towards and possibly into the cylinder.

## *4.3 Wall-film results*

The single-component study was conducted at the ERC1 and ERC2 conditions. Figure 7 shows the liquid fuel in the grid during the ERC1 simulation for $C_6H_{14}$, $C_8H_{18}$, and $C_{14}H_{30}$. The lower vaporization of $C_{14}H_{30}$ is clearly shown as the amount of liquid fuel in the grid is substantially larger than both $C_8H_{18}$ and $C_6H_{14}$, and it closely matches the total injected quantity after 2 cycles. The $C_6H_{14}$ is close to reaching a steady-state amount of liquid fuel in the grid where the cyclic amount of fuel in the grid does not change cycle to cycle. $C_8H_{18}$ has not reached this steady-state fuel cycle but the increase in the amount of fuel in each cycle does appear to be decreasing, suggesting that the $C_8H_{18}$ is close to reaching its steady-state cycle. At the end of the 1$^{st}$ injection there is approximately 50mg of liquid fuel, but after the 2$^{nd}$ injection it is approximately 75mg, showing a decreasing contribution.

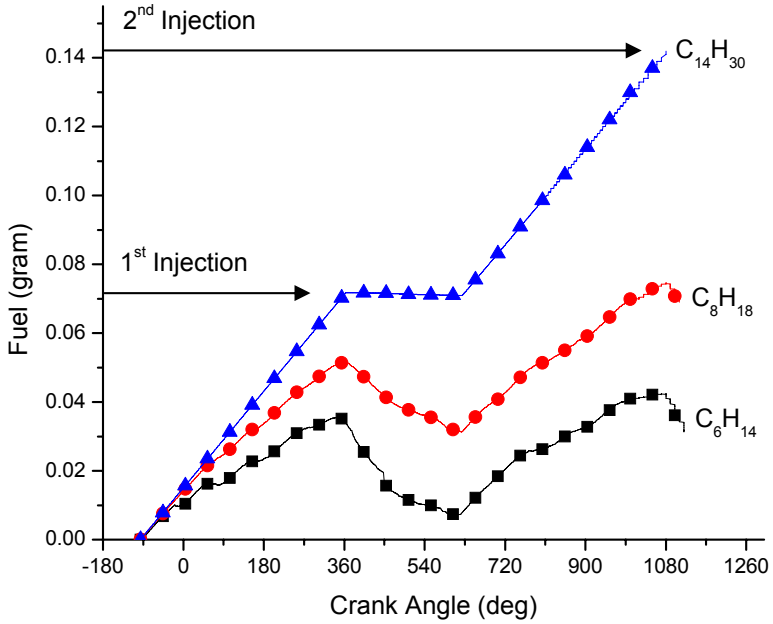


*Figure 7: ERC1 Liquid Fuel in Grid*

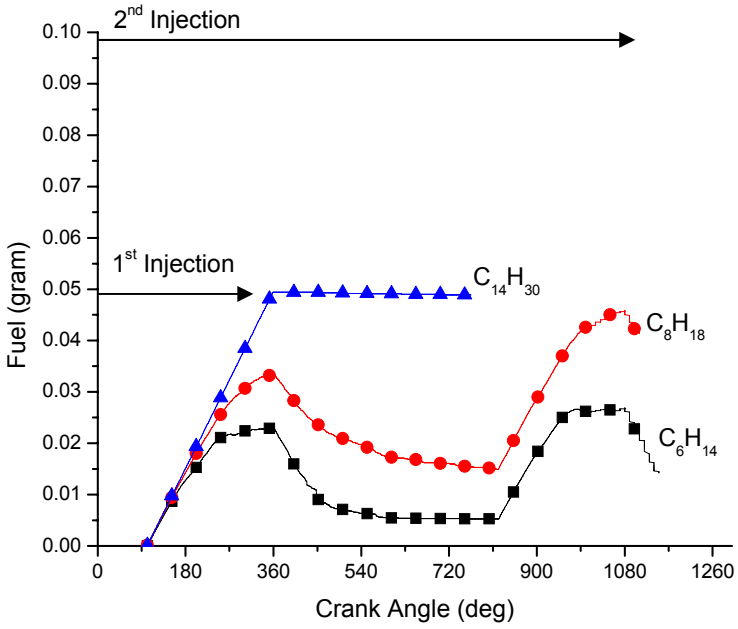


*Figure 8: ERC2 Liquid Fuel in Grid*

The ERC2 simulation results are shown in Figure 8 and are similar to the results of the ERC1 simulation. The $C_6H_{14}$ simulation appears to be nearing a steady-state cycle of fuel in the grid while the $C_8H_{18}$ simulation is still showing an increasing amount of fuel in the grid during each cycle. The $C_{14}H_{30}$ simulation encountered temperature convergence issues due to the wall film height in small cells such that the simulation had a shorter duration

Figure 9 shows the regions that were defined to further classify the location of the liquid fuel films.

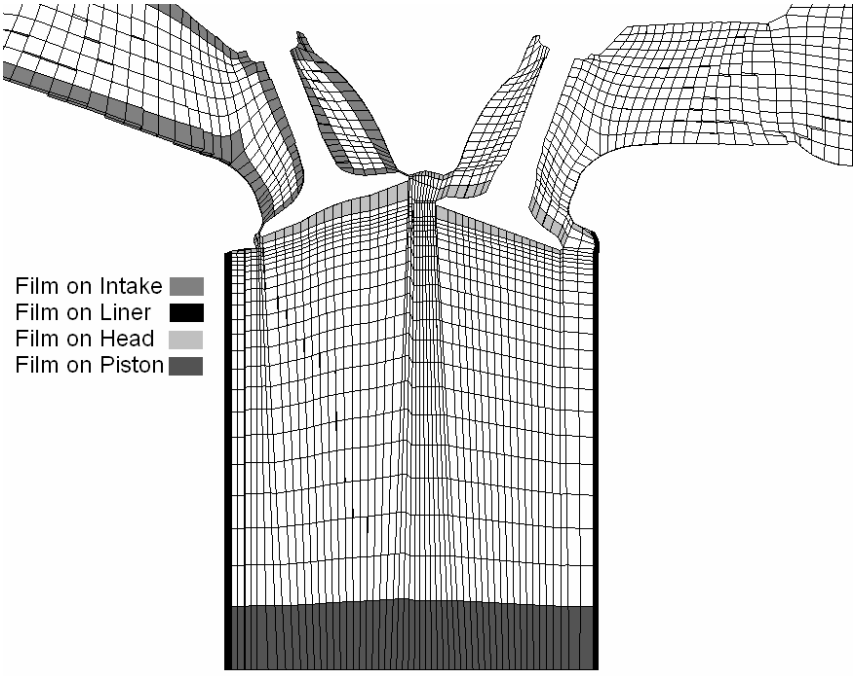


*Figure 9: Regions of Fuel Film in Grid*

The total fuel film mass was calculated in each region. The intake region included any areas that were not in cylinder. The liner region included any wall cells

that were on the wall of the cylinder, and also include the corner cell on the piston-liner. The piston region included all cells on the piston crown but not the corner cells with the liner. The head region included all wall cells above the flat portion of the head. The total film is the summation of all of the previously mentioned regions, and the difference between this and the total fuel injected is liquid fuel not yet impinged or vaporized.

Figure 10 thru Figure 15 show the fuel film results for simulation ERC1. The results of all 3 different test fuels show that the fuel impingement is occurring almost exclusively in the intake manifold and on the intake valves. The amounts of adhered fuel at the end of the simulations vary from 20mg for $C_6H_{14}$ to 100mg for the $C_{14}H_{30}$ simulation. The $C_8H_{18}$ simulation has 55mg of fuel impinged at the end of the simulation with 5mg occurring in the head region of the cylinder. This fuel appears to have been transported into the head region during the intake stroke from the existing wall-film in the intake manifold.

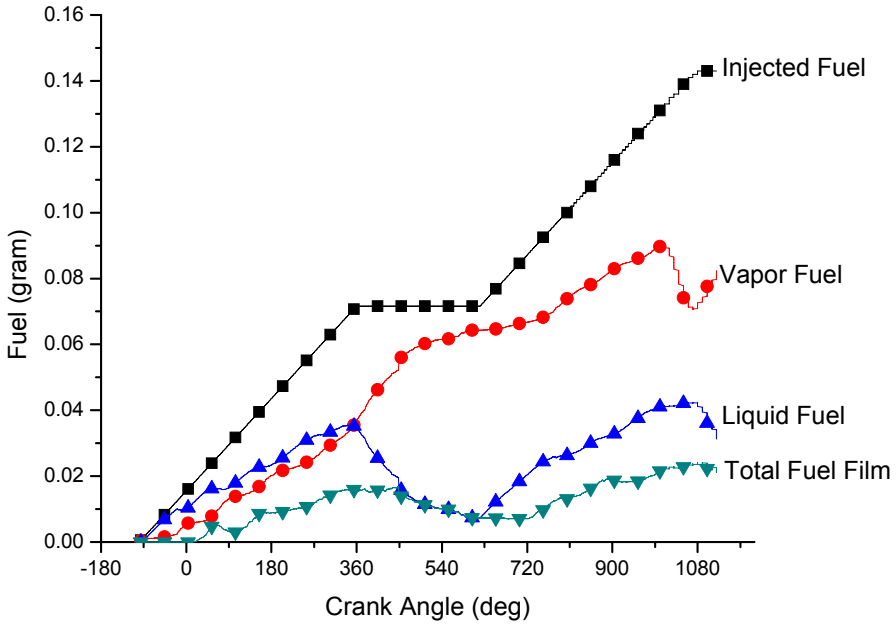


*Figure 10: ERC1 $C_6H_{14}$ Fuel in Grid*

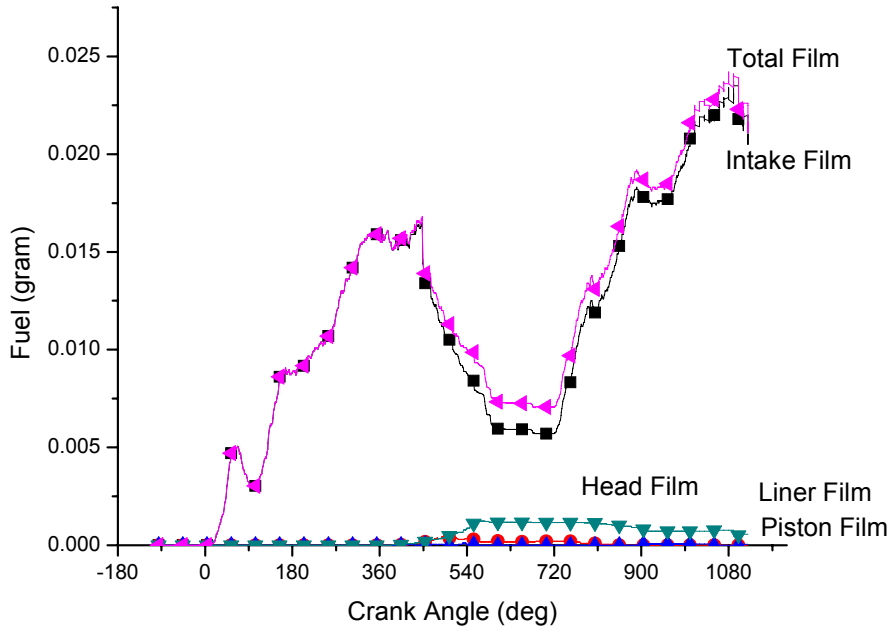


*Figure 11: ERC1 $C_6H_{14}$ Fuel Film Results*

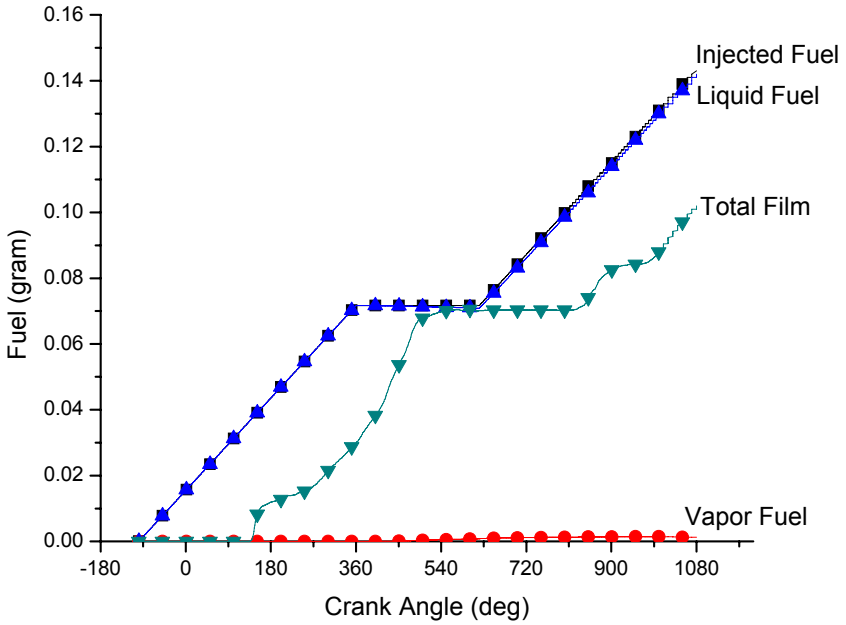


*Figure 12: ERC1 $C_{14}H_{30}$ Fuel in Grid*

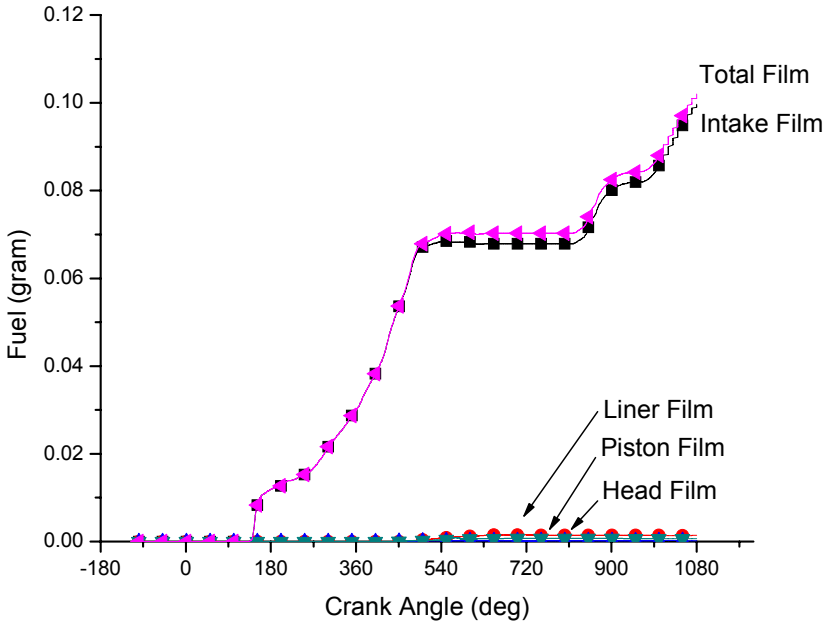


*Figure 13: ERC1 $C_{14}H_{30}$ Fuel Film Results*

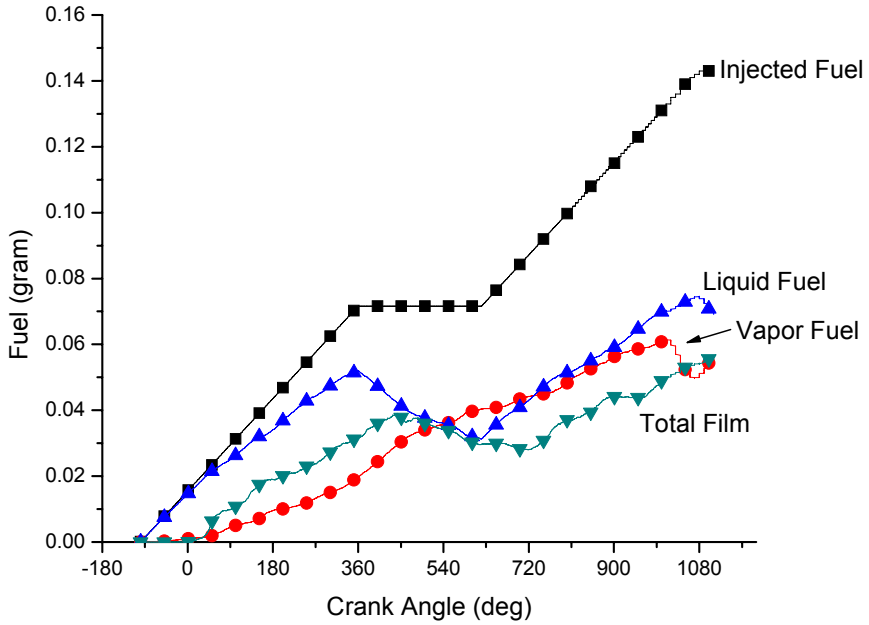


*Figure 14: ERC1 $C_8H_{18}$ Fuel in Grid*

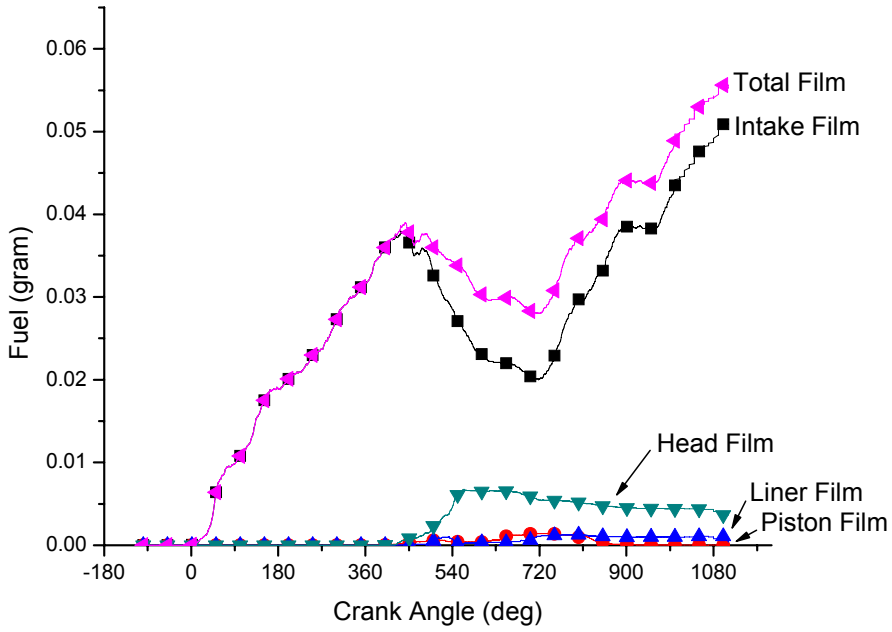


*Figure 15: ERC1 $C_8H_{18}$ Fuel Film Results*

Figure 16 thru Figure 21 show the fuel film results for simulation ERC2. The results of all 3 different test fuels show that the fuel impingement is occurring almost exclusively in the intake manifold and on the intake valves. The amounts of adhered fuel impingement at the end of the simulations vary from 10mg for $C_6H_{14}$ to 49mg for the $C_{14}H_{30}$ simulation. The $C_8H_{18}$ simulation has 29mg of fuel impinged at the end of the simulation with film almost exclusively occurring in the intake manifold.

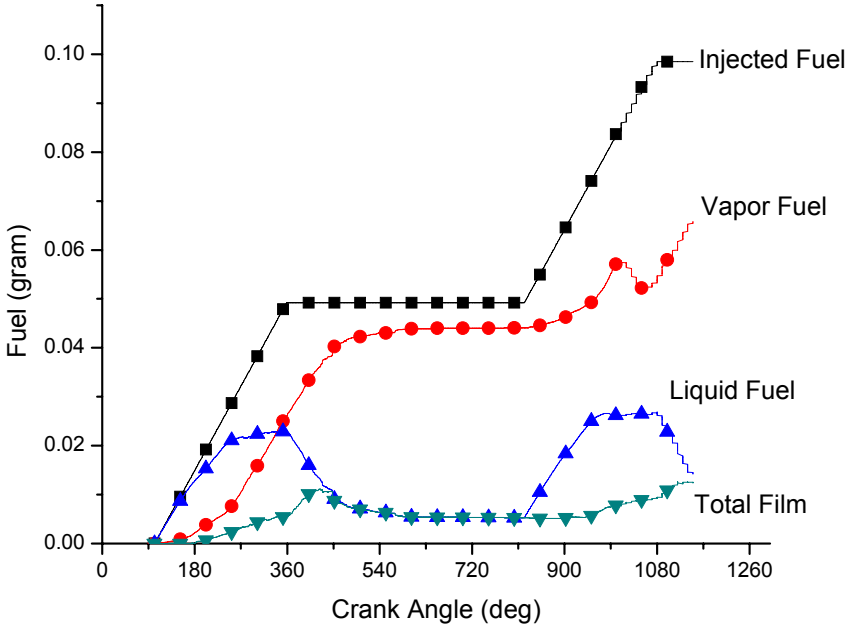


*Figure 16: ERC2 $C_6H_{14}$ Fuel in Grid*

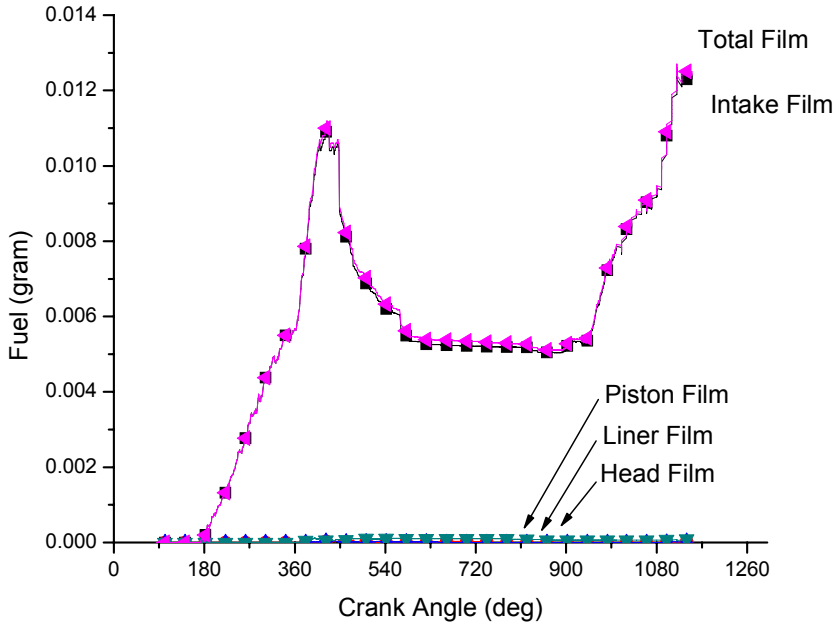


*Figure 17: ERC2 $C_6H_{14}$ Fuel Film Results*

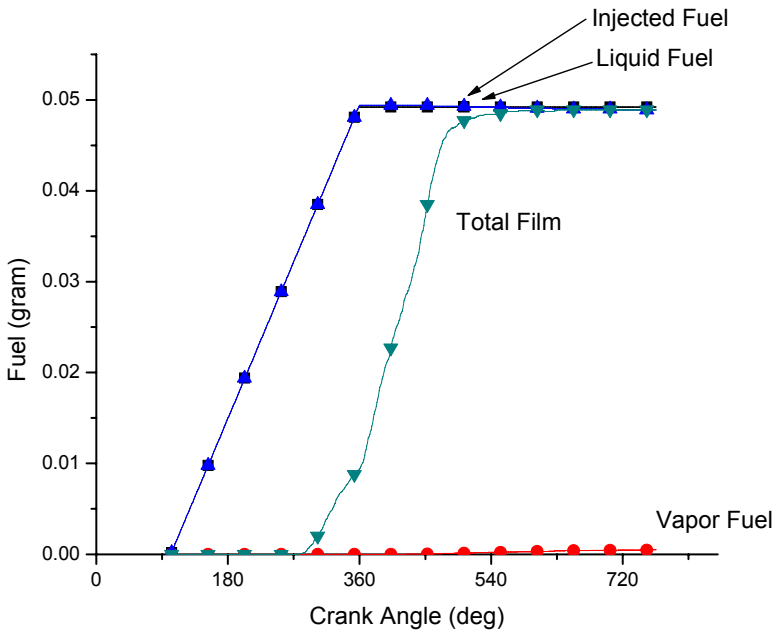


*Figure 18: ERC2 $C_{14}H_{30}$ Fuel in Grid*

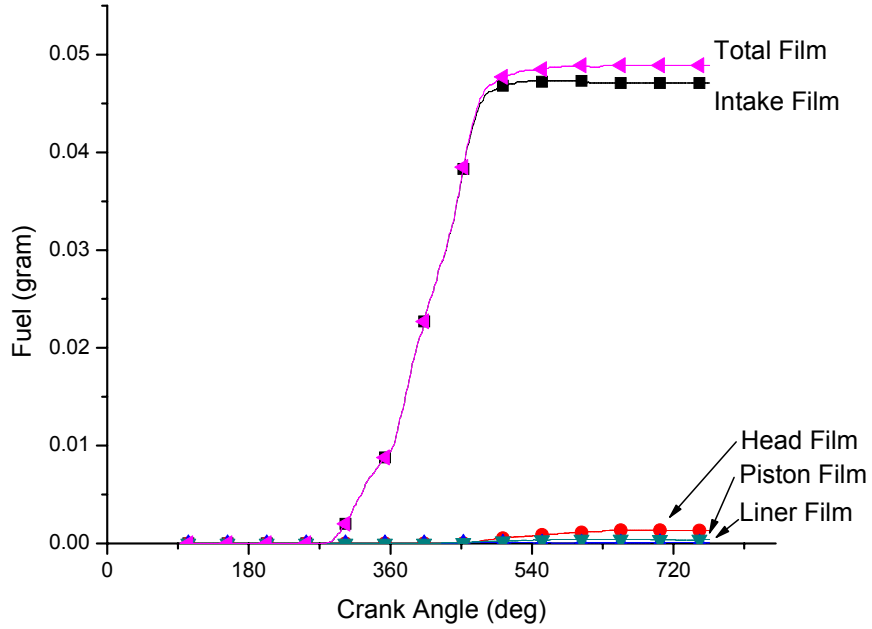


*Figure 19: ERC2 $C_{14}H_{30}$ Fuel Film Results*

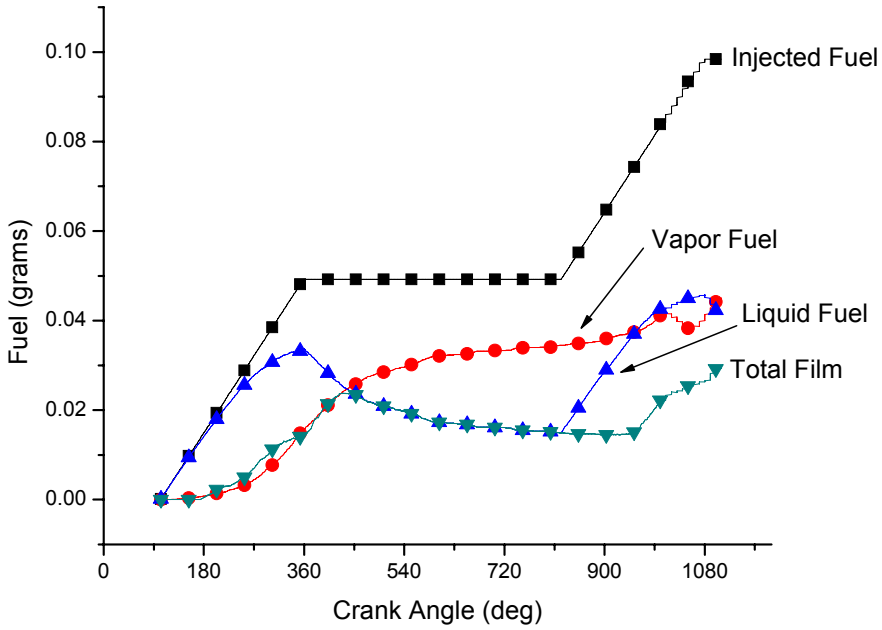


*Figure 20: ERC2 $C_8H_{18}$ Fuel in Grid*

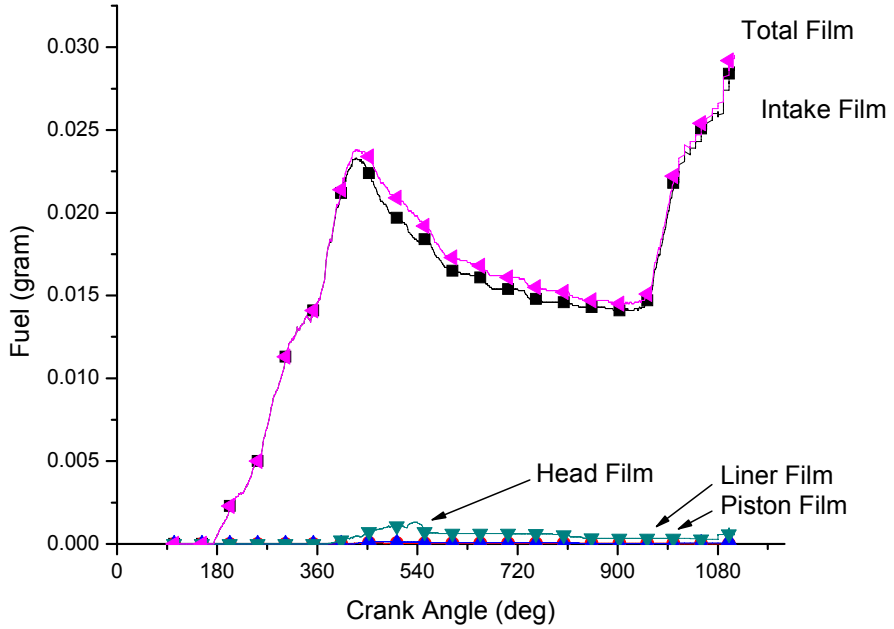


*Figure 21: ERC2 $C_8H_{18}$ Fuel Film Results*

## *4.4 Wall-film Location and Translation*

Figure 22 thru Figure 27 show representative top and side views for all 3 single-component fuels at the end of simulation ERC1. At this time all of the simulations have completed approximately 1300 crank angles, almost 2 full cycles. The mass of adhered fuel is noticeably different between the 3 different fuels, which would be expected from the previous mass results. The $C_6H_{14}$ simulation, Figure 22 and Figure 23, shows fuel films in the intake manifold, mainly located on the valves and on the septum between the valves. The fuel film thickness in the $C_6H_{14}$ simulations appears to be on the order of 10 micron or less.

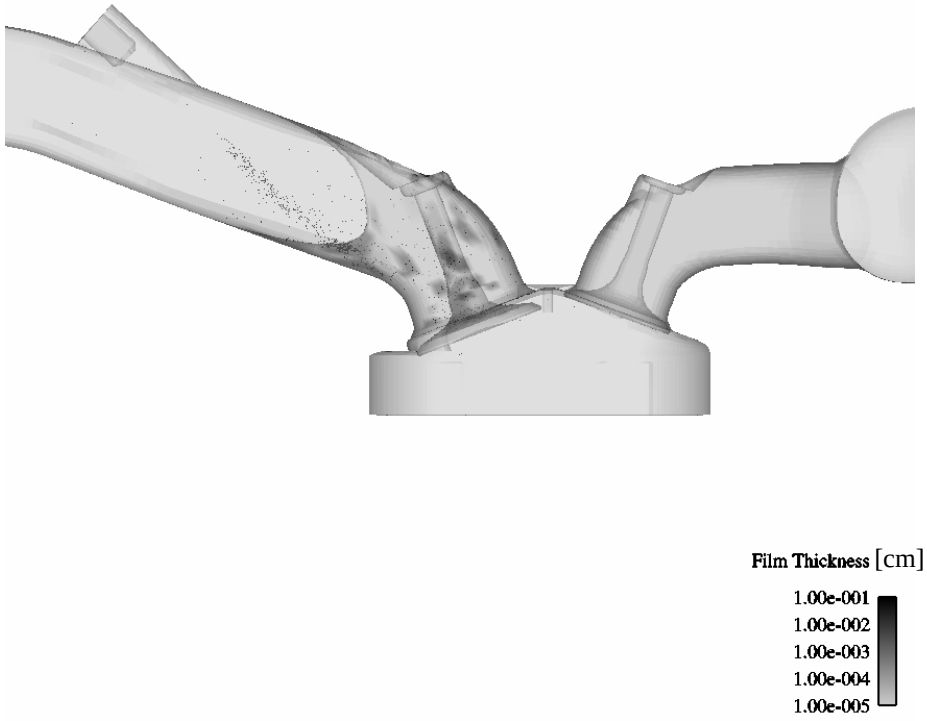


*Figure 22: ERC1 $C_6H_{14}$ Fuel Film Side View at 1070 Crank Angles*

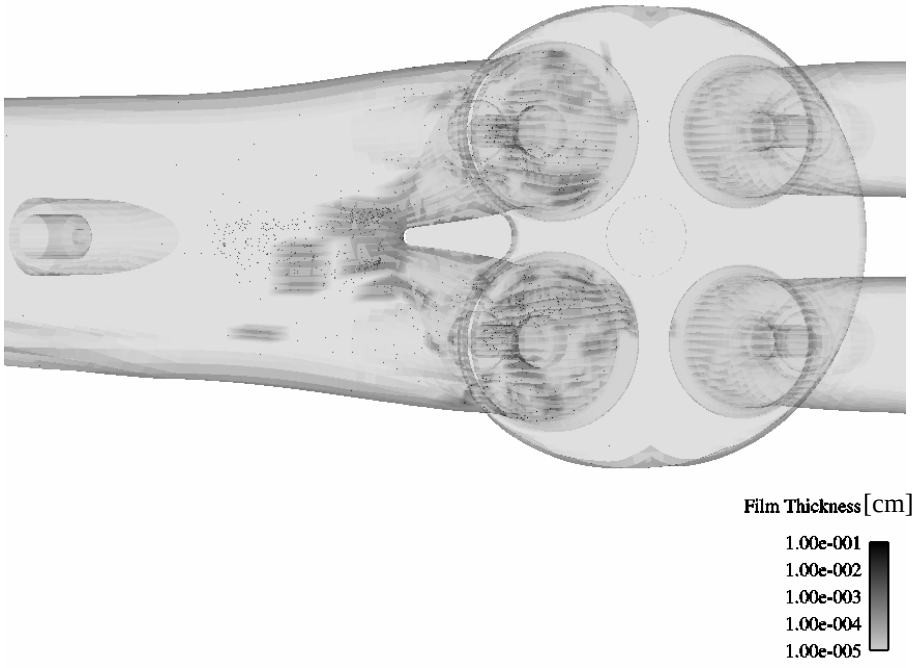


*Figure 23: ERC1 $C_6H_{14}$ Fuel Film Top View at 1070 Crank Angles*

The $C_8H_{18}$ simulation, Figure 24 and Figure 25, shows a fuel films spread throughout the intake manifold. There does appear to be some fuel impingement on the head around the area of the intake valves. The fuel film thickness appears to be on the order of 100 microns or less. The thickest fuel film is occurring on top of the valves and on the septum.

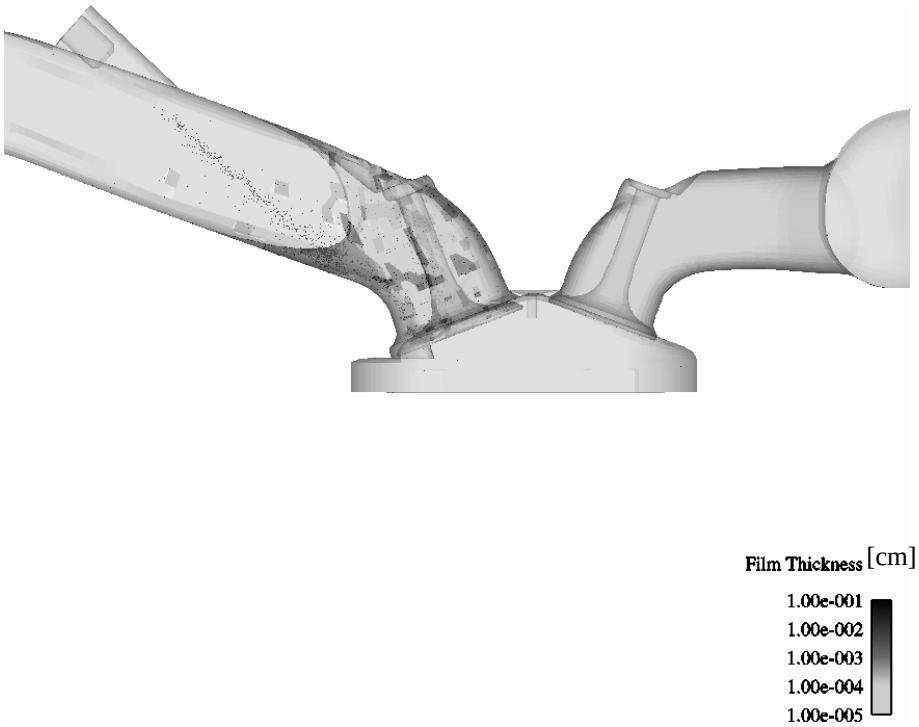


*Figure 24: ERC1 $C_8H_{18}$ Fuel Film Side View at 1465 Crank Angles*

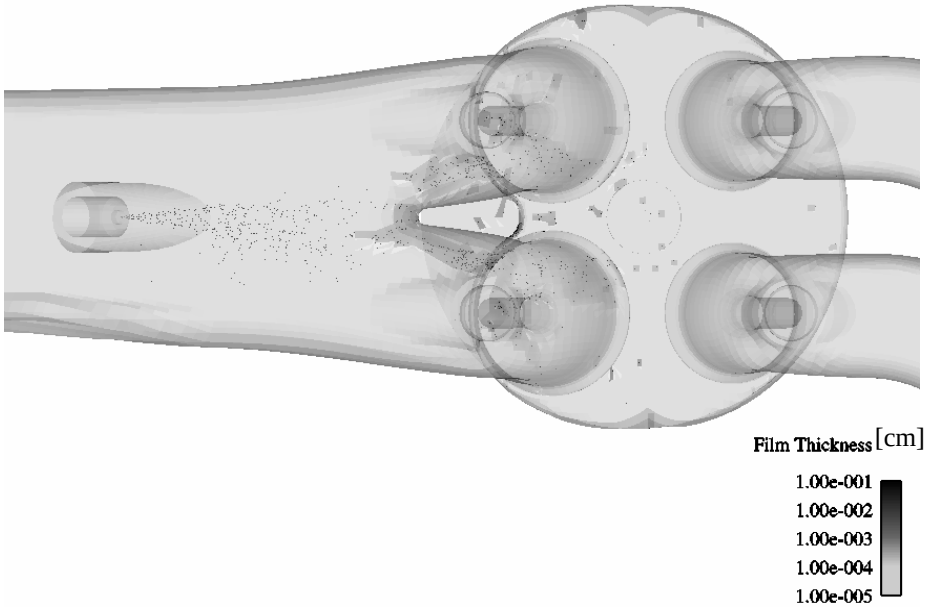


*Figure 25: ERC1 $C_8H_{18}$ Fuel Film Top View at 1465 Crank Angles*

The $C_{14}H_{30}$ simulation, Figure 26 and Figure 27, shows considerable fuel impingement throughout the intake manifold with some fuel films reaching 1000 microns in thickness. Due to the very low level of vaporization in this simulation, there is a film on the entire area around the valves and intake manifold on the order of 100 microns in thickness.

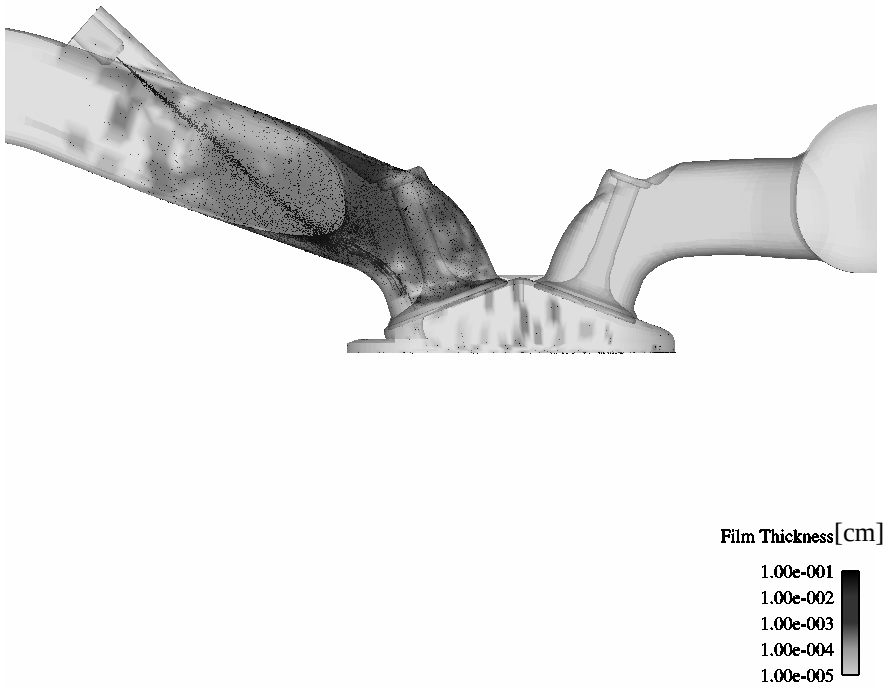


*Figure 26: ERC1 $C_{14}H_{30}$ Fuel Film Side View at 1470 Crank Angles*

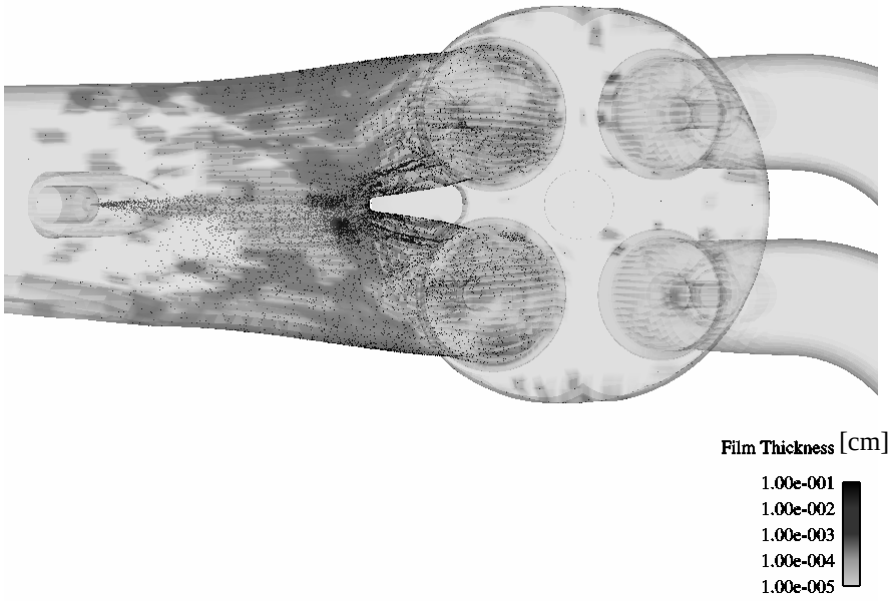


*Figure 27: ERC1 $C_{14}H_{30}$ Fuel Film Top View at 1470 Crank Angles*

## *4.5 Wall-film movement*

The ERC1 $C_8H_{18}$ simulation was chosen to show the transient nature of the film during the simulation. The film in the intake manifold migrates towards the valves and into the cylinder during the intake strokes. Figure 28 shows the buildup of fuel film on the septum and its movement towards the valves. The migration of the fuel film can be seen during the intake, image times 735° thru 900°. The migration of the fuel towards the valve shows some of the fuel entering the cylinder around the valves and staying on the surface of the head after the intake valves close.

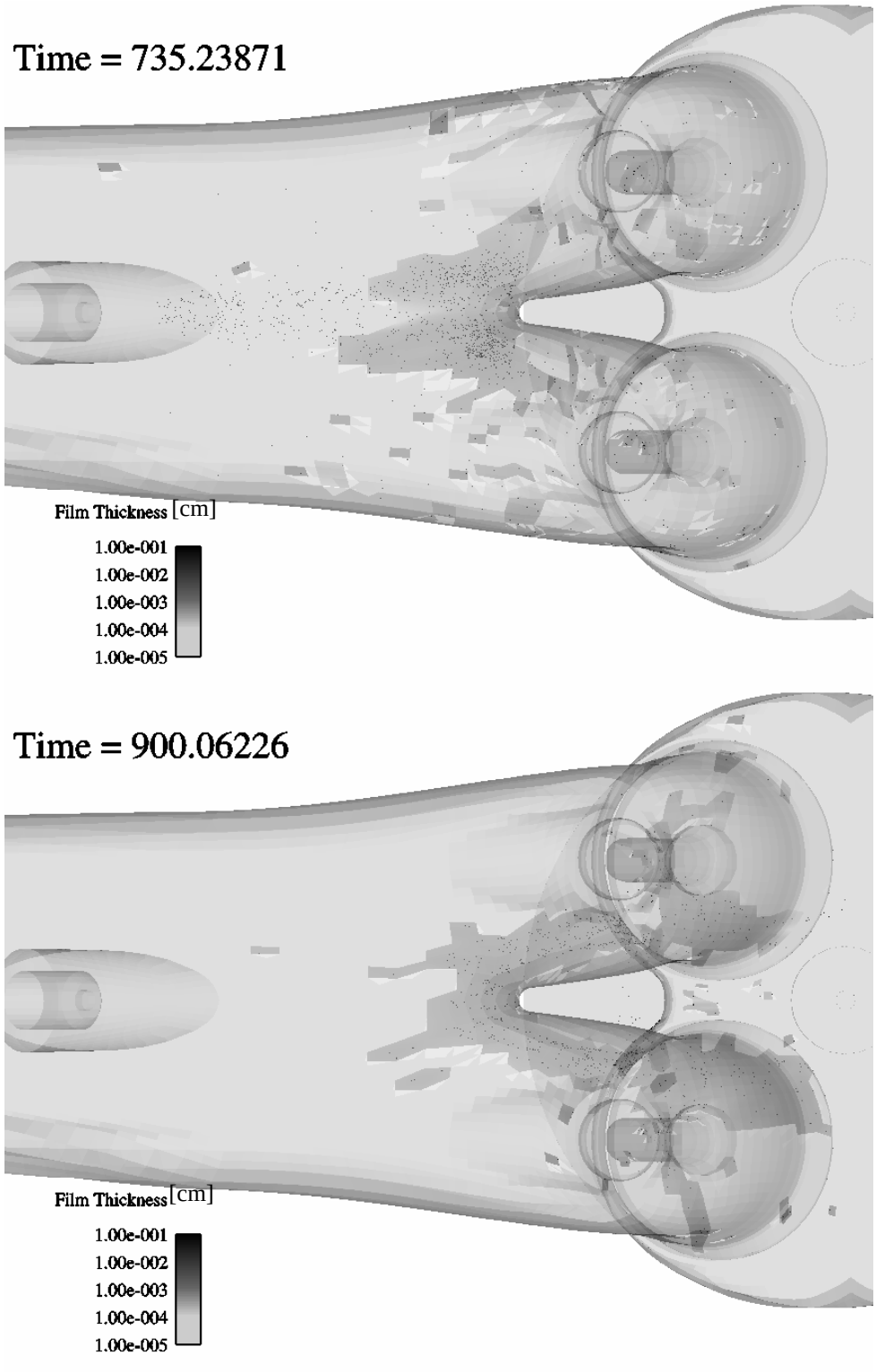


*Figure 28: Migration of $C_8H_{18}$ Fuel Film*

During the second injection, Figure 28 shows fuel adding to existing wall film on the septum and valves tops. This additional fuel buildup would be expected to add to the amount of fuel that is migrating towards the valves and result in more fuel impingement on the head of the cylinder.

The multi-component effects of gasoline are significant based on comparison of the 3 single-component fuel results. Although the wall temperatures, intake temperature and intake pressure vary in the KIVA3v Release 2 simulations due to additional information from Mercury Marine, the results of the KIVA3v simulations clearly show that the multi-component effects are significant. For light components, steady state is approached after 2 cycles. The liquid film is expected to be dominated by the heavy fuel components.

## *4.6 Results of KIVA3v Release 2 Single-component Fuels*

KIVA3v Release 2 was modified to include the rezoning subroutine developed using KIVA3v and single-component simulations were conducted. The single-component fuel tested was single-component gasoline. Single-component gasoline is a fuel mixture considered to be a single species that most closely matches the vaporization characteristics of gasoline but does not account for multi-component effects. The chemical makeup of single-component gasoline is given as $C_8H_{17}$. Figure 29 shows the liquid fuel, vapor fuel and injected fuel during the simulation. The simulation duration included 3 full injections. Figure 29 shows a decreasing

contribution to the liquid fuel in the grid after the second injection. The simulation does appear to reach a near-steady state condition of liquid fuel in the grid.

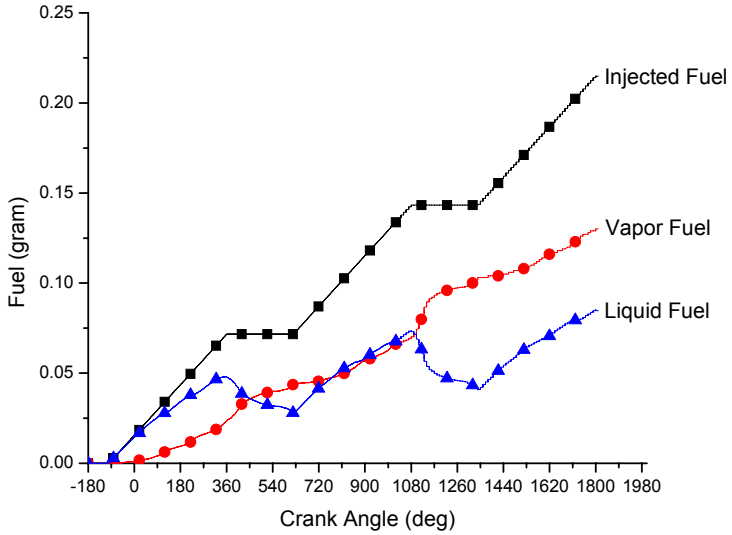


*Figure 29: Single-component Gasoline Liquid in Grid*

Figure 30 shows the decreasing contribution to intake wall film during the second and third injection. The intake appears to have a steady state fuel film of approximately 50mg while the head and liner appear to have steady state fuel films of ~9mg and ~5mg respectively. Some film does appear to reaching the piston and evaporating during each cycle.

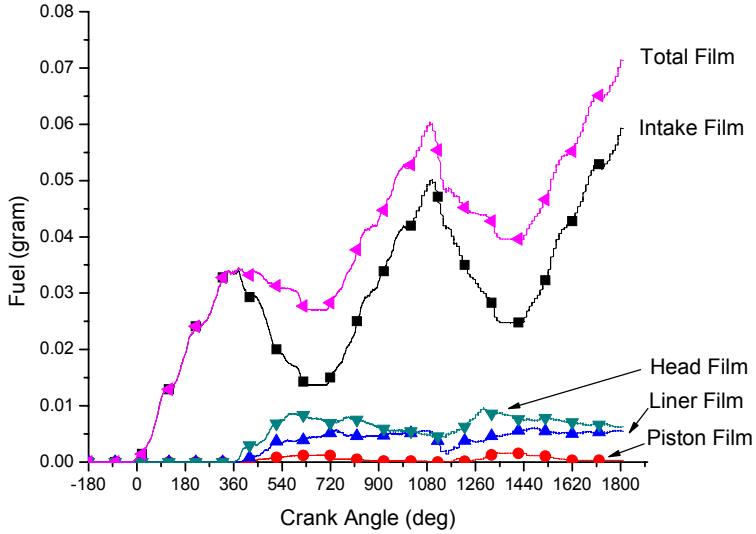


*Figure 30: Single-component Gasoline Fuel Film Results*

Figure 31 shows the amount of fuel film on top of the intake valves. The sharp declines are due to a computational issue when the valves are moving downward. The second and third injections appear to have declining contributions to the film on the intake valves and the steady state valve film appears to be approximately 35mg.

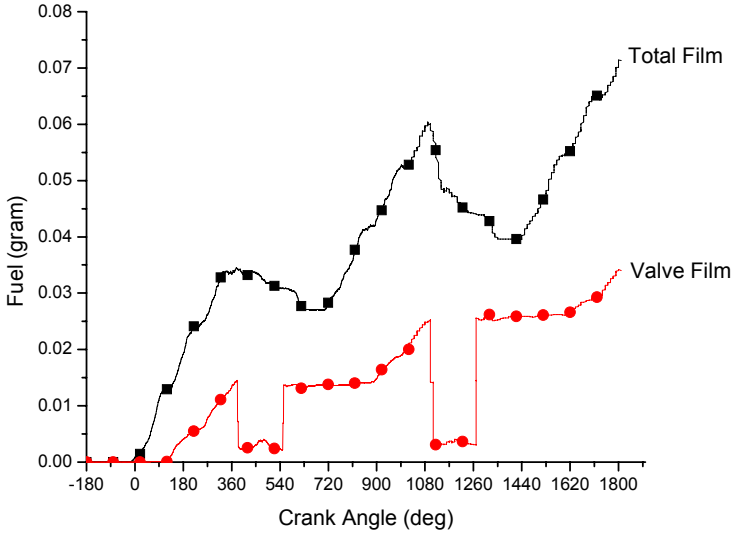


*Figure 31: Single-component Gasoline Valve Film Results*

# 5 MULTI-COMPONENT RESULTS

## 5.1 Overview of Multi-component Model

The multi-component study was conducted with KIVA3v Release 2. This version of KIVA has multi-component capabilities and has been modified to include the rezoning subroutine discussed in Appendix A. Fuel distributions were created based on ASTM D-86 test results, Figure 32, supplied by Mercury Marine. The ASTM D-86 test results were fit to the distribution using a similar method to that of Cotterman et al. [12]. Five test fuels were simulated, 2 summer gasoline blends, 2 winter gasoline blends and Haltermann HE.

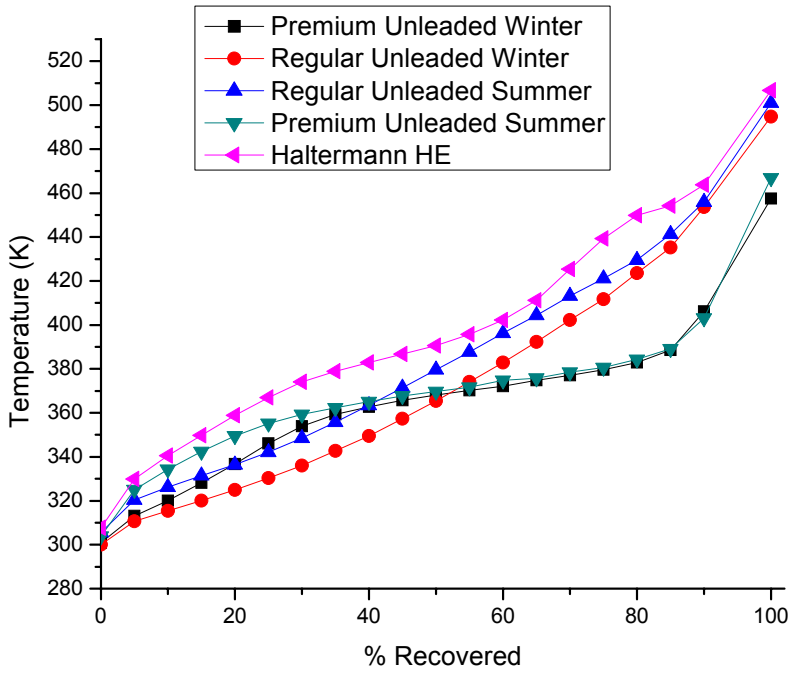


*Figure 32: ASTM D-86 Test Results*

The multi-component fuel distributions are shown in Figure 33. The gasoline distribution determined by [33] is noticeably lighter than the multi-component fuel distributions based on the Mercury Marine test fuels. Table 6 shows a summary of the calculated distributions. For additional information refer to Appendix C.

*Table 6: Summary of Gasoline Distributions*

| | Gasoline | Summer Regular | Summer Premium | Winter Regular | Winter Premium | Haltermann HE |
|---|---|---|---|---|---|---|
| Mean Molecular Weight (g/mol) (mass basis) | 100.5 | 105.5 | 91.54 | 105.5 | 101.1 | 134.5 |
| Mean Molecular Weight (g/mol) (mole basis) | 85.5 | 96.6 | 85.87 | 96.5 | 93.7 | 123.5 |
| Variance | 35.8 | 29.44 | 22.18 | 29.77 | 26.2 | 35.09 |

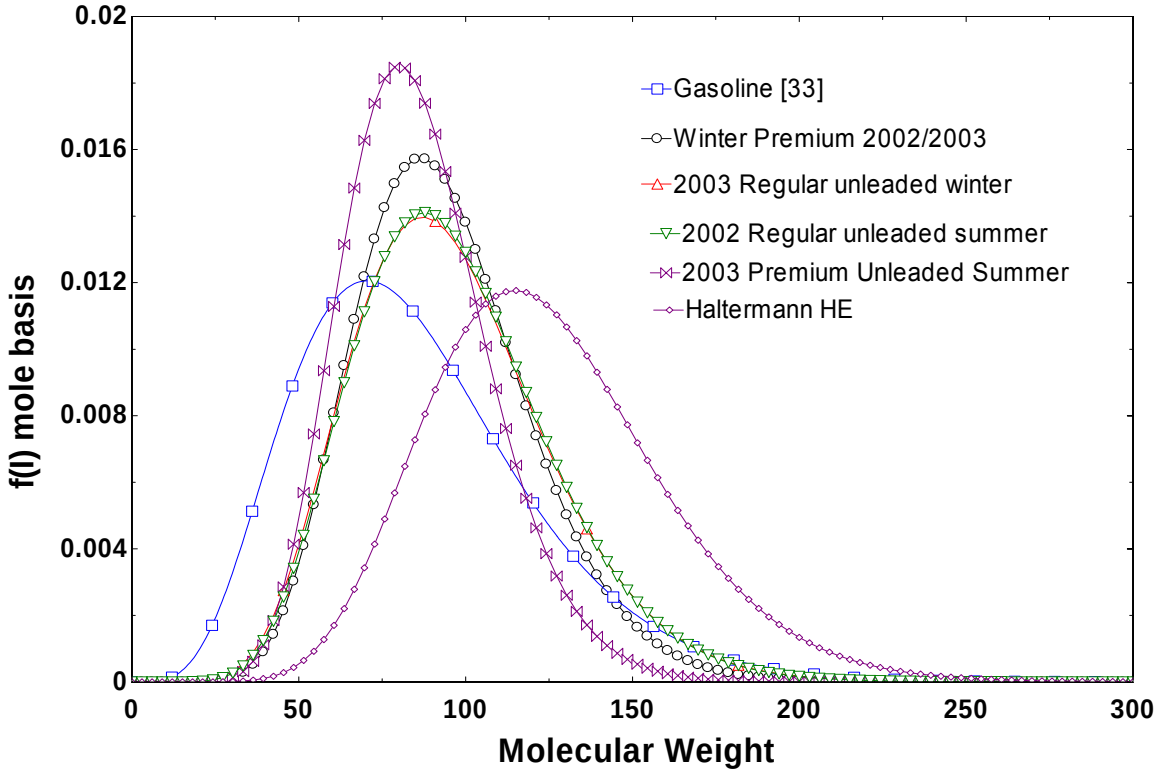


*Figure 33: Multi-component Fuel Distributions*

## 5.2 Results of Multi-component Model

The multi-component simulations were not able to have as long of simulation durations as the single-component simulations. All of the multi-component simulations encountered temperature iteration problems before the end of injection due to large wall film thicknesses in small cells.

## 5.3 Comparison of Multi-component and Single-component Gasoline

The results of the multi-component gasoline simulations were used to investigate the composition of the fuel droplets in the air and those fuel droplets that had impinged. The droplet's composition was averaged on a mass basis to determine the mean composition of both the impinged fuel and air droplets. The mean molecular weight on a mass basis was determined by:

$$\bar{\theta} = \frac{\sum_{n=1}^{np} \bar{\theta}_n V_n \rho_n}{\sum_{n=1}^{np} V_n \rho_n} \quad \text{Equation 15}$$

where $V_n$ and $\rho_n$ refer to the volume and density of the droplet. $\bar{\theta}_n$ refers to the mean molecular weight of an individual parcel and $\bar{\theta}$ refers to the mean molecular weight of the droplets based on mass. Histograms were also created of fuel parcel's mean molecular weight.

### 5.3.1 Results of Gasoline Distributions

The Summer Premium Gasoline distribution simulation results, Figure 34, shows that very little of the injected fuel has vaporized and Figure 35 shows that all of the film is occurring in the intake manifold.

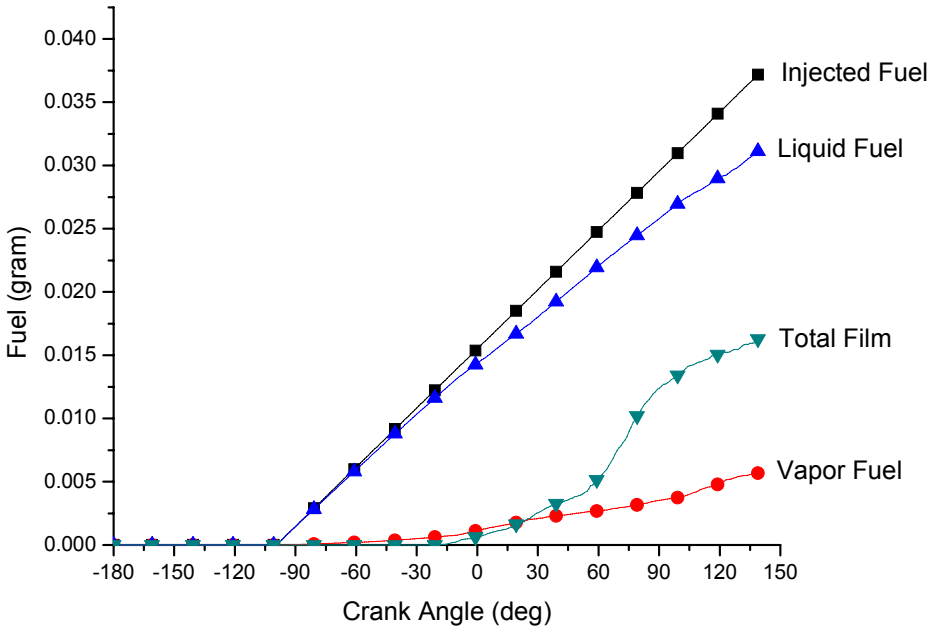


*Figure 34: Summer Premium Fuel in Grid Results*

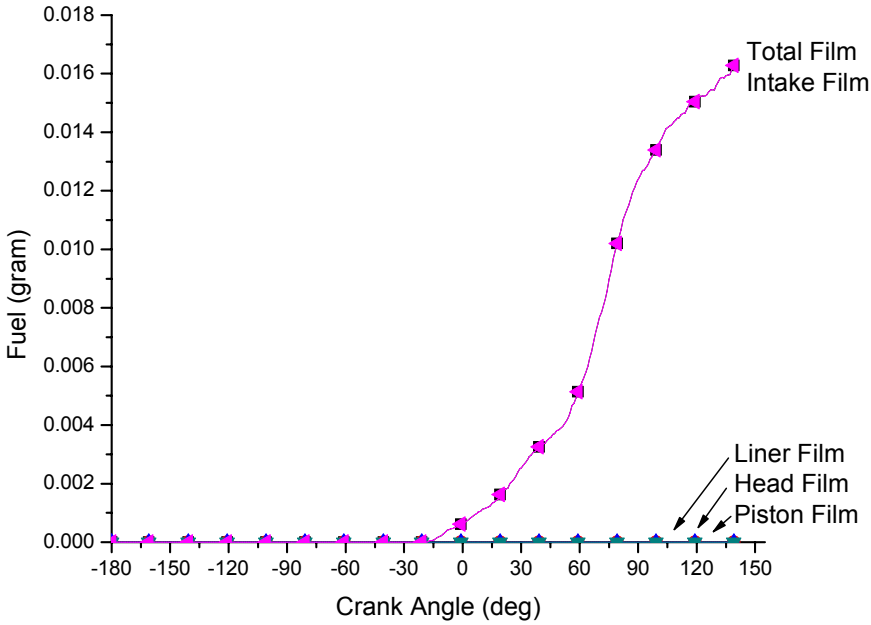


*Figure 35: Summer Premium Fuel Film Results*

All of the winter and summer gasoline distributions had qualitatively and very nearly quantitatively similar results to Figure 34 and Figure 35. Table 7 summarizes the results of summer and winter gasoline distributions obtained at 120°ATDC.

*Table 7: Fuel in Grid Results for Summer and Winter Gasoline at 120°ATDC*

| At 120° ATDC | Summer Regular | Summer Premium | Winter Regular | Winter Premium |
|---|---|---|---|---|
| Injected [mg] | 0.3422 | 0.3422 | 0.3422 | 0.3422 |
| Liquid [mg] | 0.3015 | 0.0291 | 0.3032 | 0.3058 |
| Vapor [mg] | 0.0037 | 0.0048 | 0.0036 | 0.0033 |
| Film [mg] | 0.0151 | 0.0151 | 0.0159 | 0.0162 |

The differences in the fuels can be noticed in the gasoline's changing composition during the simulation. Figure 36 shows the changing composition for

the winter and summer gasoline distributions during the simulation. Table 8 summarizes the mean molecular weight of the fuel at 120°ATDC.

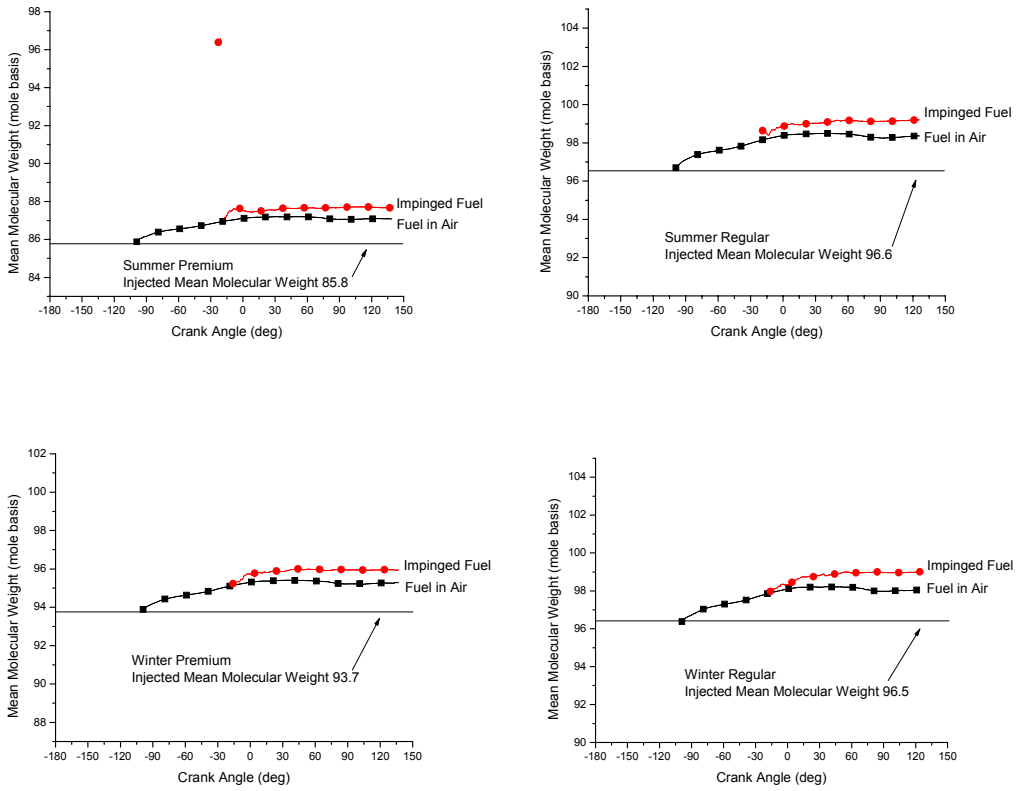


*Figure 36: Gasoline Mean Molecular Weight of Air Droplets and Film Droplets*

*Table 8: Gasoline Mean Molecular Weight of Droplets at 120°ATDC*

| At 120°ATDC<br>Mole Basis | Summer<br>Regular | Summer<br>Premium | Winter<br>Regular | Winter<br>Premium |
|---|---|---|---|---|
| Injected Mean Molecular Mass [g/mol] | 96.6 | 85.8 | 96.5 | 93.7 |
| Air Droplets Mean Molecular Mass [g/mol] | 98.3 | 87.0 | 98.0 | 95.2 |
| Film Droplets Mean Molecular Mass [g/mol] | 99.1 | 87.7 | 98.9 | 95.9 |

Although the change in the mean molecular weight of the droplets appears to be small, Figure 37 shows histograms of the fuel droplets mean molecular weight at 120°ATDC. Even though the mean molecular weight of the fuel has not change significantly, there are a number of fuel parcels have much higher mean molecular weights.

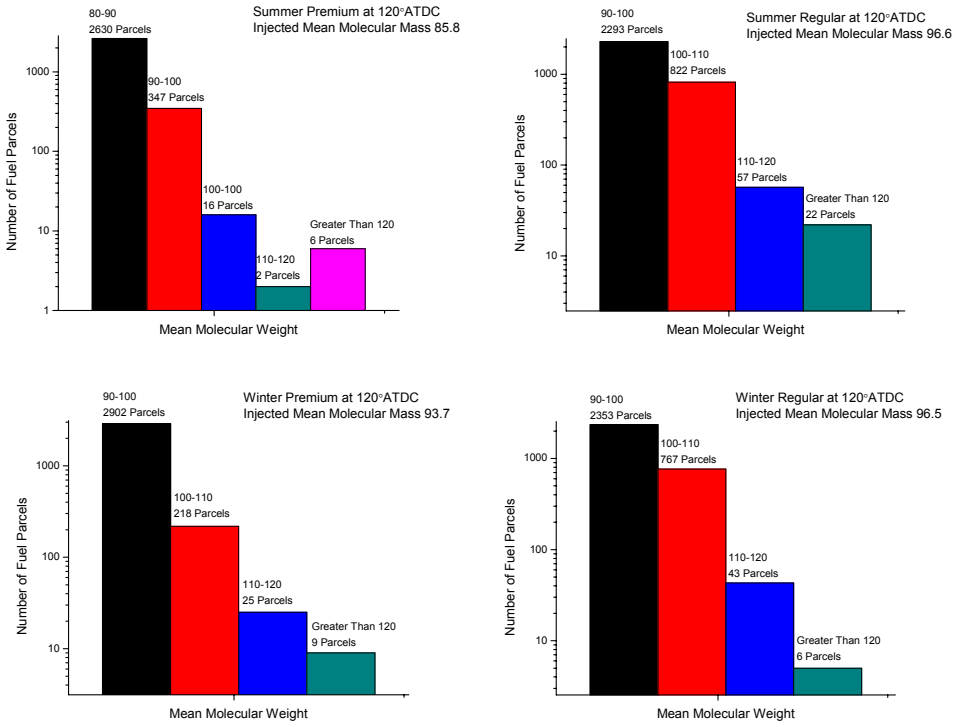


*Figure 37: Gasoline Fuel Parcel Histogram at 120°ATDC*

### *5.3.2 Results of Halterman HE*

The Halterman HE distribution, Figure 38, shows that very little of the injected fuel has vaporized and all of the film is occurring in the intake manifold. Figure 39 shows a slight difference between the mean molecular weight of the fuel droplets in the air versus those impinged. The impinged fuel does have a higher mean

molecular weight than that fuel that has not yet impinged. Both the dispersed phase fuel and fuel that has impinged have mean molecular weights approximately 2g/mol greater than when the fuel was initially injected.

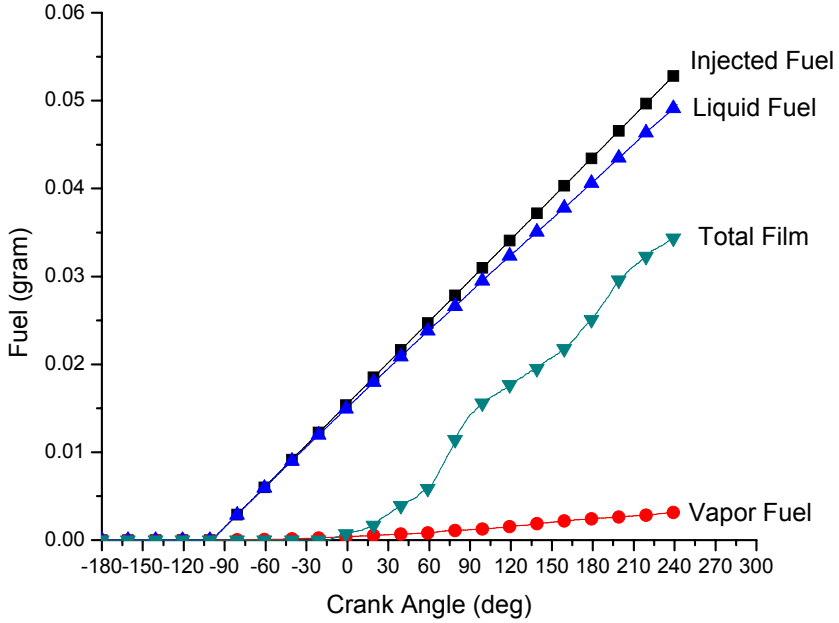


*Figure 38: Haltermann HE Fuel in Grid Results*

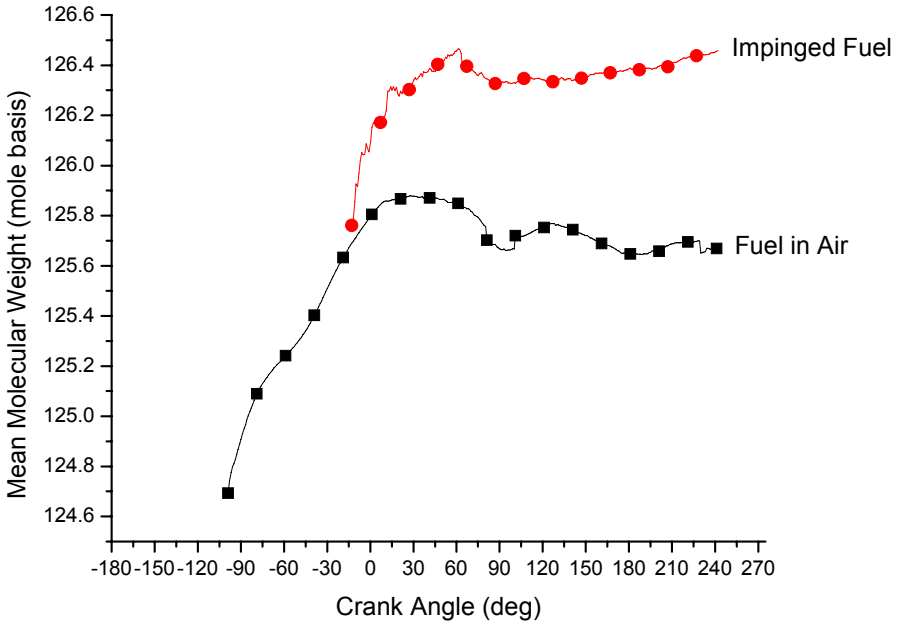


*Figure 39: Haltermann HE Air Droplets versus Impinged Droplets*

## *5.4 Single-component Fuel Concentration*

The multi-component simulations provided insight into how the mean molecular weight of the fuel increases during the simulation but the information attained was limited due to the simulations encountering temperature iteration issues due to large wall film thicknesses in small cells. Single-component simulations were conducted using 25% of the injected fuel mass using $C_9H_{20}$ and $C_{10}H_{22}$ to directly study the heavy end of the distribution, i.e. that part having molecular weight greater than $C_8H_{18}$. The $C_{14}H_{30}$ simulations in Chapter 4 studied the fuel impingement of a heavy fuel, but it was felt that $C_{14}H_{30}$ represents approximately 2 % of the total injection mass and is not representative of fuels with weights in between $C_8H_{18}$ and $C_{14}H_{30}$.

The results of the $C_9H_{20}$ simulations show approximately 30mg of film out of 34mg injected at the end of 2 injections. Figure 40 shows that very little of the $C_9H_{20}$ vaporizes. Figure 41 and Figure 42 show the location and amounts of fuel film during the simulation. Although a majority of the film occurs in the intake manifold, the 0.03mg of fuel that is on the liner is of concern because that is where the fuel would be migrating though the ring pack and into the engine oil. Figure 43 shows that a ~5mg of fuel is on the intake valves during steady state.

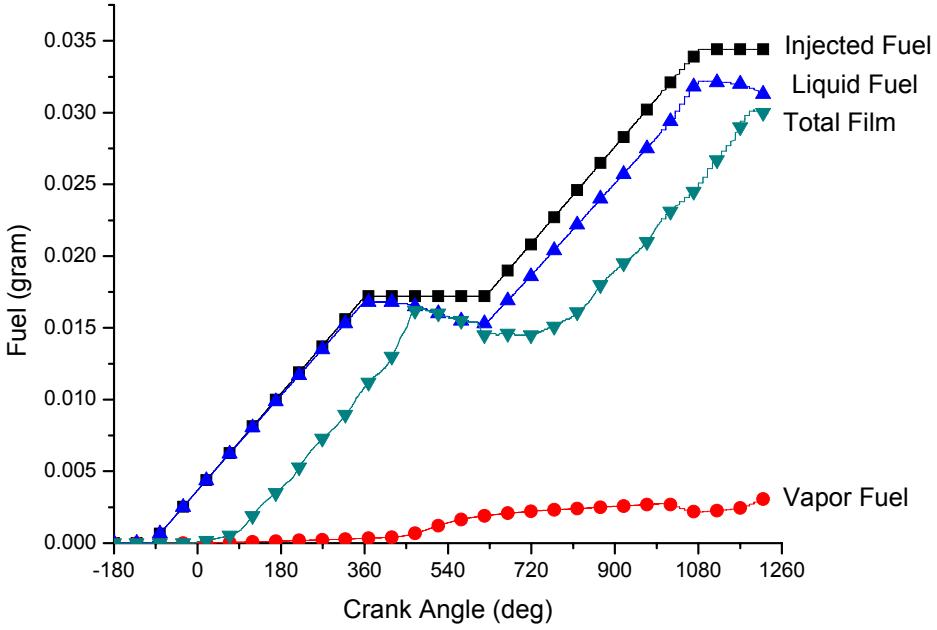


*Figure 40: $C_9H_{20}$ Fuel in Grid*

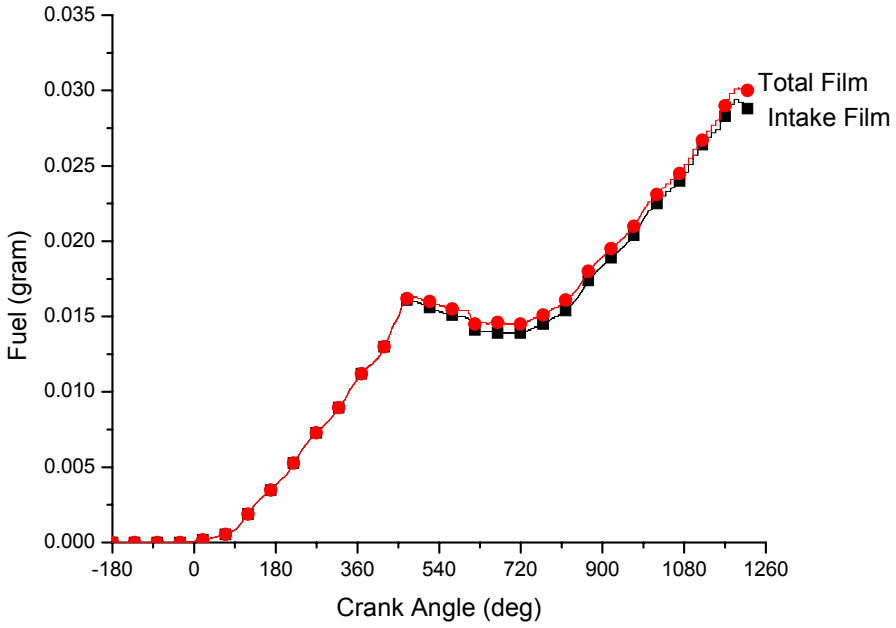


*Figure 41: $C_9H_{20}$ Fuel Film on Intake*

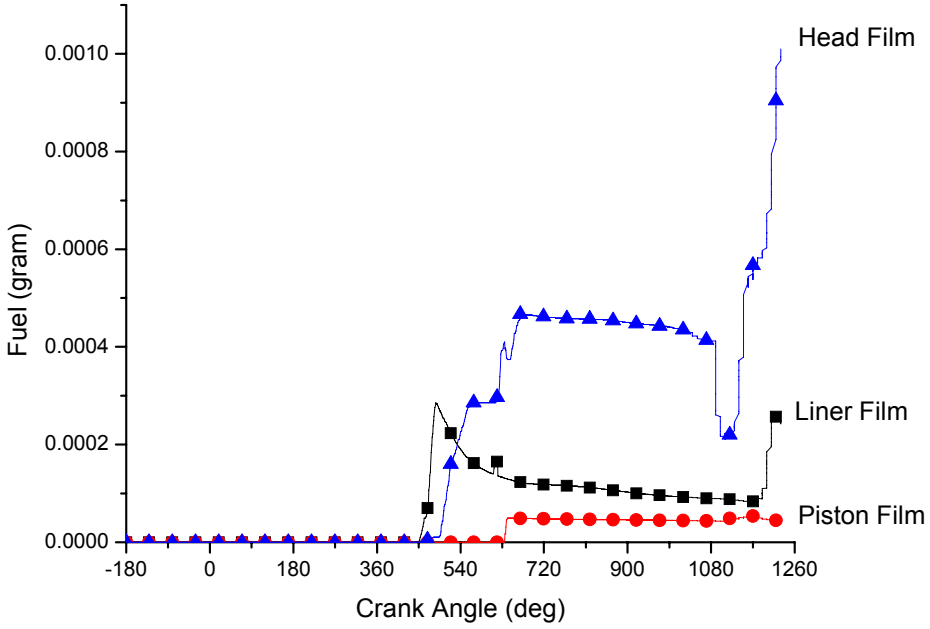


*Figure 42: $C_9H_{20}$ In-cylinder Fuel Film*

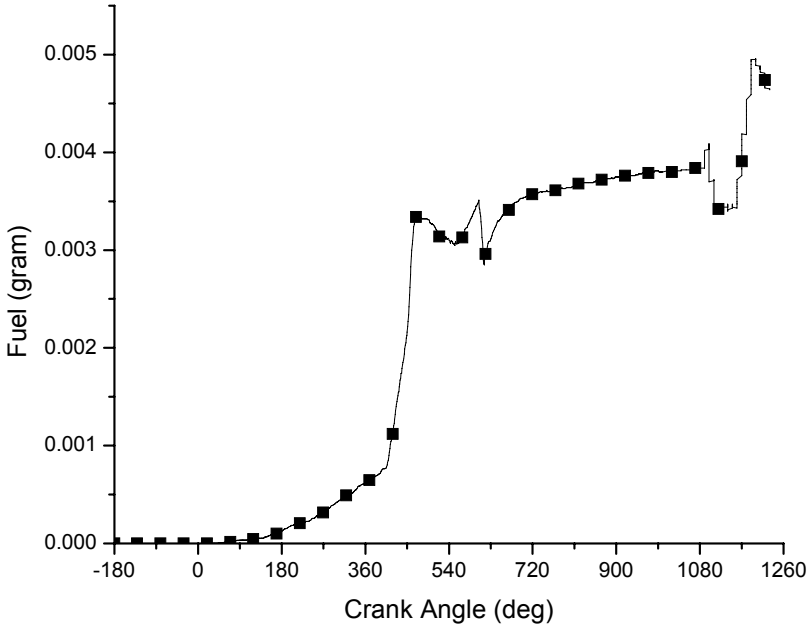


*Figure 43: $C_9H_{20}$ Fuel Film on Intake Valves*

The results of the $C_{10}H_{22}$ simulations show approximately 32mg of film at the end of 2 injections. Figure 44 shows that very little of the $C_{10}H_{22}$ vaporizes. Figure 45 and Figure 46 show the location and amounts of fuel film during the simulation. Although a majority of the film occurs in the intake manifold, 0.06mg of fuel is on the liner and is of concern because that is where the fuel would be migrating though the ring pack and into the engine oil. Figure 43 shows that a ~6mg of fuel is on the intake valves during steady state.

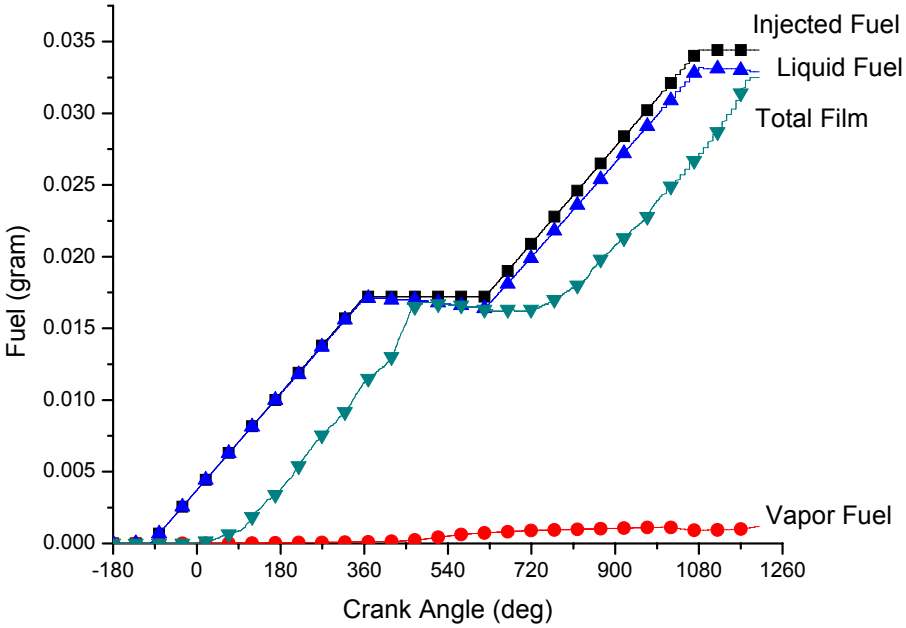


*Figure 44: $C_{10}H_{22}$ Fuel in Grid*

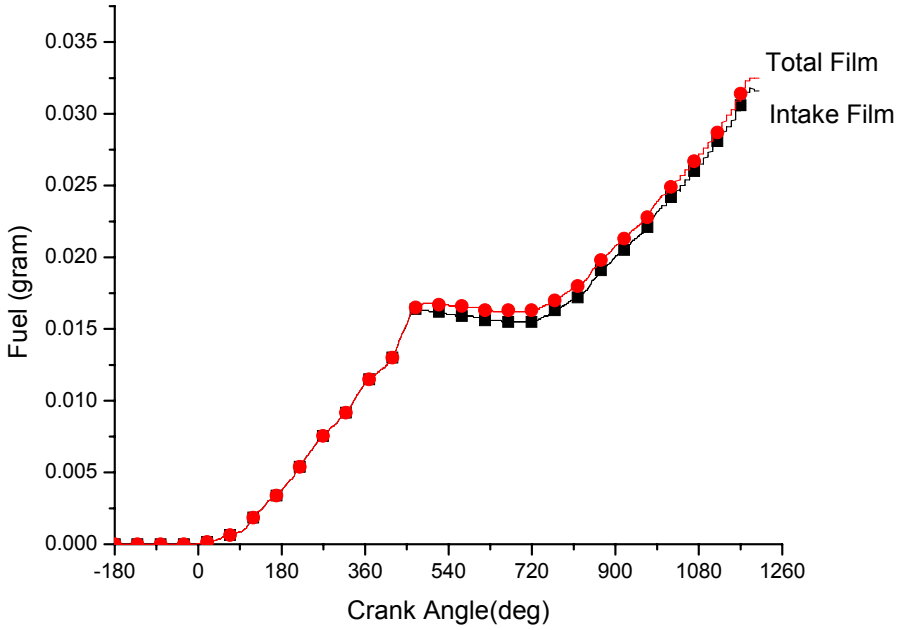


*Figure 45: $C_{10}H_{22}$ Intake Fuel Film*

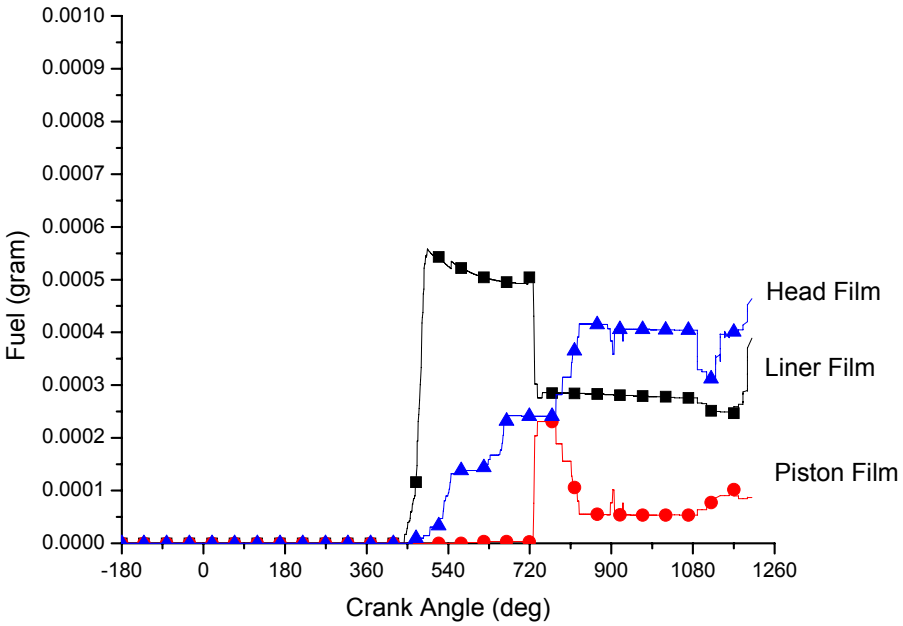


*Figure 46: $C_{10}H_{22}$ In-cylinder Fuel Film*

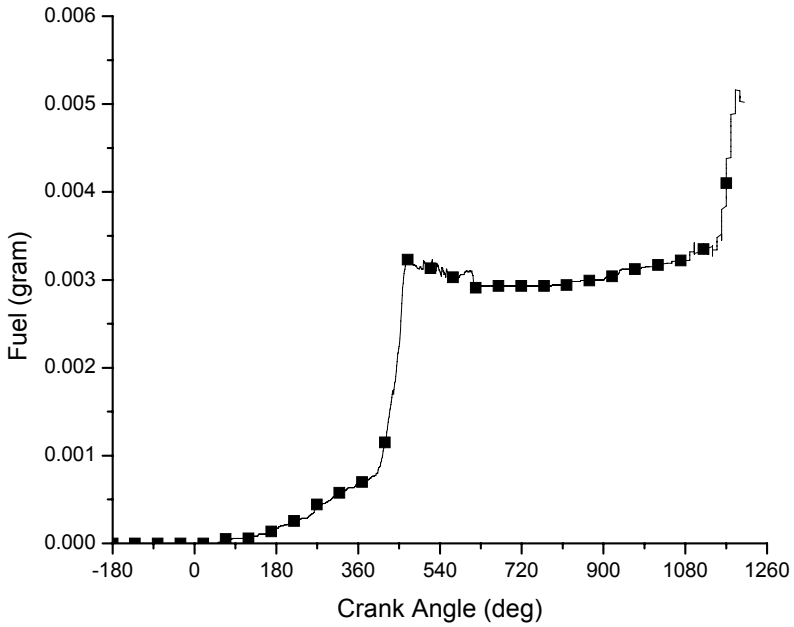


*Figure 47: $C_{10}H_{22}$ Fuel Film on Intake Valves*

# 6 SUMMARY AND RECOMMENDATIONS

## *6.1 Summary of Study*

A computational study of fuel impingement in a port fuel injection gasoline engine was performed. An understanding of the fuel impingement location and mass provides insight into the fuel delivery process at high load where oil dilution can be a significant problem. This process is inherently difficult to study experimentally due to the high engine speeds and loads. The relatively low intake manifold temperatures and large amount of fuel injected make fuel impingement of particular interest in marine outboard engines. This study included the development of a rezoning subroutine, a single-component fuel study and a multi-component fuel study.

Single-component fuel simulations provided insight into the extent to which multi-component would be important and gave an initial indication of the amount and location of fuel impingement. The single-component study showed significant differences between $C_6H_{14}$, $C_8H_{18}$ and $C_{14}H_{30}$ fuels. Ideally a steady-state amount of fuel impingement would have been reached to fully understand the location and amounts of fuel impingement. The low intake manifold temperatures resulted in only $C_6H_{14}$ reaching a steady-state condition; $C_8H_{18}$ was nearing a steady-state condition and $C_{14}H_{30}$ liquid was continually building up in the intake manifold at the end of the simulation. These results indicated a fuel-composition dependence of the fuel impingement process. Single-component gasoline ($C_8H_{17}$) was also simulated. The single-component gasoline showed fuel building in the intake manifold and migrating

towards the valve and onto the cylinder head and liner during intake events. A steady-state amount of fuel impingement on the head and liner was estimated to be 3.5% and 0.5% of injected fuel respectively.

The multi-component study used the Continuous Thermodynamics Method [22] to allow for fuel distributions instead of a fuel with a single chemical makeup and properties. The fuel distributions were created based on a curve fit between molecular weight and boiling temperature of multiple species and the results of ASTM D-86 tests provided by Mercury Marine[12][24] for several fuel blends. The calculated fuel distributions were heavier than the fuel distribution of Tamim and Hallet, 1995[33].

The results of the multi-component study showed that the mass-averaged mean molecular weight of the fuel droplets in the film was heavier than those droplets still in the air. This would suggest that the film composition has shifted towards the heavier end of the original distribution, and some of the lighter components have vaporized. Histograms of the fuel parcel's mean molecular mass also showed a trend towards larger numbers of heavier fuel parcels but the mass of those parcels were not significant enough to influence the mass-averaged mean molecular weight.

Ideally the multi-component simulations would have successfully completed 1 full cycle but the large amount of fuel impingement resulted in temperature iteration problems due to large wall film thickness in small cells approximately 220° after the

start of the injection. If the simulation had successfully completed one cycle, one could expect that the mean molecular weight of the fuel would continue to increase.

The results of the $C_9H_{20}$ and $C_{10}H_{22}$ simulations showed a significant change in the fuel impingement process when compared to $C_8H_{18}$ and single-component gasoline. The $C_9H_{20}$ and $C_{10}H_{22}$ simulations resulted in the fuel film making of 86.9% and 94.4% of total injected fuel respectively compared to 38.6% for $C_8H_{18}$ and 33.2% for single-component gasoline. At the given conditions, there is a clear transition in the impingement process between $C_8H_{18}$ and lighter hydrocarbons, and hydrocarbons that are heavier than $C_8H_{18}$.

## *6.2 Topics for Further Research*

While this study provided insight into the fuel composition dependence of fuel impingement, the limitations on simulation length and wall-film model should be taken into consideration. The limitations on simulation length were mainly due to the simulation encountering temperature iteration issues due to wall film thicknesses at some point during the simulation. The wall-film model provided movement of the droplets on the wall and vaporization of fuel from those droplets, but there is room for improvement. The large amount of fuel impingement in this study would have been expected to create a film or puddle of fuel in the intake manifold. The current wall film model calculates vaporization based on a wall film but the movement and interactions of the fuel is still treated in particle form. The model does account for droplets moving perpendicular to the surface but one could expect large numbers of

these droplets combining into a large surface film and moving as a film instead of as individual particles.

# REFERENCES


1. Abraham J. and Magi V., 1998, “A Model for Multicomponent Droplet Vaporization in Sprays”, SAE Technical Paper 980511.

2. Ambramzon B. and Sirignao W.A., 1989, “Droplet Vaporization Model for Spray Combustion Calculations”, Int. J Heat Mass Transfer, Vol. 32, No. 9. pp. 1605-1618.

3. Aggarwal S.K. and Chitre S., 1991, “Computations of Turbulent Evaporating Sprays”, AIAA J. Propulsion, Vol. 7, pp. 213-220.

4. Aggarwal S.K. and Peng F., 1995, “A Review of Droplet Dynamics and Vaporization Modeling for Engineering Calculations”, Journal of Engineering for Gas Turbines and Power, Vol.117, pp. 453-461.

5. Amsden A.A, 1993, “KIVA-3: A KIVA Program with Block –Structured Mesh for Complex Geometries”, Los Alamos National Labs., LA-12503-MS.

6. Amsden A.A, O’Rourke P.J., and Butler T.D., 1989, “KIVA-II – A Computer Program for Chemically Reactive Flows with Sprays”, Los Alamos National Labs., LA-11560-MS.

7. Amsden A.A, 1999, “KIVA-3V Release 2, improvements to KIVA-3V”, Los Alamos National Labs, LA-UR-99-915.

8. Annamalai K. Ryan W. and Chandra S., 1993 “Evaporation of Multicomponent Drop Arrays”, ASME Journal of Heat Transfer, Vol. 115, pp. 707-716.

9. Ayoub N.S. and Reitz R.D., 1997, “Multidimensional Modeling of Fuel Effects and Split Injections on Diesel Engine Cold Starting”, AIAA Journal of Propulsion and Power, Vol. 13, No. 1, pp. 123-130.

10. Briano J.G. and Glandt E.D., 1983, “Molecular Thermodynamics of Continuous Mixtures”, Fluid Phas Equilibria, Vol. 14, pp. 91-102.

11. Chaves H., Kubitzek A.M. and Obermeier F., 1998, “Dynamical Processes Occuring During the Spreading of Thin Liquid Films Produced by Drop Impact on Hot Walls”, Proceedings of the ILASS-Europe ’98 Conference, Manchester, 6-8 July, 1998.

12. Cotterman R.L., Bender R., and Prausnitz J.M. 1985, “Phase Equilibria for Mixtures Containing Very Many Components: Development and Application of Continuous Thermodynamics for Chemical Process Design”, Ind. Eng. Chem. Process Des. Dev., Vol 23, pp. 194-203.

13. Cotterman R.L. and Prausnitz J.M., 1991, “Continous Thermodynamics for Phase-Equilibrium Calculations in Chemical Process Design”, Kinetic and Thermodynamic Lumping of Multicomponent Mixtures, ed. G. Astarita and S.I. Sandler, Elsevier, pp. 229-275

14. Han Z. and Reitz R.D., 1995, “Turbulence Modeling of Internal Combustion Engines Using RNG k-ε Models”, Combust. Sci. and Tech., Vol. 106, p.267

15. Han Z. and Reitz R.D., 1996, “A Temperature Wall Function Formulation for Variable-Density Turbulence Flows with Application to Engine Convective Heat Transfer Modeling”, Intl. Jnl. Heat Mass Transfer.

16. Heywood J.B., 1988, “Internal Combustion Engine Fundamentals”, McGraw-Hill, New York.

17. Hiroyasu H., Kadota T., Senda T. and Imamoto T., 1974, “Evaporation of a Single Droplet at Elevated Pressure and Temperatures: Experimental Study”, Trans. Japan Soc. Mech. Engrs., Vol. 40, pp.3147-3161.

18. Kehlen H., Rätzsch M.T., and Bergmann J., 1985, “Continuous Thermodynamics of Multicomponent Systems”, AIChE J., Vol 31, No. 7, pp. 1136-1148.

19. Law C. K., 1976, “Multicomponent Droplet Combustion with Rapid Internal Mixing”, Combustion and Flame, Vol. 26, pp. 219-233.

20. Law C.K. and Law H.K., 1982, “A $d^2$-Law for Multi-component Droplet Vaporization and Combustion”, AIAA Journal, Vol. 20, 522-527.

21. Lindgren R. and Denbratt I., 2000, “Modelling Gasoline Spray-wall Interaction – A Review of Current Models”, SAE Technical Paper Series 2000-01-2808.

22. Lippert A.M., 1999, “Modeling of Multicomponent Fuels with Application to Sprays and Simulation of Diesel Engine Cold Start”, Ph.D. Thesis, University of Wisconsin-Madison

23. Meyer R. and Heywood J.B., 1999, “Effect of Engine and Fuel Variables on Liquid Transport into the Cylinder in Port-Injected SI Engines”, SAE Technical Paper 1999-01-0563.

24. Mercury Marine, Private Communications, 2006

25. Naber J.D. and Reitz R.D., 1988, “Modeling Engine Spray/Wall Impingement”, SAE Technical Paper 880107.

26. O’Rourke P.J. and Amsden A.A., 1987, “The TAB Method for Numerical Calculation of Spray Droplet Breakup”, SAE Technical Paper 961961.

27. Reitz, R.D., 1987, “Modeling Atomization Process in High-Pressure Vaporizing Sprays”, Atomization and Spray Technology, Vol. 3,309.

28. Senda, J. and Fujimoto H, 2001, “Multicomponent Fuel Consideration for Spray Evaporation Field and Spray-Wall Interaction”, SAE Technical Paper 2001-01-1071.

29. Skippton S.M. and Norton D., 1998, “The Effects of Gasoline Volatility on Mass and Composition of the Inlet Port Wall Film in Port-Injected SI Engines”, SAE Technical Paper 982517.

30. Stanton D.W., 1995, “Modeling Fuel Film Formation and Wall Interactions in Diesel Engines”, MS Thesis, University of Wisconsin-Madison.

31. Stanton D.W., 1998, “Multi-dimensional Modeling of Fuel Films and Spray-Wall Interactions Resulting from Impinging Sprays”, Ph.D. Thesis, University of Wisconsin-Madison.

32. Stanton D.W., Lippert A.M, Reitz R.D., and Rutland C.J., 1998 “Influence of Spray-Wall Interaction and Fuel Films on Cold Starting in Direct Injection Diesel Engines”, SAE Technical Paper Series, 982584

33. Tamim J. and Hallett W.L.H., 1995, “Continous Thermodynamics Model for Multicomponent Vaporization”, Chem. Engr. Sci., Vol. 50, No.18, 2933-2942.

34. Turns S.R., 2000, “An Introduction to Combustion”, McGraw-Hill, New York.

35. Ra Y. and Reitz R.D., 2003, “The Application of a Multicomponent Droplet Vaporization Model to Gasoline Direct Injection Engines”, Int. J. Engine Res., Vol. 4, No. 3, pp. 193-218.

36. Wang, D. and Lee, C.F., 2005 “Continuous Multicomponent Fuel Film Vaporization Model for Multidimensional Engine Modeling”, SAE Technical Paper 2005-01-0209.

37. Whitson C.H., 1983, “Characterizing Hydrocarbon Plus Fractions”, Soc. Petroleum Engineers Jnl., Vol. 1983, 683-694.

38. Zhu G.S., Reitz R.D., Xin J., and Takabayashi T., 2001, “Characteristics of Vaporizing Continuous Multicomponent Fuel Sprays in a Port Fuel Injection Gasoline Engine”, SAE Technical Paper Series 2001-01-1231.

# Appendix A – Design of Rezoning Subroutine

The rezoning subroutine was based on a generic rezoning subroutine provided by Randy Hessel of the Engine Research Center, which was modified to work with the Mercury Verado grid. This rezoning subroutine moves the computational grid vertices to allow for grid movement and provide good computational cells. The rezoning subroutine will be described in detail.

The rezoning subroutine uses an array variable called `moveme` that is initialized to all grid vertices as 1. This `moveme` variable will be used to limit which vertices are moved in each step, and finally is set to 0 when the vertex will no longer be moved. The figures in this appendix will show what cells have been fixed during the rezoning subroutine and are depicted as GRAY when `moveme` is equal to 0.

The first step in the rezoning subroutine uses a DO statement to look at every vertex in the grid (1-nverts) and uses a series of IF statements such that the only remaining vertices with a `moveme` value of 0 are fluid vertices in the cylinder. The cells outside of the cylinder do not need to be moved because there is no grid movement in any other grid regions. The solid boundaries must be set to `moveme=0` so that the solid shape of the grid remains intact. Figure 48 shows grid after the first step in the rezoning subroutine where `moveme=0` cells are shown in gray.

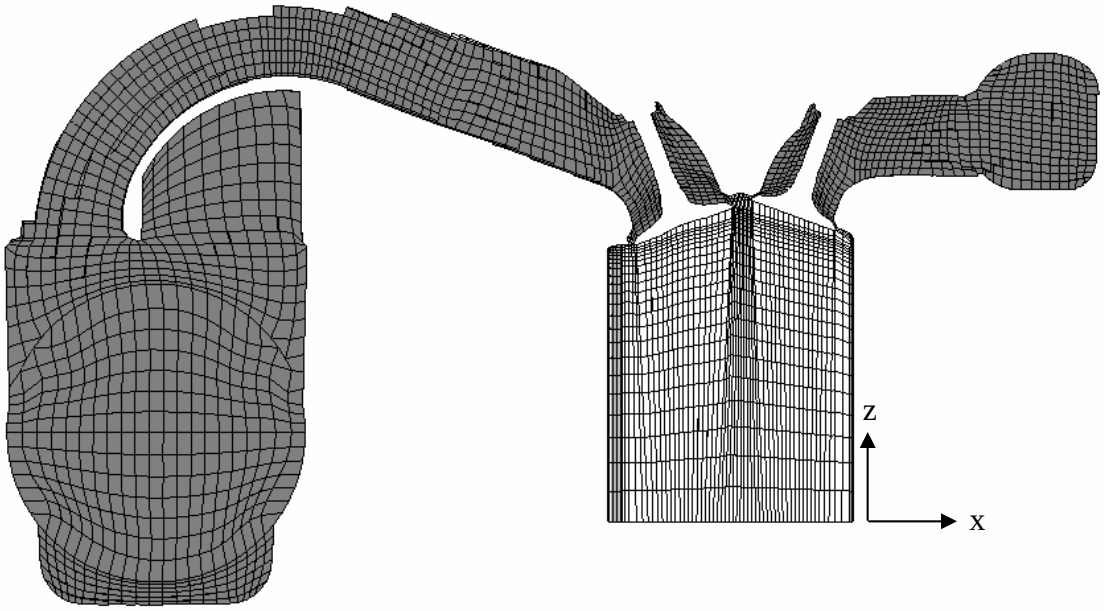


*Figure 48: First Step in Rezoning Subroutine*

The rezoning subroutine then counts the number of grid planes between the bottom of the lowest valve and the piston. Every grid vertex on the bottom of the valves is examined to make sure that the lowest number of planes is calculated. The vertices underneath the valves are then interpolated between the bottom of the valves and the piston. The interpolation is weighted so more vertices are near the top of the valve than are at the bottom of the cylinder. This provides more grid points near the valves which allows for greater flexibility during valve movement. Once a vertex has been interpolated, the `moveme` value of the vertex is set to 0. Lastly any

points above the valve are set to `moveme=0` because moving those points could make it difficult to allow the valves to move up during the cycle. Figure 49 shows grid after the second step in the rezoning subroutine where `moveme=0` cells are shown in gray.

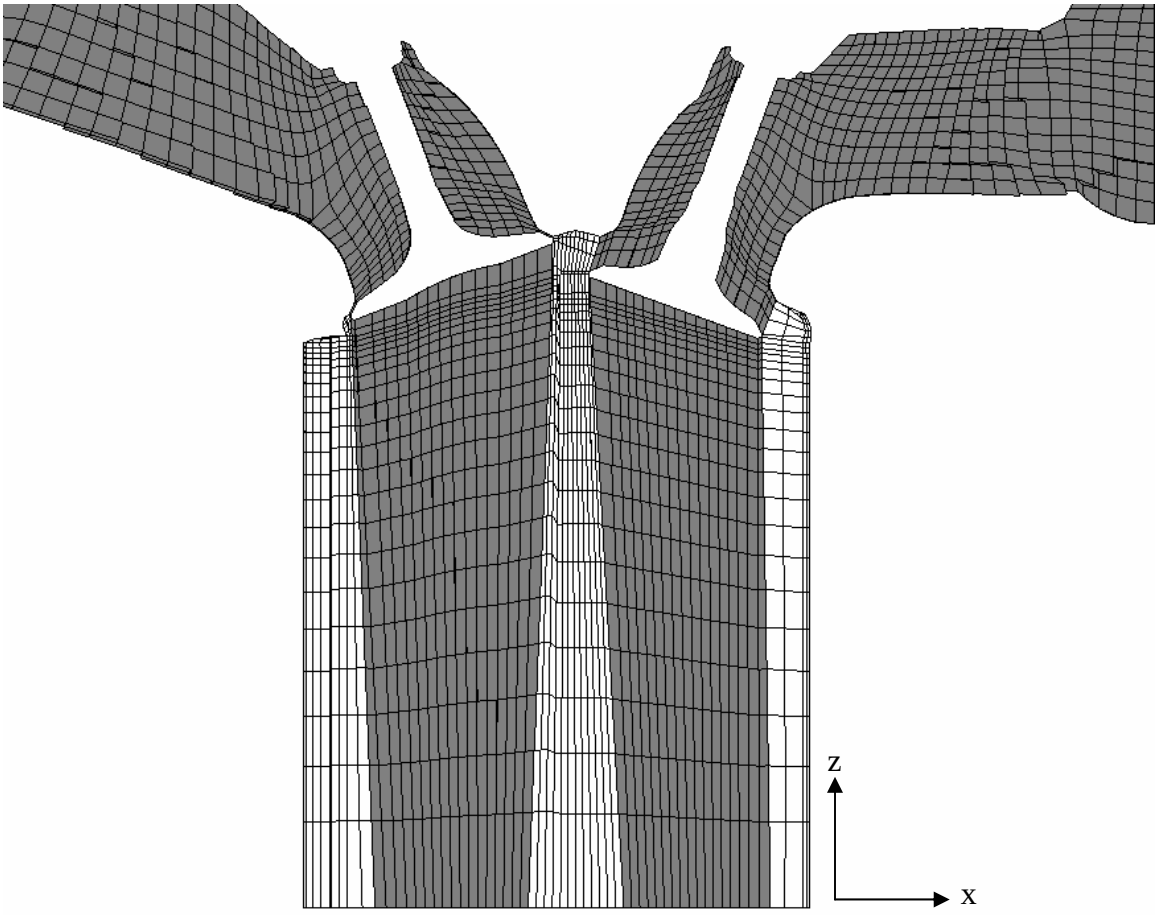


*Figure 49: Second Step in Rezoning Subroutine*

The next step in the subroutine finds the highest plane in the cylinder that falls below the flat part of the head and interpolates any vertices with movevme=1 below that plane using an weighted interpolation that matches the wall vertex spacing. This results in all vertices below the flat part of the head being interpolated and

having very good computational cells. Once a vertex has been interpolated, the vertex `moveme` value is set to 0. Figure 50 shows grid after the third step in the rezoning subroutine where `moveme`=0 cells are shown in gray.

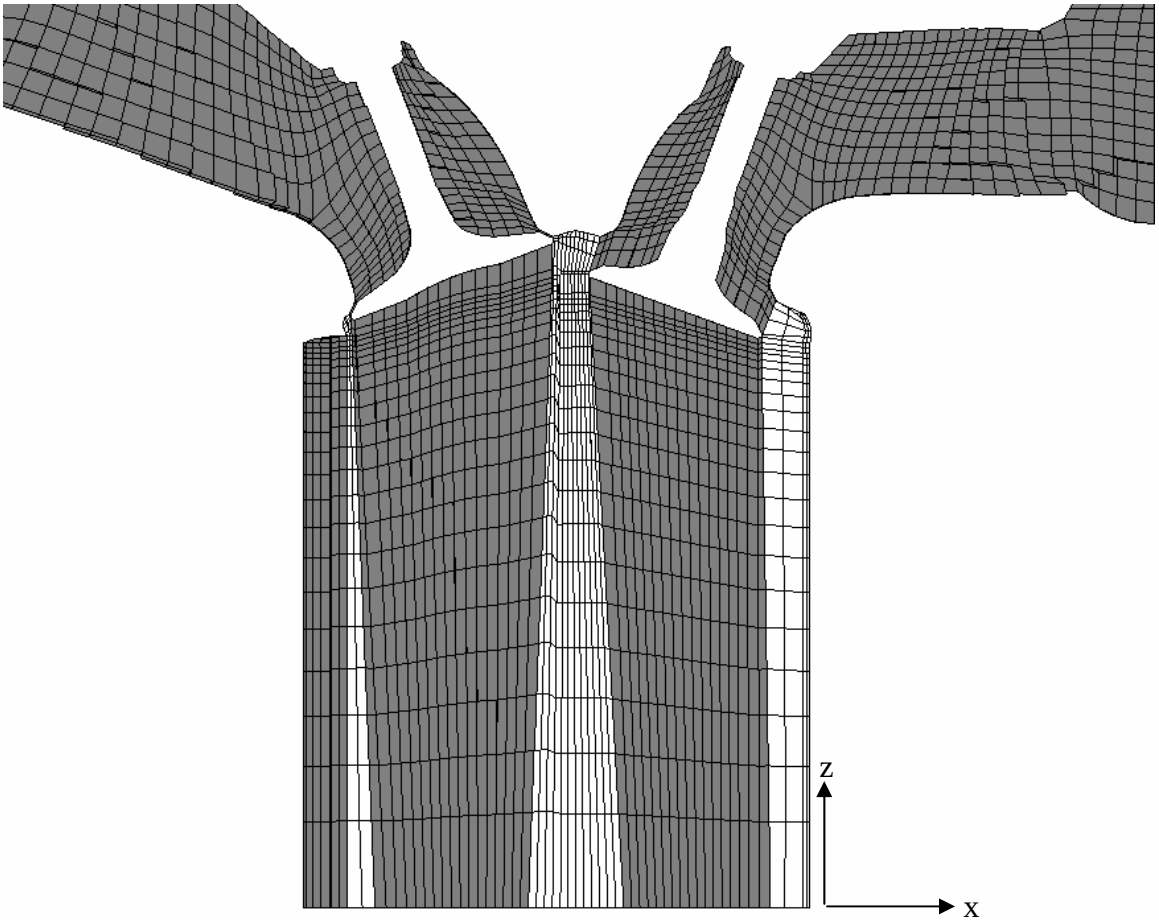


*Figure 50: Third Step in Rezoning Subroutine*

The rezoning subroutine then interpolates between the two valves and between the valves and the side walls. This portion of the code looks at all remaining points with `moveme`=1 and looks in both the *x* and *y* directions to find whether a valve lies in the path. If there is a valve in an *x* or *y* direction, it

interpolates between the valve and the wall or in between the valves which gives good grid structure in the space between the valves and in between the valves and the wall. Once a vertex has been interpolated its `moveme` value is set to 0. Figure 51 shows grid after the fourth step in the rezoning subroutine where `moveme=0` cells are shown in gray.

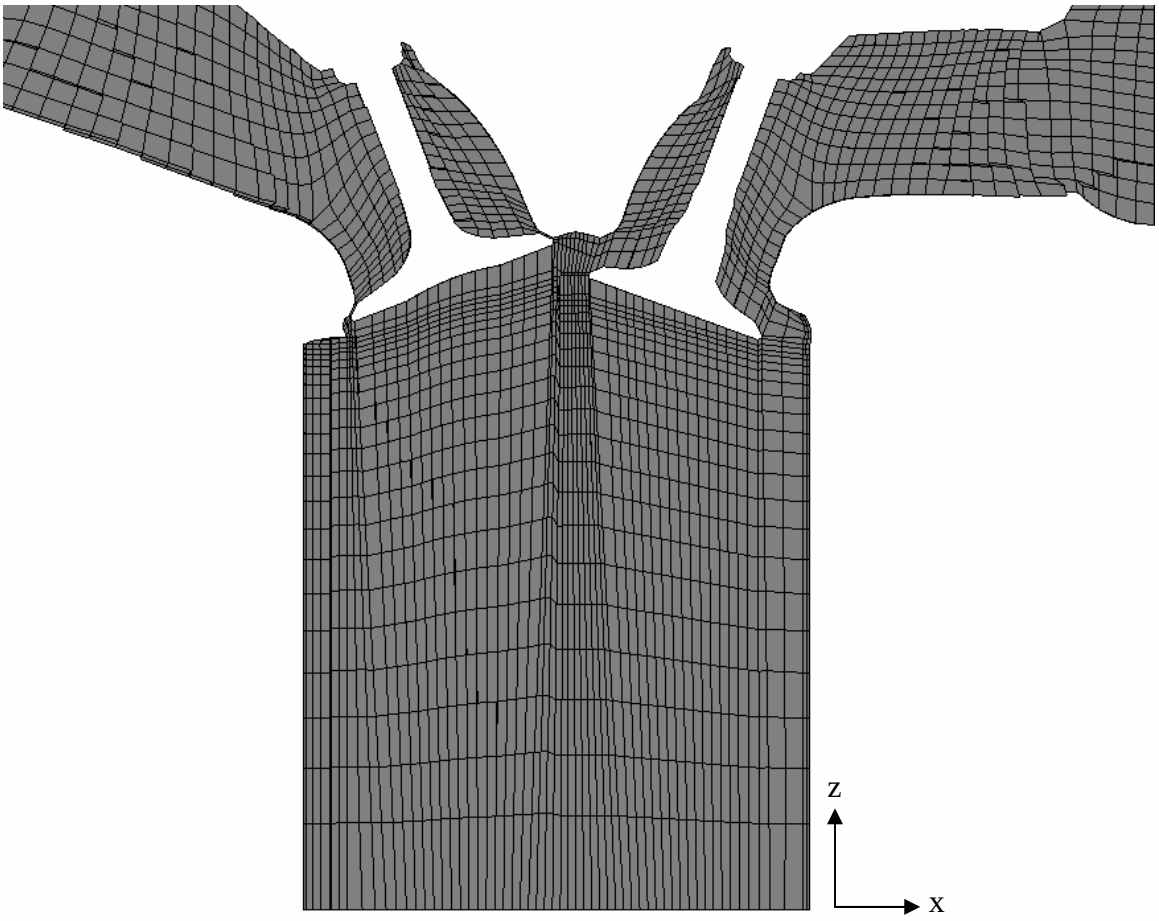


*Figure 51: Results After Fourth Step*

At this point in the rezoning subroutine, the only vertices with `moveme=1` are at the top of the cylinder and not in an *x* or *y* line which intersects a valve. The next step in the rezoning subroutine looks at all of these remaining points and

interpolates in the *x* direction between the nearest points which have `moveme` equal to 0, whether they be solid such as a wall and valve or previously interpolated vertices. This methodology makes sure that all grid points are interpolated instead of using a relaxation. This results in a grid structure that is the same after each cycle instead of having relaxations that develop grid structure over a number of cycles. Figure 52 shows grid relaxation in the rezoning subroutine where the cells that have been relaxed are shown cells are in gray.

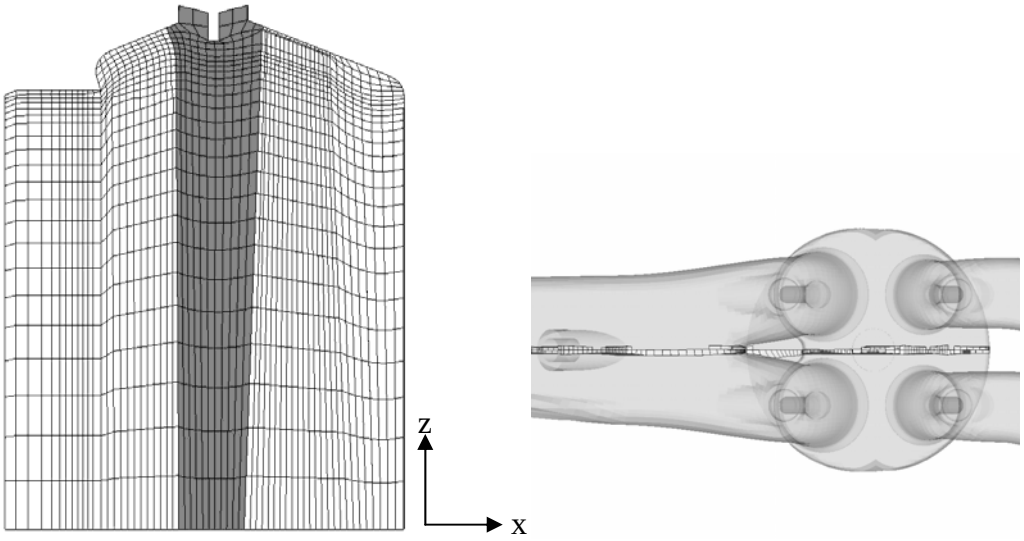


*Figure 52: Relaxation in Center of Cylinder*

Ideally the grid would done at this point but certain areas do cause problems because they are confined by the neighboring grid points and result in small, badly shaped computation cells. In addition to the interpolations up to this point a number of relaxations were needed to move grid points in problem areas.

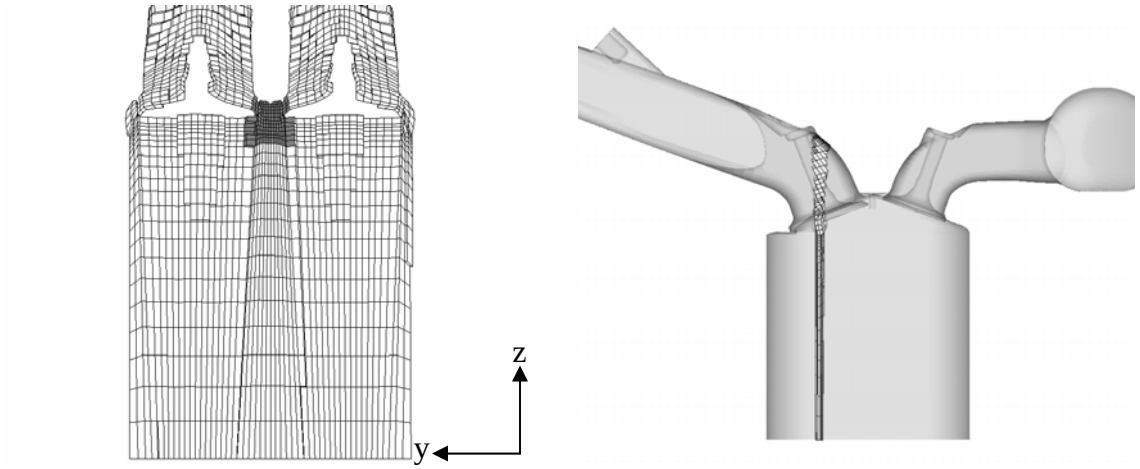


*Figure 53: Relaxation Between Intake Valves*

An *x* and *z* relaxation were needed for the points in between the intake valves because the *x* and *z* values were confining many cells in an awkward shape due to a groove in the cylinder head. The relaxation was very simple and counted through the vertices in this region averaging the *x* and *z* positions based on the neighboring 4 vertices in the *x*-*z* plane. This relaxation was conducted four times to allow for enough grid movement. Figure 53 shows grid relaxation between the intake valves where the cells that have been relaxed are shown cells are in gray.

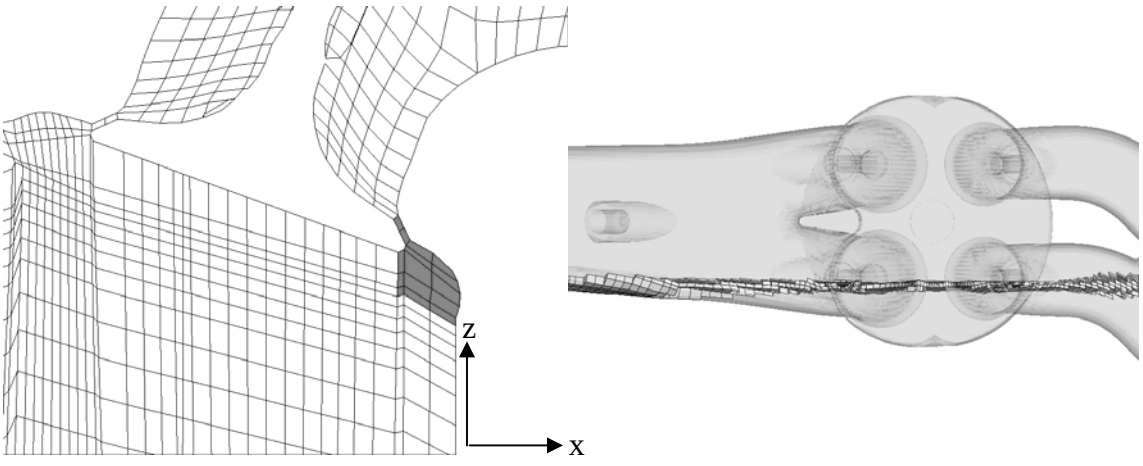


*Figure 54: Relaxation on Edge of Exhaust Valve*

A similar problem was encountered in the area in between one of the exhaust valves and the side wall. The cylinder head was conformed to the shape of the valve which resulted in only 2 grid vertices between the valve and the cylinder head. This lack of cells created very narrow long grid cells that cause problems due to cell inversions. The same relaxation was used in these areas as was used between the valves, and this gave those few grid vertices the ability to move and create more uniform cells. Figure 54 shows grid relaxation on the edge of exhaust valve where the cells that have been relaxed are shown cells are in gray.

# Appendix B – Compilation of Input Parameters

## *KIVA3v*

### ERC1

```
 K122298 4-valve MERCURY
VERADO, (082996), 052899
  irest     0
 nohydro    0
  lwall     1
  lpr       0
  irez      7
  ncfilm99999
  nctap899999
  nclast99999
  ncmon     50
 ncaspec    1
-180.0
  gmv       0.0
  cafilm    5.0
  cafin  1300.0
  angmom    0.0
  pgssw     0.0
  dti   1.00000e-5
  dtmxca    1.0
  dtmax 1.00000e-5
  tlimd     0.0
  twfilm   9.99e+9
  twfin    9.99e+9
  fchsp     0.25
  bore      8.2
  stroke    8.1
  squish    0.22
  rpm       6.1e+3
  atdc     - 180.0
  datdct    0.0
  revrep    2.0
  conrod   13.3
  swirl     0.0
  swipro    3.11
  thsect  360.0
  sector    0.0
  epsy      1.0e-3
  epsv      1.0e-3
  epsp      1.0e-4
  epst      1.0e-3
  epsk      1.0e-3
  epse      1.0e-3
  gx     9800.0
  gy        0.0
  gz        0.0
  tcylwl  418.15
  thead   448.15
  tpistn  498.15
  pardon    0.0
  a0        0.0
  b0        1.0
  artvis    0.0
  ecnsrv    0.0
  adia      0.0
  anu0      0.0
  visrat-.66666667
  tcut   1000.0
  tcute  1200.0
  epschm    0.02
  omgchm    1.0
  turbsw    1.0
  sgsl      0.0
 trbchem    0.0
  capa     18.0
 pmplict    0.0
 lospeed    0.0
  airmu1  1.457e-5
  airmu2  110.0
  airla1  252.0
  airla2  200.0
  prl       0.74
  rpr       1.11
  rsc       1.11
  xignit    1.0e+4
  t1ign     9.99e+9
```

```
 tdign    9.99e+9
 ca1ign  999.0
 cadign   10.0
 xignl1   +0.175
 xignr1   +0.425
 yignf1   -0.125
 yignd1   +0.125
 zignb1   9.6000
 zignt1   9.9500
 xignl2    0.0
 xignr2    0.0
 yignf2    0.0
 yignd2    0.0
 zignb2    0.0
 zignt2    0.0
 kwikeq    0
 numnoz    2
 numvel    1
injdist    1
 kolide    1
 t1inj   -9.99e+9
 tdinj   -9.99e+9
 ca1inj  -99.5
 cadinj  459.7
 tspmas    0.07179
 pulse     2.0
 tnparc 1000.0
 tpi     333.15
 turb      1.0
breakup    1.0
 evapp     1.0
 drnoz    -9.870
 dznoz    15.47
 dthnoz    0.0
 tiltxy   -9.3
 tiltxz   48.6
 cone     12.4
 dcone    12.4
 anoz      1.0
 smr      2.50e-3
 amp0      0.0
 drnoz    -9.870
 dznoz    15.47
 dthnoz    0.0
  tiltxy    8.8
  tiltxz   48.6
  cone     13.4
  dcone    13.4
  anoz      1.0
  smr      2.50e-3
  amp0      0.0
     3150.0
  nsp       5
  ic8h18
ic8h18
stoifuel    4.0
  stoio2   49.0
  nreg     10
 presi,     10*17.9000e+5
 tempi,     10*436.15
 tkei,      10*0.10
 scli,      10*0.0
 er,        10*0.0
o2          10*0.2200910204
n2          10*0.7650385386
co2         10*9.913863271e-3
h2o         10*4.956577746e-3
co          10*0.0
  nrk       0
  nre       0
 nvalves    4
vliftmin    0.025
 skirtth    0.037
  tmove   293.15
 vtiltxz  -21.05
  nlift   154
vliftmin    0.025
 skirtth    0.037
  tmove   293.15
 vtiltxz  -21.05
  nlift   154
vliftmin    0.05
 skirtth    0.037
  tmove   293.15
 vtiltxz  +20.05
  nlift   173
vliftmin    0.05
 skirtth    0.037
```

```
 tmove   293.15
vtiltxz  +20.05
 nlift   173
 isoot     0
distamb    2.0
 pamb    17.9000e+5
 tkeamb  435.35
 sclamb    4.8
 velin     0.0
 reedin    0.0
reedout    0.0
nregin0    9
nregamb    9
 numpcc    2
   0.0 9.9000e+5
  720.0 9.9000e+5
 numpex    2
   0.0 9.9000e+5
  720.0 9.9000e+5
```

**ERC2**

K122298 4-valve MERCURY
VERADO, (082996), 052899
 irest 0
 nohydro 0
 lwall 1
 lpr 0
 irez 7
 ncfilm99999
 nctap899900
 nclast99999
 ncmon 50
 ncaspec 1
-180.0
 gmv 0.0
 cafilm 5.0
 cafin 1800.0
 angmom 0.0
 pgssw 0.0
 dti 1.00000e-5
 dtmxca 1.0
 dtmax 5.00000e-5
 tlimd 0.0
 twfilm 9.99e+9
 twfin 9.99e+9
 fchsp 0.25
 bore 8.2
 stroke 8.1
 squish 0.22
 rpm 4.9e+3
 atdc - 180.0
 datdct 0.0
 revrep 2.0
 conrod 13.3
 swirl 0.0
 swipro 3.11
 thsect 360.0
 sector 0.0
 epsy 1.0e-3
 epsv 1.0e-3
 epsp 1.0e-4
 epst 1.0e-3
 epsk 1.0e-3
 epse 1.0e-3
 gx 9800.0
 gy 0.0
 gz 0.0
 tcylwl 418.15
 thead 448.15
 tpistn 498.15
 pardon 0.0
 a0 0.0
 b0 1.0
 artvis 0.0
 ecnsrv 0.0
 adia 0.0
 anu0 0.0
 visrat-.66666667
 tcut 1000.0
 tcute 1200.0
 epschm 0.02
 omgchm 1.0
 turbsw 1.0
 sgsl 0.0
trbchem 0.0
 capa 18.0
pmplict 0.0
lospeed 0.0
 airmu1 1.457e-5
 airmu2 110.0
 airla1 252.0
 airla2 200.0
 prl 0.74
 rpr 1.11
 rsc 1.11
 xignit 1.0e+4
 t1ign 9.99e+9
 tdign 9.99e+9
 ca1ign 999.0
 cadign 10.0
 xignl1 +0.175
 xignr1 +0.425
 yignf1 -0.125
 yignd1 +0.125
 zignb1 9.6000

```
 zignt1   9.9500
 xignl2    0.0
 xignr2    0.0
 yignf2    0.0
 yignd2    0.0
 zignb2    0.0
 zignt2    0.0
 kwikeq    0
 numnoz    2
 numvel    1
injdist    1
 kolide    1
 t1inj   -9.99e+9
 tdinj   -9.99e+9
 ca1inj  101.9
 cadinj  258.0
 tspmas    0.04942
 pulse     2.0
 tnparc 1000.0
 tpi     333.15
 turb      1.0
breakup    1.0
 evapp     1.0
 drnoz    -9.870
 dznoz    15.47
 dthnoz    0.0
 tiltxy   -9.3
 tiltxz   48.6
 cone     12.4
 dcone    12.4
 anoz      1.0
 smr      2.50e-3
 amp0      0.0
 drnoz    -9.870
 dznoz    15.47
 dthnoz    0.0
 tiltxy    8.8
 tiltxz   48.6
 cone     13.4
 dcone    13.4
 anoz      1.0
 smr      2.50e-3
 amp0      0.0
    3200.0
  nsp       5
  ic8h18
ic8h18
stoifuel    4.0
  stoio2   49.0
  nreg     10
 presi,     10*12.4000e+5
 tempi,     10*436.15
 tkei,      10*0.10
 scli,      10*0.0
 er,        10*0.0
o2          10*0.2200910204
n2          10*0.7650385386
co2         10*9.913863271e-3
h2o         10*4.956577746e-3
co          10*0.0
  nrk       0
  nre       0
 nvalves    4
vliftmin    0.025
 skirtth    0.037
  tmove   293.15
 vtiltxz  -21.05
  nlift   154
vliftmin    0.025
 skirtth    0.037
  tmove   293.15
 vtiltxz  -21.05
  nlift   154
vliftmin    0.05
 skirtth    0.037
  tmove   293.15
 vtiltxz  +20.05
  nlift   173
vliftmin    0.05
 skirtth    0.037
  tmove   293.15
 vtiltxz  +20.05
  nlift   173
  isoot     0
 distamb    2.0
  pamb   12.4000e+5
  tkeamb  370.65
  sclamb    4.8
```

velin 0.0
reedin 0.0
reedout 0.0
nregin0 9
nregamb 9
numpcc 2
0.0 9.9000e+5
720.0 9.9000e+5
numpex 2
0.0 9.9000e+5
720.0 9.9000e+5

## *KIVA3v Release 2*

### ERC1

K122298 4-valve MERCURY
VERADO, (082996), 052899
irest 0
nohydro 0
lwall 1
lpr 0
irez 7
ncfilm99999
nctap8 1000
nclast99999
ncmon 25
ncaspec 1
-180.0
gmv 0.0
cafilm 5.0
cafin 3000.0
angmom 0.0
pgssw 0.0
dti 1.00000e-5
dtmxca 1.0
dtmax 1.00000e-5
tlimd 0.0
twfilm 9.99e+9
twfin 9.99e+9
fchsp 0.25
bore 8.2
stroke 8.1
squish 0.22
rpm 6.1e+3
atdc -180.0
datdct 0.0
revrep 2.0
conrod 13.3
swirl 0.0
swipro 3.11
thsect 360.0
sector 0.0
deact 0.0
epsy 1.0e-3
epsv 1.0e-3
epsp 1.0e-4
epst 1.0e-3
epsk 1.0e-3
epse 1.0e-3
gx 9800.0
gy 0.0
gz 0.0
tport1 333.15
tport2 373.15
tcylwl 373.15
thead 373.15
tpistn 373.15
pardon 0.0
a0 0.0
b0 1.0
artvis 0.0
ecnsrv 0.0
adia 0.0
anu0 0.0
visrat-.66666667
tcut 1000.0
tcute 1200.0
epschm 0.02
omgchm 1.0
turbsw 1.0
sgsl 0.0
trbchem 0.0
capa 18.0
pmplict 0.0
lospeed 0.0
airmu1 1.457e-5
airmu2 110.0
airla1 252.0
airla2 200.0
prl 0.74
rpr 1.11
rsc 1.11
xignit 1.0e+4
t1ign 9.99e+9
tdign 9.99e+9

```
 ca1ign  999.0
 cadign   10.0
 xignl1   +0.175
 xignr1   +0.425
 yignf1   -0.125
 yignd1   +0.125
 zignb1   9.6000
 zignt1   9.9500
 xignl2    0.0
 xignr2    0.0
 yignf2    0.0
 yignd2    0.0
 zignb2    0.0
 zignt2    0.0
 kwikeq    1
 numnoz    2
 numinj    1
 numvel    1
 t1inj   -9.99e+9
 tdinj   -9.99e+9
 ca1inj  -99.5
 cadinj  459.7
 tspmas    0.07179
 tnparc 1000.0
 pulse     2.0
injdist    1
 kolide    1
 tpi     300.15
 turb      1.0
breakup    1.0
 evapp     1.0
 drnoz    -9.870
 dznoz    15.47
 dthnoz    0.0
 tiltxy   -9.3
 tiltxz   48.6
 cone     12.4
 dcone    12.4
 anoz      1.0
 smr      2.50e-3
 amp0      0.0
 drnoz    -9.870
 dznoz    15.47
 dthnoz    0.0
 tiltxy    8.8
 tiltxz   48.6
 cone     13.4
 dcone    13.4
 anoz      1.0
 smr      2.50e-3
 amp0      0.0
    3150.0
 nsp      12
gasoline
     o2   mw2     32.000  htf2     0.0
     n2   mw3     28.016  htf3     0.0
    co2   mw4     44.011  htf4   -93.965
    h2o   mw5     18.016  htf5   -57.103
      h   mw6      1.008  htf6    51.631
     h2   mw7      2.016  htf7     0.0
      o   mw8     16.000  htf8    58.989
      n   mw9     14.008  htf9   112.520
     oh   mw10    17.008  htf10    9.289
     co   mw11    28.011  htf11  -27.200
     no   mw12    30.008  htf12   21.456
stoifuel    4.0
 stoio2   49.0
 nreg     10
 presi,     10*17.9000e+5
 tempi,     10*323.15
 tkei,      10*0.10
 scli,      10*0.0
 er,        10*0.0
 mfracfu,   10*0.0
 mfraco2,   10*0.2200910204
 mfracn2,   10*0.7650385386
 mfracco2,  10*9.913863271e-3
 mfrach2o,  10*4.956577746e-3
 mfrach,    10*0.0
 mfrach2,   10*0.0
 mfraco,    10*0.0
 mfracn,    10*0.0
 mfracoh,   10*0.0
 mfracco,   10*0.0
 mfracno,   10*0.0
 nrk       4
 cf1   8.0000e10 ef1   1.5780e+4 zf1
 cb1      0.0    eb1      0.0    zb1      0.0
```

```
 am1     4   49    0    0    0    0    0    0
0    0    0    0
 bm1     0    0    0   32   34    0    0    0
0    0    0    0
 ae1    0.250   1.500   0.000   0.000
0.000   0.000   0.000   0.000
       0.000   0.000   0.000   0.000
 be1    0.000   0.000   0.000   0.000
0.000   0.000   0.000   0.000
       0.000   0.000   0.000   0.000
 cf2   1.5587e14 ef2   6.7627e+4 zf2
0.0
 cb2   7.5000e12 eb2      0.0    zb2
0.0
 am2     0    1    2    0    0    0    0    0
0    0    0    0
 bm2     0    0    0    0    0    0    0    0
2    0    0    2
 ae2    0.000   0.500   1.000   0.000
0.000   0.000   0.000   0.000
       0.000   0.000   0.000   0.000
 be2    0.000   0.000   0.000   0.000
0.000   0.000   0.000   0.000
       1.000   0.000   0.000   1.000
 cf3   2.6484e10 ef3   5.9418e+4 zf3
1.0
 cb3   1.6000e+9 eb3   1.9678e+4 zb3
1.0
 am3     0    2    1    0    0    0    0    0
0    0    0    0
 bm3     0    0    0    0    0    0    0    2
0    0    0    2
 ae3    0.000   1.000   0.500   0.000
0.000   0.000   0.000   0.000
       0.000   0.000   0.000   0.000
 be3    0.000   0.000   0.000   0.000
0.000   0.000   0.000   1.000
       0.000   0.000   0.000   1.000
 cf4   2.1230e14 ef4   5.7020e+4 zf4
0.0
 cb4      0.0    eb4      0.0    zb4      0.0
 am4     0    0    1    0    0    0    0    0
0    2    0    0
 bm4     0   0  0  0  0  2  0  0  0  0  0    2
 ae4    0.000   0.000   0.500   0.000
0.000   0.000   0.000   0.000
       0.000   1.000   0.000   0.000
 be4    0.000   0.000   0.000   0.000
0.000   1.000   0.000   0.000
       0.000   0.000   0.000   1.000
 nvalves    4
vliftmin    0.050  !0.025
 skirtth    0.037
  tmove   293.15
 vtiltxz  -21.05
  nlift   154
vliftmin    0.050
 skirtth    0.037
  tmove   293.15
 vtiltxz  -21.05
  nlift   154
vliftmin    0.025
 skirtth    0.037
  tmove   293.15
 vtiltxz  +20.05
  nlift   173
vliftmin    0.025
 skirtth    0.037
  tmove   293.15
 vtiltxz  +20.05
  nlift   173
  isoot     0
 distamb    2.0
  pamb 17.9000e+5
  tkeamb  324.0
  sclamb    4.8
  velin     0.0
  reedin    0.0
 reedout    0.0
 nregin0    9
 nregamb    9
  numpcc    2
     0.0 9.9000e+5
    720.0 9.9000e+5
  numpex    2
     0.0 9.9000e+5
720.0 9.9000e+5
```

**ERC2**

K122298 4-valve MERCURY
VERADO, (082996), 052899
irest 0
nohydro 0
lwall 1
lpr 0
irez 7
ncfilm99999
nctap8 1000
nclast99999
ncmon 25
ncaspec 1
-180.0
gmv 0.0
cafilm 5.0
cafin 3000.0
angmom 0.0
pgssw 0.0
dti 1.00000e-5
dtmxca 1.0
dtmax 1.00000e-5
tlimd 0.0
twfilm 9.99e+9
twfin 9.99e+9
fchsp 0.25
bore 8.2
stroke 8.1
squish 0.22
rpm 4.9e+3
atdc -180.0
datdct 0.0
revrep 2.0
conrod 13.3
swirl 0.0
swipro 3.11
thsect 360.0
sector 0.0
deact 0.0
epsy 1.0e-3
epsv 1.0e-3
epsp 1.0e-4
epst 1.0e-3
epsk 1.0e-3
epse 1.0e-3
gx 9800.0
gy 0.0
gz 0.0
tport1 333.15
tport2 373.15
tcylwl 373.15
thead 373.15
tpistn 373.15
pardon 0.0
a0 0.0
b0 1.0
artvis 0.0
ecnsrv 0.0
adia 0.0
anu0 0.0
visrat-.66666667
tcut 1000.0
tcute 1200.0
epschm 0.02
omgchm 1.0
turbsw 1.0
sgsl 0.0
trbchem 0.0
capa 18.0
pmplict 0.0
lospeed 0.0
airmu1 1.457e-5
airmu2 110.0
airla1 252.0
airla2 200.0
prl 0.74
rpr 1.11
rsc 1.11
xignit 1.0e+4
t1ign 9.99e+9
tdign 9.99e+9
ca1ign 999.0
cadign 10.0

```
 xignl1   +0.175
 xignr1   +0.425
 yignf1   -0.125
 yignd1   +0.125
 zignb1   9.6000
 zignt1   9.9500
 xignl2    0.0
 xignr2    0.0
 yignf2    0.0
 yignd2    0.0
 zignb2    0.0
 zignt2    0.0
 kwikeq    1
 numnoz    2
 numinj    1
 numvel    1
 t1inj   -9.99e+9
 tdinj   -9.99e+9
 ca1inj  101.9
 cadinj  258.0
 tspmas    0.04942
 tnparc 3000.0
 pulse     2.0
injdist    1
 kolide    1
 tpi     300.15
 turb      1.0
breakup    1.0
 evapp     1.0
 drnoz    -9.870
 dznoz    15.47
 dthnoz    0.0
 tiltxy   -9.3
 tiltxz   48.6
 cone     12.4
 dcone    12.4
 anoz      1.0
 smr      2.50e-3
 amp0      0.0
 drnoz    -9.870
 dznoz    15.47
 dthnoz    0.0
 tiltxy    8.8
 tiltxz   48.6
 cone     13.4
 dcone    13.4
 anoz      1.0
 smr      2.50e-3
 amp0      0.0
    3200.0
 nsp      12
gasoline
     o2   mw2     32.000  htf2     0.0
     n2   mw3     28.016  htf3     0.0
    co2   mw4     44.011  htf4   -93.965
    h2o   mw5     18.016  htf5   -57.103
      h   mw6      1.008  htf6    51.631
     h2   mw7      2.016  htf7     0.0
      o   mw8     16.000  htf8    58.989
      n   mw9     14.008  htf9   112.520
     oh   mw10    17.008  htf10    9.289
     co   mw11    28.011  htf11  -27.200
     no   mw12    30.008  htf12   21.456
stoifuel    4.0
 stoio2   49.0
 nreg     10
 presi,     10*12.4000e+5
 tempi,     10*310.15
 tkei,      10*0.10
 scli,      10*0.0
 er,        10*0.0
 mfracfu,   10*0.0
 mfraco2,   10*0.2200910204
 mfracn2,   10*0.7650385386
 mfracco2,  10*9.913863271e-3
 mfrach2o,  10*4.956577746e-3
 mfrach,    10*0.0
 mfrach2,   10*0.0
 mfraco,    10*0.0
 mfracn,    10*0.0
 mfracoh,   10*0.0
 mfracco,   10*0.0
 mfracno,   10*0.0
 nrk       4
 cf1   8.0000e10 ef1   1.5780e+4 zf1
0.0
 cb1      0.0    eb1      0.0    zb1      0.0
```

```
 am1     4   49    0    0    0    0    0    0
0    0    0    0
 bm1     0    0    0   32   34    0    0    0
0    0    0    0
 ae1    0.250   1.500   0.000   0.000
0.000   0.000   0.000   0.000
       0.000   0.000   0.000   0.000
 be1    0.000   0.000   0.000   0.000
0.000   0.000   0.000   0.000
       0.000   0.000   0.000   0.000
 cf2   1.5587e14 ef2   6.7627e+4 zf2
0.0
 cb2   7.5000e12 eb2      0.0    zb2
0.0
 am2     0    1    2    0    0    0    0    0
0    0    0    0
 bm2     0    0    0    0    0    0    0    0
2    0    0    2
 ae2    0.000   0.500   1.000   0.000
0.000   0.000   0.000   0.000
       0.000   0.000   0.000   0.000
 be2    0.000   0.000   0.000   0.000
0.000   0.000   0.000   0.000
       1.000   0.000   0.000   1.000
 cf3   2.6484e10 ef3   5.9418e+4 zf3
1.0
 cb3   1.6000e+9 eb3   1.9678e+4 zb3
1.0
 am3     0    2    1    0    0    0    0    0
0    0    0    0
 bm3     0    0    0    0    0    0    0    2
0    0    0    2
 ae3    0.000   1.000   0.500   0.000
0.000   0.000   0.000   0.000
       0.000   0.000   0.000   0.000
 be3    0.000   0.000   0.000   0.000
0.000   0.000   0.000   1.000
       0.000   0.000   0.000   1.000
 cf4   2.1230e14 ef4   5.7020e+4 zf4
0.0
 cb4      0.0    eb4      0.0    zb4      0.0
 am4     0    0    1    0    0    0    0    0
0    2    0    0
 bm4     0    0    0    0    0    2    0    0
0    0    0    2
 ae4    0.000   0.000   0.500   0.000
0.000   0.000   0.000   0.000
       0.000   1.000   0.000   0.000
 be4    0.000   0.000   0.000   0.000
0.000   1.000   0.000   0.000
       0.000   0.000   0.000   1.000
 nvalves    4
vliftmin    0.050  !0.025
 skirtth    0.037
  tmove   293.15
 vtiltxz  -21.05
  nlift   154
vliftmin    0.050
 skirtth    0.037
  tmove   293.15
 vtiltxz  -21.05
  nlift   154
vliftmin    0.025
 skirtth    0.037
  tmove   293.15
 vtiltxz  +20.05
  nlift   173
vliftmin    0.025
 skirtth    0.037
  tmove   293.15
 vtiltxz  +20.05
  nlift   173
  isoot     0
 distamb    2.0
  pamb 12.4000e+5
  tkeamb  310.0
  sclamb    4.8
  velin     0.0
  reedin    0.0
 reedout    0.0
 nregin0    9
 nregamb    9
  numpcc    2
    0.0 9.9000e+5
   720.0 9.9000e+5
  numpex    2
    0.0 9.9000e+5
```

720.0 9.9000e+5

# Appendix C – Calculation of Multi-component Distributions

The multi-component distributions were calculated based on ASTM D-86 tests results which were supplied from Mercury Marine. The method is based on that of Cotterman et al. [12]. A list of single-component fuels were used to generate Figure 55, which provided a correlation between molecular weight and dew point. Combining the curve fit of Figure 55 and integration of the Pearson III distribution results in a percent recovered versus temperature correlation. The ASTM D-86 tests were curve fit to correlate percent recovered versus temperature. Figure 56 thru Figure 60 shows the ASTM D-86 curve fits of the five test fuels along with the calculated D-86 test results of the distributions.

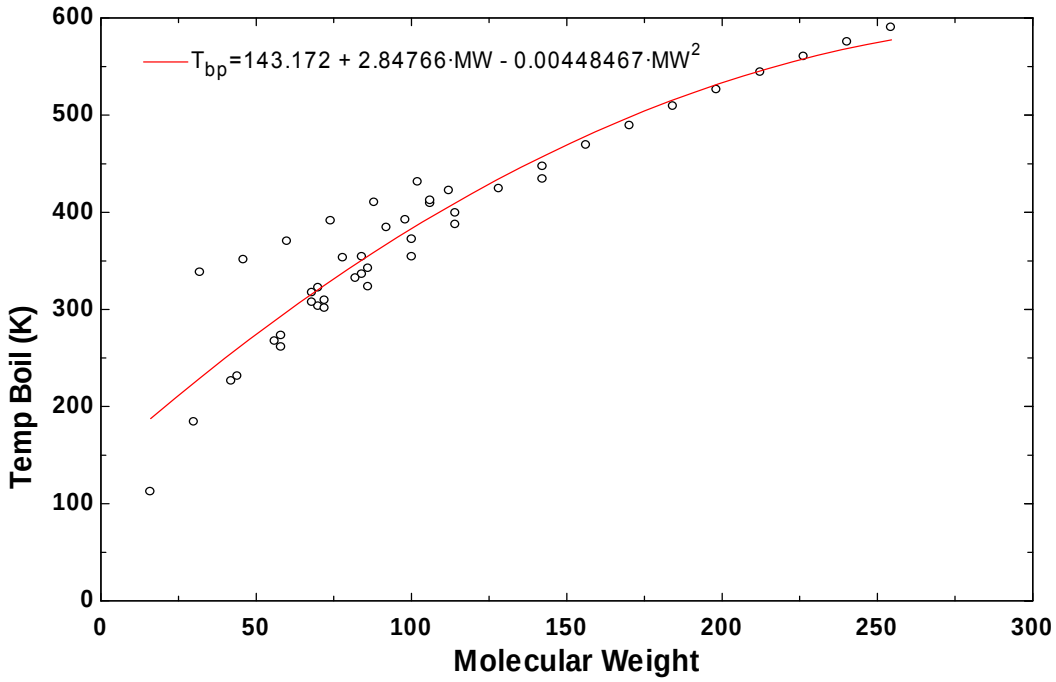


*Figure 55: Curve Fit Multiple Fuel Boiling Temperatures*

*Table 9: Results of D-86 Fuel Distributions*

| Fuel | Gasoline | Summer Regular Unleaded | Summer Premium Unleaded | Winter Regular Unleaded | Winter Premium Unleaded | Halterman HE |
|---|---|---|---|---|---|---|
| α | 5.7 | 10.77 | 14.97 | 10.46 | 12.82 | 12.62 |
| β | 15.0 | 8.97 | 5.732 | 9.206 | 7.318 | 9.877 |
| Γ | 0.0 | 0.0 | 0.0 | 0.0 | 0.0 | 0.0 |

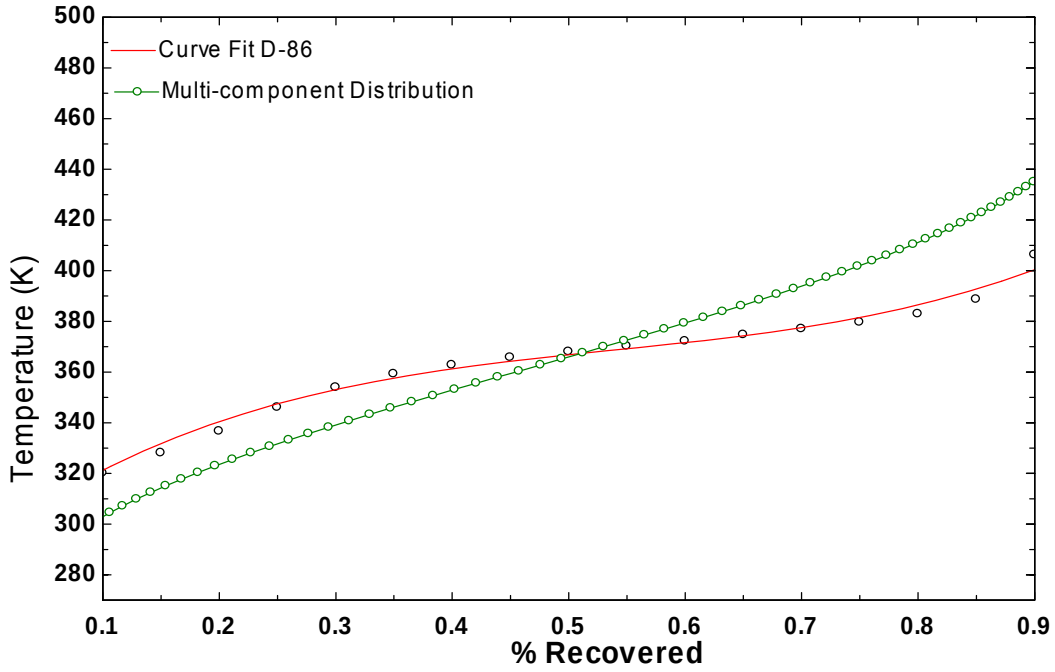


*Figure 56: Winter Premium ASTM D-86*

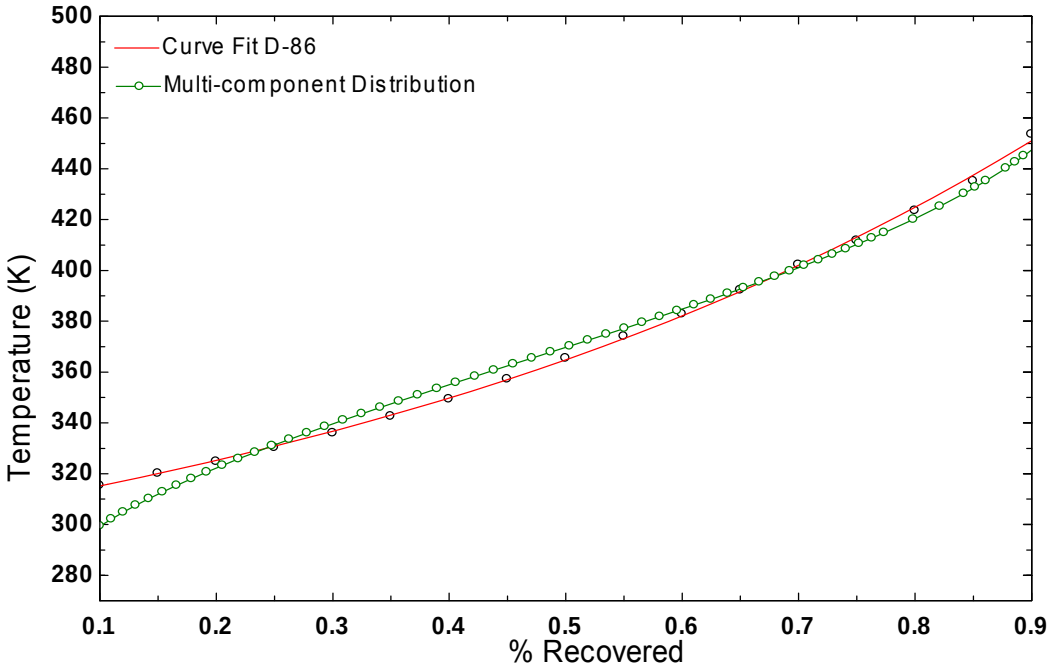


*Figure 57: Winter Regular ASTM D-86*

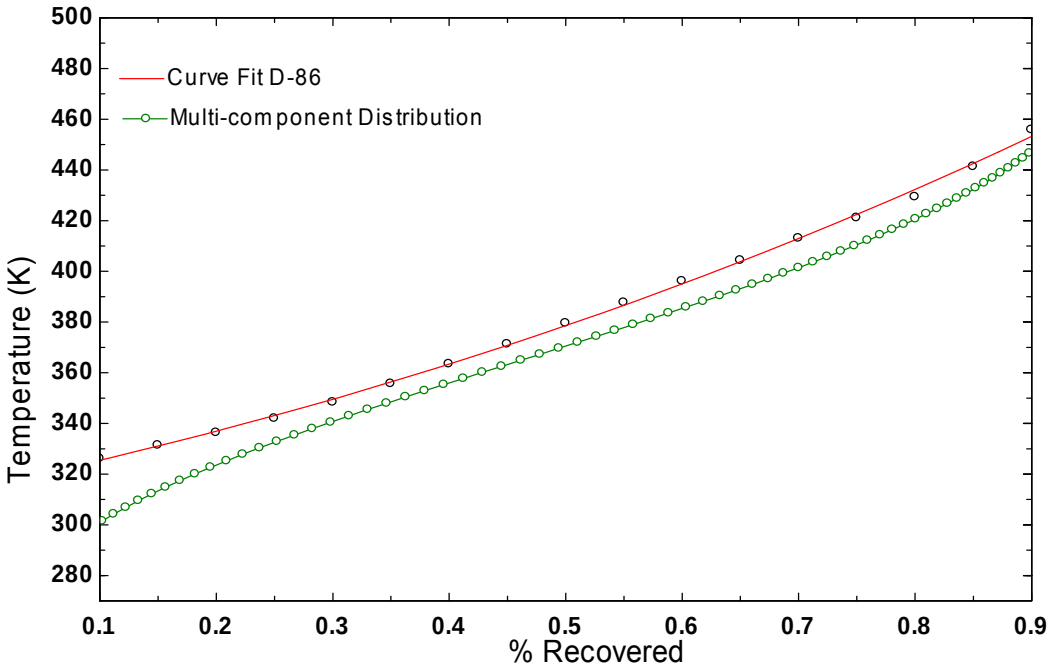


*Figure 58: Summer Regular ASTM D-86*

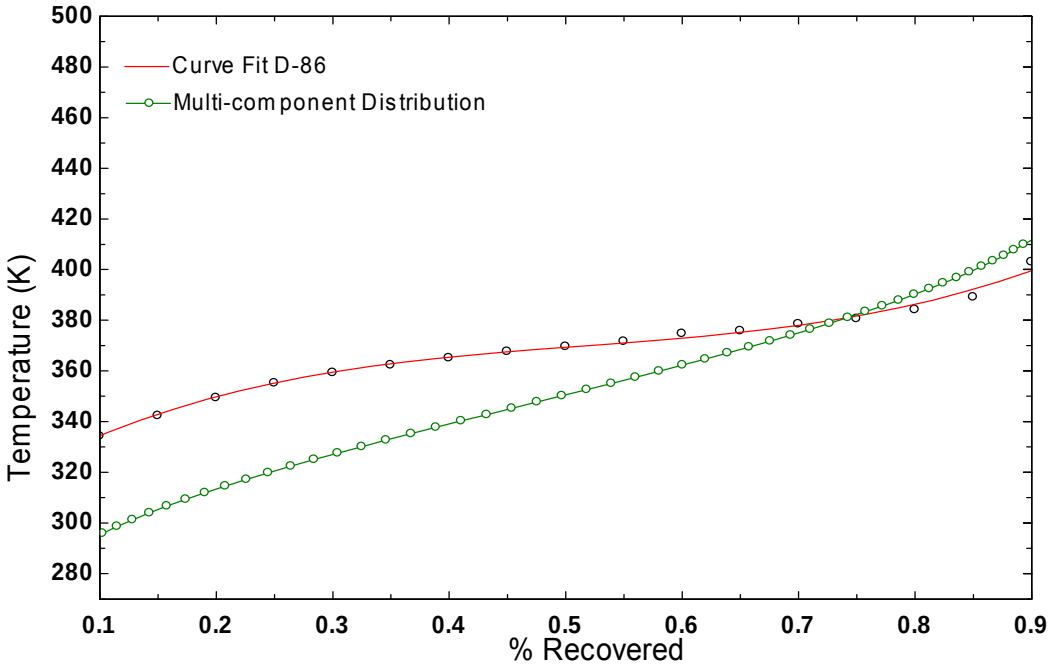


*Figure 59: Summer Premium ASTM D-86*

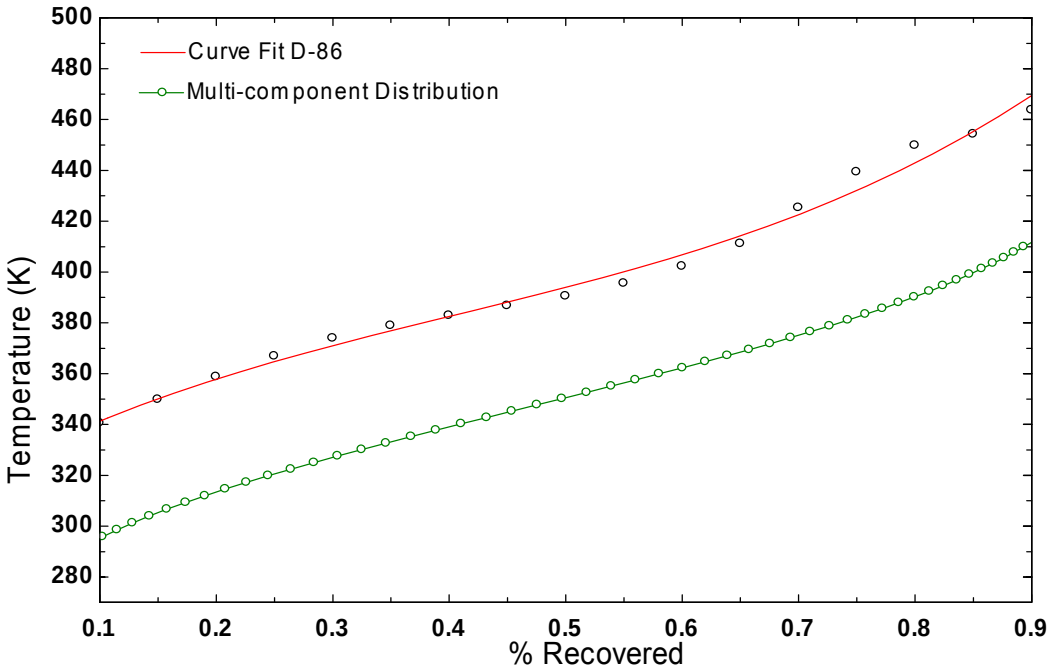


*Figure 60: Haltermann HE ASTM D-86*

## EES code which was used to solve for distribution variables

```
"alpha=5.7
beta=15 For Gasoline disribution"

gamma=0
MW=(alpha+1)*beta
variance=sqrt(alpha*beta^2)

f=(I+gamma)^(alpha-1)/(beta^alpha*GAMMA_(alpha))*exp(-(I-gamma)/beta)
"person distribution"

"DEWPOINT=143.172 + 2.84766*I - 0.00448467*I^2"  "fit curve for pearson"

PERCENT_Pearson=integral(f,i,116,300)

"WINTER PREMIUM UNLEADED"
"TEMPBOIL=293.824 + 322.42*Percent_Pearson - 510.607*Percent_Pearson^2 +
315.491*Percent_Pearson^3 ""winter Premium 2002/2003"
"DEWPOINT=143.172 + 2.84766*M - 0.00448467*M^2  ""fit curve"
"alpha=12.82
beta=7.318"
"ERROR=integral(abs(TEMPBOIL-DEWPOINT),i,0,300)"

"WINTER REGULAR UNLEADED"
"TEMPBOIL=306.014 + 87.4836*Percent_pearson + 32.9911*Percent_pearson^2+
54.2025*Percent_Pearson^3"
"DEWPOINT=143.172 + 2.84766*M - 0.00448467*M^2 " "fit curve"
alpha=10.46
beta=9.206
"ERROR=integral(abs(TEMPBOIL-DEWPOINT),i,0,300)"

"REGULAR UNLEADED SUMMER"
"TEMPBOIL=306.014 + 87.4836*Percent_pearson + 32.9911*Percent_pearson^2+
54.2025*Percent_pearson^3"
"DEWPOINT=143.172 + 2.84766*M - 0.00448467*M^2 " "fit curve"
"alpha=10.77
beta=8.97"
"ERROR=integral(abs(TEMPBOIL-DEWPOINT),i,0,300)"

"Premium UNLEADED SUMMER"
"Tempboil=311.842 + 268.836*Percent_pearson - 454.211*Percent_pearson^2 +
293.154*Percent_pearson^3"
"DEWPOINT=143.172 + 2.84766*M - 0.00448467*M^2"  "fit curve"
"alpha=14.97
beta=5.732"
"ERROR=integral(abs(TEMPBOIL-DEWPOINT),i,0,300)"

"Haltermann HE "
"tempboil=320.056 + 242.008*Percent_pearson - 318.497*Percent_pearson^2 +
259.936*Percent_pearson^2"
"DEWPOINT=143.172 + 2.84766*M - 0.00448467*M^2  ""fit curve"
```

```
"alpha=12.62
beta=9.877"
"ERROR=integral(abs(TEMPBOIL-DEWPOINT),i,0,300)"


"ERROR=abs(TEMPBOIL-DEWPOINT)

$integraltable i,f , percent_pearson, tempboil, dewpoint,error"
```